New approaches in super-resolution microscopy

Bin Yang

université de BORDEAUX

THÈSE PRÉSENTÉE

POUR OBTENIR LE GRADE DE

DOCTEUR DE

L'UNIVERSITÉ DE BORDEAUX

ÉCOLE DOCTORALE DES SCIENCES PHYSIQUES ET DE L'INGÉNIEUR

SPÉCIALITÉ : LASER, MATIÈRE ET NANOSCIENCES

Par Bin YANG

NEW APPROACHES IN SUPER-RESOLUTION MICROSCOPY

Soutenue le : Lundi 13 avril 2015

Après avis de :

Michel ORRIT	Rapporteur
Christian EGGELING	Rapporteur

Devant la commission d'examen formée de :

Valentin NÄGERL	Professeur	Université de Bordeaux	Président
Michel ORRIT	Professeur	Université de Leiden	Rapporteur
Christian EGGELING	Professeur	Université d'Oxford	Rapporteur
Vahid SANDOGHDAR	Professeur	Max Planck Institute	Examinateur
Jean-Baptiste TREBBIA	Chargé de recherche	CNRS	Examinateur
Brahim LOUNIS	Professeur	Université de Bordeaux	Directeur de thèse

Résumé

La microscopie joue un rôle important pour observer et étudier les petits objets. Parmi toutes les techniques d'imagerie de l'état de l'art, la microscopie optique en champ lointain est la plus largement utilisée en biologie, avec une bonne résolution à l'échelle des organites cellulaires. Parce qu'elle ne nécessite pas de préparation complexes des échantillons, son fonctionnement est assez simple, il est le seul moyen d'imager des échantillons épais en trois dimensions dans des conditions physiologiques. La fluorescence a joué un rôle important dans l'évolution de la microscopie optique en champ lointain. En filtrant spectralement les photons excitateurs et en ne collectant que les photons de fluorescence décalée vers le rouge, on peut obtenir des images de très bon contraste et on peut même détecter des nano-émetteurs uniques. Diverses techniques de microscopie à fluorescence telles que la microscopie confocale et la microscopie à deux photons ont été développés avec des avantages distincts en fonction des applications.

Cependant la résolution d'un microscope optique est fondamentalement limitée par la diffraction, avec la résolution définie comme la plus petite distance nécessaire pour distinguer deux objets ponctuels. À cause de la diffraction, la lumière provenant d'un objet ponctuel ne converge pas vers un seul point du plan image, mais se répand dans l'espace selon un volume de taille fini, i.e. la fonction d'étalement du point (Point Spread Function ou PSF). L'étendue spatiale tri-dimensionnelle de la PSF détermine la plus petite dimension qui peut être résolu dans une image. Selon Émile Verdet, Ernst Abbe et Lord Rayleigh, la résolution d'un microscope optique est définie par $0.61\lambda/NA$ dans la direction latérale, et $2n\lambda/NA^2$ dans la direction axiale, où λ est la longueur

d'onde de lumière, $NA = nsin\alpha$ l'ouverture numérique de l'objectif, avec n l'indice de réfraction du milieu de microscope et α le demi-angle du cône maximum de lumière qui peut entrer ou sortir de l'objectif. Avec la lumière visible et un objectif à immersion dans l'huile (typiquement de $NA \sim 1{,}4$), la meilleure résolution latérale est d'environ 200 nm et la résolution axiale est d'environ 1 μm.

En dépassant la limite de diffraction et en offrant une résolution allant jusqu'à quelques nanomètres, la microscopie à fluorescence de super-résolution a révolutionné la microscopie optique en champ lointain au cours de la dernière décennie.

L'utilisation des propriétés spectroscopiques des émetteurs fluorescents joue un rôle important dans la réalisation des techniques de super-résolution. À cause de la limite de diffraction, les images de fluorescence des émetteurs dans un volume limité par la diffraction se recouvrent et ne se distinguent pas. Exploiter les propriétés photophysiques et photo-chimiques des émetteurs permet d'activer les émetteurs séquentiellement et ainsi de les résoudre optiquement. Cette séquentialité de l'imagerie est réalisée par des moyens stochastiques ou déterministes. Les méthodes de super-résolution stochastiques sont basées sur la localisation d'émetteurs uniques isolés, tels que PALM (photo activated localization microscopy), STORM (stochastic optical reconstruction microscopy) et (u)PAINT ((universal) points accumulation for imaging in nanoscale topography). Les méthodes déterministes sont basées sur l'excitation (ou la déplétion) des émetteurs par des motifs optiques qui limitent l'émission de fluorescence à des positions pré-déterminées, telles que STED (stimulated emission depletion), GSD (ground state depletion) et (S)SIM ((saturated) structured illumination microscopy).

La microscopie de super-résolution a eu beaucoup de succès dans différents domaines notamment dans la bio-imagerie. En 2014, le prix Nobel de chimie a été attribué à trois chercheurs "pour le développement de la microscopie à fluorescence de super-résolution". Néanmoins, la microscopie de super-résolution est encore en cours de développement rapide. Le défi pour les chercheurs consiste à en améliorer les performances, telles que

la vitesse d'imagerie, l'amélioration de la résolution en trois dimensions, la profondeur d'imagerie dans l'échantillon et l'applicabilité à des échantillons vivants.

Au cours de cette thèse, nous avons développé deux technique de microscopies de super-résolution: Lattice-STED (optical lattice STED microscopy) et ESSat (excitation state saturation microscopy). Lattice-STED vise à améliorer la vitesse d'imagerie de la microscopie STED, et démontre pour la première fois sa parallélisation massive (jusqu'à 100 fois). La microscopie Essat étend l'application de la microscopie de super-résolution à la température de l'hélium liquide sur des molécules organiques uniques insérées dans une matrice solide. Nous avons atteint une résolution de moins de dix nanomètres à de faibles intensités lumineuses et montré que la microscopie Essat est capable de résoudre au-delà de la limite de diffraction des molécules uniques avec des résonances optiques proches.

Dans la première partie de ce manuscrit, je vais vous présenter Lattice-STED. STED repose sur la combinaison d'un faisceau d'excitation focalisé avec un faisceau de déplétion. Le faisceau de déplétion a une longueur d'onde décalée vers le rouge et généralement une forme de beignet, qui peut désexciter les émetteurs par émission stimulée à la périphérie du faisceau d'excitation. De cette manière, STED réduit l'émission de fluorescence à un volume inférieur à celui limité par diffraction. Pour obtenir une image, il nécessite le balayage des deux faisceaux laser sur l'ensemble du champ de vision pendant l'acquisition. Cette modalité d'imagerie séquentielle implique que le gain de résolution se fait au détriment de la vitesse d'imagerie, ce qui pourrait être une limitation sévère lors de l'étude des structures dynamiques dans les cellules vivantes.

Ainsi, STED doit être parallélisée afin d'améliorer cette résolution temporelle pour permettre l'imagerie rapide à grand champ. Dans ce contexte, nous proposons et démontrons la parallélisation massive du STED par des réseaux optiques. Les réseaux optiques sont des motifs périodiques qui peuvent être générés par des interférences multi-faisceaux. Ils contiennent une matrice de cellules élémentaires, dont chacune a un min-

imum d'intensité entouré par une distribution d'intensité à peu près isotrope. Chaque cellule élémentaire joue le même rôle que le faisceau en forme de beignet, i.e. limiter le volume d'émission de fluorescence à l'échelle sous-diffraction par effet STED. Pour obtenir une image super-résolue, l'échantillon ne doit être balayé que sur une maille élémentaire du réseau optique au lieu de l'ensemble du champ de vision. Avec cette méthode, nous avons atteint une résolution de 70 nm avec un champ de vision de 3 μ m * 3 μ m. La vitesse d'imagerie de notre microscope Lattice-STED est de 80 ms par image super-résolue, qui est seulement limitée par le temps de lecture de la caméra.

Dans la deuxième partie, je présenterai la microscopie Essat sur des molécules uniques à température cryogénique. Les molécules organiques insérées dans des matrices solides à la température de l'hélium liquide sont de bons candidats pour effectuer des expériences d'optique quantique, en raison de la réduction drastique du déphasage des transitions optiques liés aux phonons, du grand facteur de qualité de la raie zéro-phonon et de l'excellente photostabilité. Dans de nombreux cas, la mesure des distances nanométriques entre les molécules uniques est nécessaire. Par exemple, la dépendance cubique de la distance de l'interaction dipôle-dipôle entre deux molécules restreint ce phénomène à une échelle de quelques dizaines de nanomètres. En outre, l'extraction de la distance entre un émetteur unique situé dans le champ évanescent d'une nanostructure et la nanostructure elle-même nécessite une excellente précision. Pour effectuer l'imagerie de super-résolution sur des molécules uniques, on excite tout d'abord ces molécules avec un faisceau en forme de beignet, ce qui nous permet de démontrer une résolution de 4,4 nm (largeur à mi-hauteur) avec une intensité d'excitation de seulement 13 kW / cm ^{2}. L'application supplémentaire d'un faisceau Gaussien temporellement modulé avec une technique de démodulation offre un meilleur contraste pour des images d'échantillons très concentrés. Une résolution de 9 nm a été obtenue avec cette méthode.

Acknowledgement

This thesis was prepared in the Nanophotonics group of Laboratoire Photonique, Numérique et Nanosciences (LP2N), a joint research unit between Institut d'Optique Graduate School (IOGS), University of Bordeaux and CNRS. I would like to thank Philippe Bouyer for having me in his laboratory.

My sincere gratitude to Michel Orrit and Christian Eggeling for their interest in my work and for being referees of my thesis. I would also like to thank Valentin Nägerl and Vahid Sandoghdar for being part of the jury committee.

Brahim Lounis not only proposed me the fascinating projects of super-resolution microscopy but also provided an outstanding scientific environment. He has been a wonderful supervisor, who is always enthusiastic about my work and constantly offers precious inputs. I would like to particularly thank him for frequently encouraging me and also for always believing in me.

Jean-baptise Trebbia has worked with me all along during this thesis. He has helped me to build optical setups, perform experiments, analyse data and prepare this manuscript. Without his help, I could not have done so much in this thesis.

It was a great pleasure working with Philippe Tamarat during my thesis. He is a great teacher of many qualities such as clarity and patience. He helped me greatly with the laser systems and the low temperature experiment. I would also like to thank him for proofreading the third chapter of this manuscript and for his advices.

I would like to thank Laurent Cognet for valuable discussions, proofreading the first chapter of this manuscript and his advices.

I would like to extend my gratitude to Michael Mestre, for his help with programming in both Labview and Matlab.

I gratefully acknowledge my collaborators Gregory Giannone and Olivier Rossier for providing me cell samples.

This work would not have been possible without the support from the mechanical and electronic workshops, both of LP2N and LOMA (Laboratoire Onde et Matière d'Aquitaine). Many thanks to Eddie Maillard, Sandra Bosio, Philippe Deulat, Jean-Hugues Codarbox and the others.

Thanks to all the friends that I met in Bordeaux: Nick, Christian, Chiara, Franck, Marion, Alex, Olga, Yi, Zhenghong, Jianji, Xiaorun... Thank you all for sharing these years with me and for the good memories.

I wholeheartedly want to thank my parents for their support. At last, I want to give special thanks to my wife, Pei-Wen, for her understanding and tolerance, for always being there.

Bordeaux, May 2015

Contents

Introduction

Scientific context

Diffraction limit

Microscopy plays an important role in observing and studying small objects. Being one of the most popular microscopy techniques, far-field optical microscopy uses light to probe the sample and can be compatible with living specimens. It is therefore an essential tool to study living cells and to understand their fundamental functions. An optical microscope gives a magnified image of the sample, which is otherwise not resolvable by human eye. However, the magnification cannot be set arbitrarily high in order to observe the finer details of the sample, because an optical microscope has limited resolution ultimately given by the diffraction, with the resolution defined as the smallest distance needed to distinguish two point objects. Light originating from a point object does not converge to a single point at the image plane, but spreads out in space to a finite-sized volume, called the point spread function (PSF). The three-dimensional spatial extent of the PSF determines the smallest dimension that can be resolved in the image. According to Émile Verdet [1], Ernst Abbe [2] and Lord Rayleigh [3], the resolution of an optical microscope is limited by diffraction as $0.61\lambda/NA$ in the lateral direction, and $2n\lambda/NA^2$ in the axial direction, where λ is the light wavelength, $NA = nsin\alpha$ the numerical aperture of the objective, n the refractive index of the microscope medium and α the half-angle of the maximum cone of light that can enter or exit the objective. In the visible range

and for an oil-immersion objective (typically of $NA \sim 1.4$), the best lateral resolution is around 200 nm and the axial resolution is around 1 μm.

Achieving better resolution

In order to investigate the ultrastructure of biological specimens including microorganisms, cells and molecular assembling, several microscopy methods have been developed which offer better resolution than far-field optical microscopy.

One approach consists of using waves with shorter wavelength. X-ray [4] has typically the wavelength between 0.1 nm and 5 nm. However, the lack of high refractive index material sets a constraint on the achievable resolution. Up to this day, 10 nm resolution has been achieved with Fresnel zone plates [5–7]. Because of the high energy applied on the sample, X-ray microscopy is not compatible with live cell imaging. Furthermore, the lack of available high energy sources limits its applications. Matter waves have even shorter wavelengths. For instance, electron beams have de Broglie wavelength at the order of 10^{-4} nm and can be used to achieve sub-angstrom resolution [8]. Electron microscopy [4, 9] has been widely used to study biological specimens. However, similar to X-ray microscopy, it is not compatible with live cell imaging. Moreover, the sample preparation is elaborate [10, 11], often requiring fixing the sample chemically, cutting the sample into slices and marking them with contrast enhancing materials such as gold.

Another approach is scanning probe microscopy, such as scanning near-field optical microscopy [12, 13], atomic force microscopy [14–17] and scanning tunnelling microscopy [18–20]. Near-field scanning microscopies use tips with sub-diffraction sizes ($\sim$ 1Å to 100 nm) and only probe areas at the vicinity of the tips. Therefore the resolution is determined by the size of the probe-sample interaction volume and can achieve atomic scale resolution [21, 22]. However, they are intrinsically surface probing methods and fail to investigate the inner space of a sample.

Fluorescence microscopy

Among all the state-of-art imaging techniques, far-field optical microscopy is the most widely used microscopy in biology, with a good resolution at the scale of cellular organelles. Because it does not require elaborate sample preparations; its operation is rather simple; it is the only way to image thick samples under physiological conditions in three dimensions. Fluorescence [23] has played an important role in the developments of modern far-field optical microscopy. By spectrally filtering out the exciting photons and collecting only the red-shifted fluorescence photons, one can obtain very good image contrast and can even detect single fluorescent nano-emitters [24, 25]. Various fluorescence microscopy techniques [26] such as confocal microscopy and two-photon excitation microscopy have been developed with distinct advantages depending on the applications. However, they share the same ultimate resolution limitation imposed by diffraction.

Super-resolution microscopy

By surpassing the diffraction limit and providing resolution down to a few nanometers, super-resolution fluorescence microscopy [27] has revolutionized far-field optical microscopy in the last decade.

The use of the spectroscopic properties of the fluorescent emitters plays an important role in super-resolution methods. Due to diffraction limit, the fluorescence images of different emitters from a diffraction-limited volume overlap and are not distinguishable. Exploiting the photo-physical and photo-chemical properties of emitters allows making them fluoresce sequentially and thus become optically resolvable. The sequential selective imaging is achieved either in stochastic or deterministic ways. Stochastic super-resolution methods are based on the localization of isolated single emitters, such as (fluorescence) photo activated localization microscopy ((f)PALM) [28, 29], (direct) stochastic optical reconstruction microscopy ((d)STORM) [30,31] and (universal) points accumulation for imaging in nanoscale topography ((u)PAINT) [32, 33]. Deterministic

methods are based on patterned excitation (or depletion) which restrict the fluorescence emission to pre-determined positions, such as stimulated emission depletion (STED) microscopy [34], ground state depletion (GSD) microscopy [35] and (saturated) structured illumination microscopy ((S)SIM) [36–38].

Super-resolution microscopy has showed great success in different fields especially in bioimaging. In 2014, the Nobel Prize in Chemistry was given to three researchers "for the development of super-resolved fluorescence microscopy" [39]. Even nowadays, super-resolution microscopy is still under rapid development. The challenge for researchers consists in improving the performances of super-resolution microscopy, such as the imaging speed [40–42], the three-dimensional resolution enhancement [43, 44], the imaging depth into the sample [45, 46] and the applicability to living samples [42, 47, 48].

During the course of this Doctorate work, we developed two super-resolution microscopies: optical lattice STED microscopy (Lattice-STED) and excitation state saturation (ESSat) microscopy. Lattice-STED aims at improving the imaging speed of STED microscopy, and demonstrates for the first time massive parallelization (up to 100-fold) of STED microscopy. ESSat microscopy extends the application of super-resolution microscopy to liquid helium temperature to image single organic molecules embedded in a solid host. We achieved sub-ten nanometer resolution at low light intensities and showed that ESSat microscopy is capable of resolving beyond the diffraction limit single molecules with close optical resonances.

In the first part of this thesis, I will present Lattice-STED. STED relies on the combination of a focused excitation beam with a depletion beam. The depletion beam has red-shifted wavelength and typically a doughnut shape, which can de-excite by stimulated emission fluorescent emitters at the periphery of the excitation beam. By this, STED restricts the fluorescence emission volume of the sample to a sub-diffraction scale. To obtain an image, it requires sequential acquisition while scanning the two laser beams over the whole field of view. This sequential imaging modality implies that the resolution

gain is at the expense of the imaging speed, which could be a severe limitation when studying dynamic structures in living cells. Fortunately STED microscopy only requires a limited number of fluorescence photons, which can be acquired at short pixel exposure times, to obtain the molecular density at the position of the emission. Therefore fast STED imaging has been achieved with raster scan for small fields of view [47]. However, STED would need to be parallelized in order to enhance this temporal resolution to allow faster wide-field imaging. In this context, we propose and demonstrate large parallelization of STED by optical lattices. Optical lattices are periodic patterns and can be generated by multi-beam interferences. They contain an array of unit cells, each of which has a centred intensity minimum surrounded by nearly isotropic intensity distribution. Each unit cell plays the same role as the doughnut beam, i.e. restricting the fluorescence emission volume to a sub-diffraction scale by stimulated emission depletion. To obtain a super-resolution image, the sample only needs to be scanned over a unit cell of the optical lattice instead of the entire field of view. With this method, we achieved a resolution of 70 nm with a field of view of 3 μm * 3 μm. The imaging speed of our Lattice-STED microscope is 80 ms per super-resolution image, which is only limited by the readout time of the camera.

In the second part, I will introduce cryogenic ESSat microscopy performed with single molecules. Organic molecules inserted in solid hosts at liquid helium temperature [24, 25] are good candidates to perform quantum optics experiments [49, 50], due to the drastic reduction of the dephasing related to phonons, the large quality factor of the zero-phonon line and the excellent photostability. In many cases, measurement of sub-diffraction distances between single molecules is necessary. For instance, the cubic dependence of the distance in the dipole-dipole interaction between two molecules [51] restricts such phenomenon to a scale of tens of nanometers. Moreover, extracting the distance between a single emitter located in the evanescent field of a nanostructure and the nanostructure itself requires an excellent accuracy. To perform super-resolution imag-

ing with single molecules, we first excite the molecules with a doughnut-shaped beam and demonstrate a resolution of 4.4 nm (FWHM) with an excitation intensity of only 13 kW/cm^2. Application of a modulated Gaussian beam together with a demodulation technique offers a better contrast in images of highly concentrated samples. A resolution of 9 nm was obtained with this method.

Plan of the manuscript

This thesis is structured as follows:

The first chapter introduces the principles of fluorescence microscopy and super-resolution microscopy. Firstly, it discusses the bases of several fluorescence microscopies such as confocal microscopy and two-photon excitation microscopy. Then, it gives a brief description of super-resolution microscopies, both deterministic and stochastic methods.

The second chapter presents Lattice-STED. Optical lattices generated by three- and four-beam interferences are discussed. The experimental realization and results of Lattice-STED are then presented.

The third chapter demonstrates cryogenic ESSat super-resolution microscopy. The optical saturation of single molecules and the principle of ESSat microscopy are introduced. The experimental setup and results are then presented.

The last chapter summarizes this thesis and discusses an outlook of further experiments and improvements of both Lattice-STED microscopy and ESSat microscopy.

CHAPITER 1

Fluorescence microscopy and super-resolution microscopy

1.1 Fluorescence microscopy techniques

Over the last decades, researchers have developed a large number of fluorescent markers which are now available for labelling virtually any biological systems. Immunofluorescence [52,53] uses the specificity of antibodies to their antigen to target fluorescent dyes or nanoparticles to specific biomolecules within cells, in order to visualize the distribution of the target molecule through the sample. It can be performed on cells and tissue sections that are fixed by a variety of methods. Many synthetic ligand systems [54–56] have also been developed to target fluorescent markers to biomolecules in living cells. Fluorescent proteins [57, 58] such as green fluorescent protein [59, 60] can be fused to proteins of interest to study living cells or animals. Overall, fluorescence microscopy is a flourishing field allowing investigations of biological systems.

1.1.1 Wide-field epifluorescence microscopy

The energy diagram of a fluorescent emitter is shown in Figure 1.1. Upon excitation with a laser beam, the emitter can be pumped from the ground state S_0 to a higher vibrational level of the excited state S_1, followed by fast relaxation (a few ps) to the lowest vibrational level of S_1 via a non-radiative process. From this level, the emitter

can emit fluorescence by spontaneous emission. By filtering out the exciting photons and collecting only the red-shifted fluorescence photons, fluorescence microscopy gives very good image contrast.

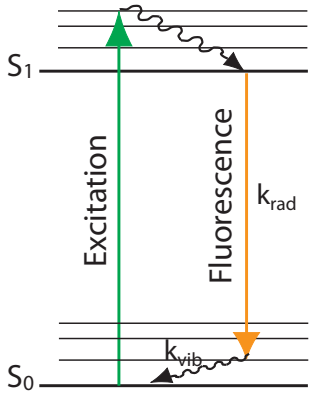

Figure 1.1: Energy diagram of a fluorescent emitter. An excitation laser excites the emitter from the ground state S_0 to a higher vibrational level of the excited state S_1. The emitter can emit fluorescence from the lowest vibrational level of S_1 by spontaneous emission.

The most common fluorescence microscopes, especially those used in life sciences, are based on epifluorescence as shown in Figure 1.2. In this configuration the microscope objective dose not only have the role of imaging the sample, but also serves as the condenser that illuminates it. A barrier (emission) filter between the objective and the photo-detector can filter out the scattered excitation light from the fluorescence. Therefore epifluorescence microscopy gives images with high signal to noise ratios.

In biology, the samples are often thick as compared to the depth of focus of the microscope. One problem with fluorescence microscopy is that regardless of the imaging plane in focus, the illumination causes the entire specimen thickness to fluoresce. Thus the out-of-focus fluorescence competes with the in-focus fluorescence and reduces the image contrast. More precisely, the depth of field (i.e. thickness of the imaging plane) of a high NA objective (NA $\geq$ 1.3) is only about 300 nm. The major part of a sample with a thickness much higher than this value is thus out of focus. A general approach

addressing this problem is to use techniques capable of optical sectioning, such as confocal microscopy and two-photon excitation microscopy.

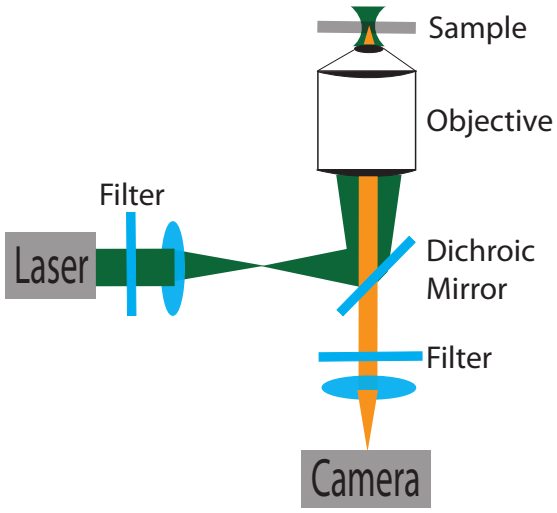

Figure 1.2: Diagram of an epifluorescence microscope. An objective is used for both illumination and imaging. A laser provides excitation light (in green) to illuminate the sample. Excited emitters can emit fluorescence (in red) which is collected by the objective. A combination of a dichroic mirror and an emission filter prevents the excitation light from reaching the camera.

1.1.2 Confocal microscopy

Invented by Minsky in 1955 [61], confocal microscopy [62] is one of key advances in microscopy. The principle is based on focused light illumination (as opposed to wide-field illumination) and the placement of a pinhole in the detection path. The invention of laser [63] largely facilitated this technique by making it possible to focus light into a diffraction-limited volume (the PSF). The diagram of a confocal microscope is shown in Figure 1.3. The focused light excites the fluorescent objects along its propagation both before and after the focal plane, inducing out-of-focus fluorescence. The role of the pinhole is to reject the out-of-focus fluorescence and only let through fluorescence originating from the focal volume. In order to form an image, the illumination volume is scanned through the sample while a point detector records the fluorescence signal.

We define $h_{exc}(r)$ and $h_{det}(r)$ as the excitation and detection PSFs, i.e. the normalized excitation intensity distribution in the focal plane of the objective and and the normalized fluorescence intensity distribution in the plane of the pinhole. The effective PSF of confocal microscopy is therefore given by [64]:

$$h_{conf}(r) = h_{exc}(r) \cdot [h_{det}(r) \otimes D(r)] \tag{1.1}$$

where $D(r)$ is the aperture function of the pinhole and $\otimes$ is the convolution sign. The excitation and detection wavelengths being approximately the same, the two PSFs are approximately identical. In practice, the diameter of the pinhole is chosen to be equal or smaller than the full-width-at-half-maximum (FWHM) of the excitation and detection PSFs, hence we have:

$$h_{conf}(r) \simeq h_{exc}(r)^2. \tag{1.2}$$

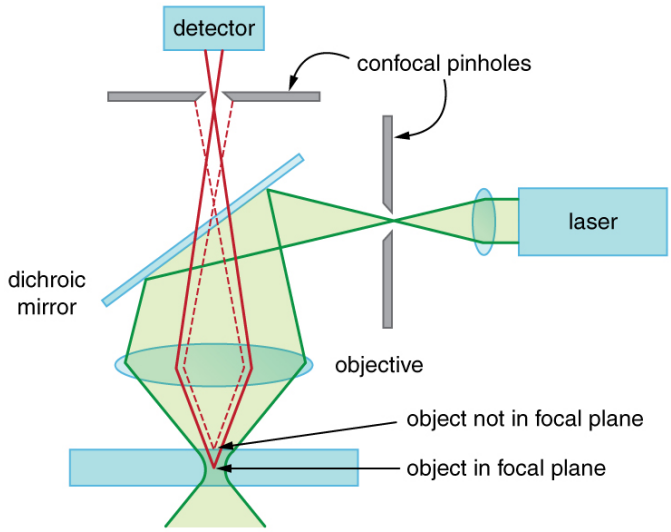

Figure 1.3: Diagram of a confocal microscope. An objective focuses the laser beam on the sample. A pinhole is set in the detection path and is conjugated with the focused laser spot to reject the out-of-focus fluorescence.

The excitation PSF is given by [65]:

$$h_{exc} = \Big[\frac{2J_1(k\,NA\,r)}{k\,NA\,r}\Big]^2 \tag{1.3}$$

where J_1 is the Bessel function of the first kind of order one, $k = 2\pi/\lambda$ is the wavenumber, NA is the numerical aperture and r is the radial distance from the optical axis.

Approximating the excitation PSF by a Gaussian distribution, the lateral resolution of confocal microscopy compared to that of wide-field fluorescence microscopy is improved by a factor of 1.4. In the following, we approximate the confocal PSF by a Gaussian distribution with a FWHM d_c and an amplitude equalling unity as:

$$h_{conf}(r) = exp(-4ln2\ r^2/d_c^2). \tag{1.4}$$

1.1.3 Two-photon excitation microscopy

With few exceptions biological tissues strongly scatter light, especially in the visible range. While confocal microscopy can reject the out-of-focus fluorescence in general, it fails to do so in deep tissues, where strongly scattered out-of-focus fluorescence photons may still pass through the pinhole. In addition, in-focus fluorescence photons may also be scattered and using a pinhole causes a net reduction of the detected signal. Therefore confocal microscopy is not readily applicable to thick tissues.

Two-photon excitation microscopy [66,67] has overcome this limitation and provides an imaging depth more than 500 μm in tissues [68–71]. A nonlinear absorption process involving two photons [72] is used (see Figure 1.4), which requires higher laser intensities for excitation than that in the single-photon case. Two-photon excitation microscopy only became possible with the emergence of pulsed lasers [73] which can provide high peak intensities with reasonable average intensity. The probability of absorbing two photons being proportional to the square of the light intensity, the fluorescence excitation

volume is restricted to the focal area of the beam. For commonly used fluorophores, two-photon absorption requires near-infrared wavelength excitation (700 - 1000 nm). Interestingly, near-infrared light also penetrates deeper into scattering tissue than visible light. Similar to confocal microscopy, two-photon excitation microscopy uses a focused beam on the sample and requires sample scanning to form an image. However, two-photon excitation microscopy does not require a pinhole on the detection path since out-of-focus excitation is minimal with the two-photon process.

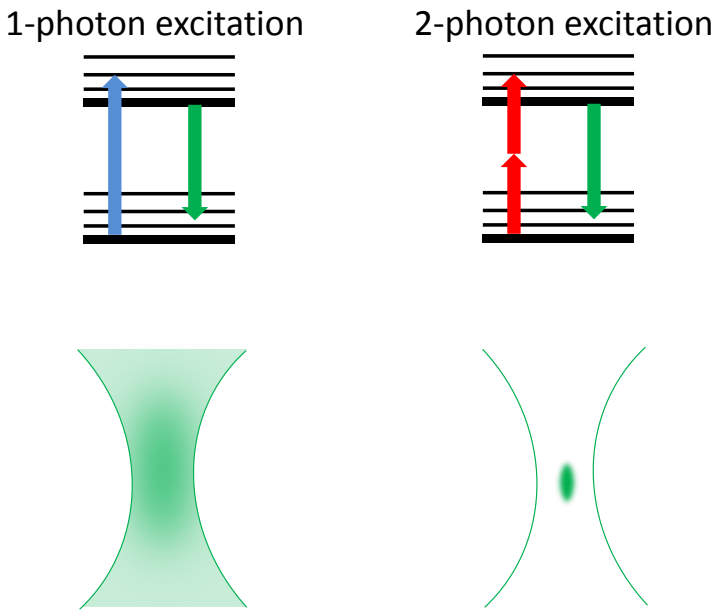

Figure 1.4: Single-photon and two-photon excitations. In the single-photon excitation case, one photon of the energy hv can excite fluorophores. The excitation takes place along the propagation of the light, both before and after the focal plane. In the two-photon excitation case, two photons of energy $hv/2$ act together to excite fluorophores. The excitation occurs only in the focal volume.

Assuming that the excitation PSF is h_{exc} and the detector is much bigger than the diffraction limit, the effective PSF of two-photon excitation microscopy is given by:

$$h_{TP}(r) = h_{exc}(r)^2. \tag{1.5}$$

Note that although Equation 1.5 is similar to the expression of the confocal PSF (Equation 1.1), the excitation wavelengths are different in the two cases. Therefore the resolution of two-photon excitation microscopy remains approximately the same as wide-field microscopy.

1.1.4 Improving the axial resolution

Both confocal microscopy and two-photon excitation microscopy have axial resolutions of about 1 μm, much larger than their lateral resolutions (about 200 nm). Several other methods have been developed to tackle this problem. Total internal reflection (TIRF) microscopy [74, 75] is a wide-field technique which uses illumination light with incident angle higher than the critical angle, so that the light is reflected at the interface of the microscope media and the sample. Only evanescent wave penetrates into the sample. Since the evanescent wave has a penetration depth of about 100 nm, only fluorescent objects close to the interface within this distance are illuminated. TIRF microscopy is well suited to study structures close to the interface, such as cell adhesion [76] and membrane dynamics [77]. Other methods such as 4Pi microscopy [78,79] and I^5M [80,81], rely on PSF engineering with two opposing objectives, which generate a PSF with a nearly spherical symmetry. 4Pi microscopy is based on confocal microscopy and I^5M is a wide-field technique. They both achieve an axial resolution of about 100 nm.

The aforementioned fluorescence microscopies have extended far-field optical microscopy to many new applications, however still with limited resolution, about 200 nm in all three dimensions. In order to study the stuctures of the sample at nanoscales, one needs to come up with new solutions providing better resolution. This was for a long time thought impossible due to diffraction limit, until the rise of super-resolution microscopy [82–84] during the past two decades.

1.2 Super-resolution optical far-field microscopy techniques

To date, super-resolution methods can be separated into two categories [85]. The first one concerns deterministic methods based on patterned excitation (or depletion), including stimulated emission depletion (STED) microscopy [34], ground state depletion (GSD) microscopy [35] and (saturated) structured illumination microscopy ((S)SIM) [36–38]. The second one concerns stochastic methods based on single molecule localization, such as (fluorescence) photo activated localization microscopy ((f)PALM) [28, 29], (direct) stochastic optical reconstruction microscopy ((d)STORM) [30,31] and (universal) points accumulation for imaging in nanoscale topography ((u)PAINT) [32,33].

STED was proposed in 1994 [34] and was experimentally realized in 1999 [86]. Thereafter, new super-resolution methods continue to emerge. SIM was introduced in 2000 [36], which offers a resolution enhancement of a factor of two compared to the diffraction limit. Based on the same principle as SIM, SSIM [37,38] can further provide theoretically unlimited resolution. Super-resolution method based on single molecule localization was proposed in 1985 [87] and was first realized in 1998 with single molecules in a solid at low temperature [88] and later in 2006 with biological samples [28–30]. These are the three most important super-resolution methods nowadays, which will be presented hereafter.

1.2.1 Stimulated emission depletion microscopy

1.2.1.1 Principles

The initial realization of STED microscopy [89] was based on confocal microscopy. It relies on the combination of a focused excitation beam (as in confocal microscopy) with a depletion beam. The depletion beam has red-shifted wavelength and typically a doughnut shape, which can deplete by stimulated emission fluorophores at the periphery of the excitation beam. Indeed, after being pumped to the excited state S_1, an emitter

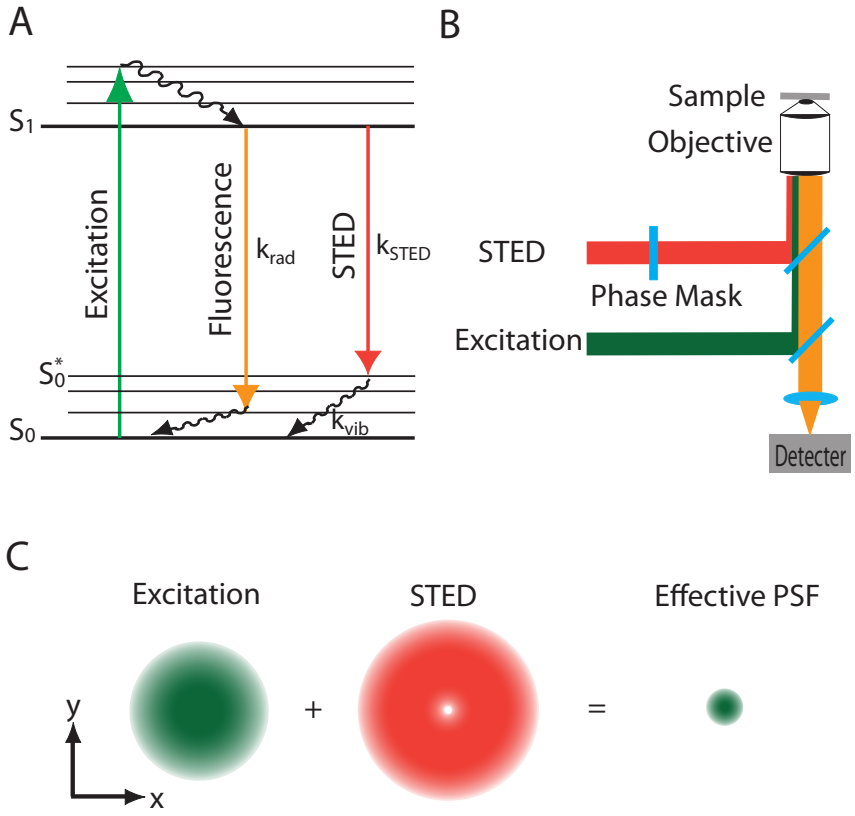

Figure 1.5: Principle of STED microscopy. (A) STED mechanism. An excitation laser excites an emitter from the ground state S_0 to a higher vibrational level of the excited state S_1. The emitter can emit fluorescence from the lowest vibrational level of S_1 by spontaneous emission. A STED photon can deplete S_1 to a excited vibrational level of S_0 by stimulated emission. (B) Diagram of the STED microscopy setup. The excitation and STED lasers are combined by dichroic mirrors and focused by an objective on the sample. The spatial form of the STED beam is modulated by a phase plate. A detector records the fluorescence. (C) Enhanced resolution with STED microscopy. A STED beam with a doughnut form overlaps the excitation beam, and suppresses the fluorescence from the pheriphery of the excitation beam. This leads to a reduced effective excitation PSF compared to the diffraction-limited PSF. Figure adapted by the author from [84].

can either emit fluorescence by spontaneous emission, or it can be de-excited to a vibrational level of the ground state S_0^* by stimulated emission, as shown in Figure 1.5A. The STED process is therefore in competition with the spontaneous emission process. Applying high STED intensities saturates the STED process and de-excites the population of S_1 mainly by stimulated emission, consequently the fluorescence is minimized. Only fluorophores in a small region around the zero intensity of the doughnut beam are allowed to fluoresce. By this, STED microscopy reduces the "effective excitation PSF", i.e. the volume where fluorescence emission can occur. This reduced excitation PSF offers super-resolution. Similar to confocal microscopy, STED microscopy requires sample scanning to form an image.

1.2.1.2 Calculation of the depleted fluorescence signal in pulsed-STED

The most common STED design is based on pulsed excitation (see Figure 1.6). Two synchronized pulsed lasers with repetition rate T_p^{-1} are used: the first one, delivering short pulses ($\sim$ ps), is for excitation of fluorophores. The second one, delivering pulses of width t_p about a few hundreds of ps, is for the depletion of fluorescence.

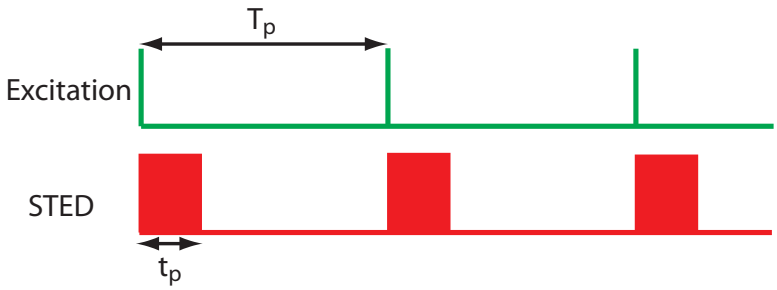

Figure 1.6: Laser sequences in pulsed-STED. Excitation pulses are typically of a few picosecond and can be therefore considered instantaneous. STED pulses arrive simultaneously with excitation pulses.

To calculate the fluorescence signal of fluorophores interacting with the two lasers, we examine the temporal evolutions of the relative populations P_{S1} of S_1 and P_{S0}^* of S_0^*.

To simplify the problem, several assumptions are made:

(a) fluorophores are initially in S_1 due to a short excitation pulse. T_p is much longer than the lifetime of the fluorophores τ, so that the fluorophores have relaxed to S_0 before the arrival of the next excitation pulse. The initial conditions are thus the same at the beginning of every excitation cycle.

(b) excitation of fluorophores from S_0 to S_1 by the red-shifted STED light is neglected since the STED wavelength is far from the excitation peak wavelength.

(c) both excitation and depletion beams are circularly polarized, therefore we can approximately neglect the orientation or rotation characteristics of the fluorophores.

During STED pulses, i.e. for $0 < t < t_p$, the relative populations P_{S1} of S_1 and P^*_{S0} of S^*_0 evolve with time as:

$$\begin{aligned} \frac{\partial}{\partial t}P_{S1} &= -\Gamma P_{S1} - \frac{\sigma\lambda I_p}{hc}\left(P_{S1} - P^*_{S0}\right) \\ \frac{\partial}{\partial t}P^*_{S0} &= -\Gamma_{vib} P^*_{S0} + \frac{\sigma\lambda I_p}{hc}\left(P_{S1} - P^*_{S0}\right) \end{aligned} \tag{1.6}$$

where $\Gamma = \tau^{-1}$ is the relaxation rate of S_1, Γ_{vib} is the vibrational relaxation rate from S^*_0 to the lowest vibrational level of S_0, λ and I_p are respectively the wavelength and peak intensity of the STED laser, σ is the cross-section of the fluorophore at λ, h is the Planck constant and c the speed of light in vacuum. At t = 0, $P_{S1}(0) = 1$ and all other states are unpopulated. Because $t_p \gg 1/\Gamma_{vib}$, the depopulation of S^*_0 is fast during the STED pulses. P_{S1} therefore approximately writes as:

$$P_{S1}(t) = exp(-\Gamma t)\, exp(-\frac{\sigma\lambda I_p}{hc}\, min(t, t_p)). \tag{1.7}$$

The first and second exponentials describe the de-excitation of S_1 due to respectively spontaneous and stimulated emissions.

Since t_p is much shorter (a few hundreds of picoseconds) than τ, the fluorescence emitted at $0 \leq t \leq t_p$ can be neglected. The probability of the emission of one fluores-

cence photon during one excitation cycle can be expressed as:

$$\begin{aligned} P_{em}(I) &= \eta_{rad}\Gamma \int_0^{T_p} P_{S1}(t)dt \approx \eta_{rad}\Gamma \int_{t_p}^{T_p} P_{S1}(t)dt \\ &\approx \eta_{rad}\, exp(-\Gamma t_p)\, exp(-\frac{\sigma\lambda I_p}{hc} t_p) \\ &= \eta_{rad}\, exp(-\Gamma t_p)\, exp(-\frac{ln2\ I}{I_S}) \end{aligned} \tag{1.8}$$

where η_{rad} is the quantum yield of the fluorophores, $I = I_p t_p / T_p$ is the average STED intensity, $I_S = ln2\ hc/(\sigma\lambda T_p)$ is the average saturation intensity at which half of the fluorescence is depleted [90]. Obviously, I_S depends on the spectroscopic properties of the fluorophores and the repetition rate of the STED laser. A STED laser with the same average power but lower repetition rates is therefore more efficient for depletion. Figure 1.7 shows P_{em} as a function of I/I_S. At higher STED intensities ($I > 7I_S$), P_{em} is well below 0.01 and the fluorescence is efficiently depleted.

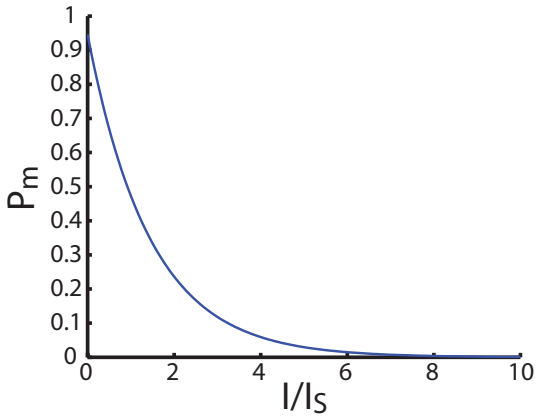

Figure 1.7: P_{em} as a function of STED intensity in pulsed-STED. Calculated for $\eta_{rad} = 1$, $\Gamma = 1/3.4$ ns^{-1}, $t_p = 200$ ps.

At low excitation intensities, the effective PSF of STED microscopy can be then written as:

$$\begin{aligned} h_{STED}(r) &= h_{exc}(r)\, P_{em}(I_{donut}(r))\, [h_{det}(r) \otimes D(r)] \\ &\approx h_{conf}(r)\, P_{em}(I_{donut}(r)) \end{aligned} \tag{1.9}$$

where $I_{donut}(r)$ is the intensity distribution of the doughnut beam. It can be described by the Laguerre-Gaussian mode LG(0,1) and writes as [91]:

$$I_{donut}(r) = eI_{STED}\, \frac{4r^2}{d^2}\, exp(-\frac{4r^2}{d^2}) \tag{1.10}$$

where I_{STED} is the maximal average intensity of the doughnut beam and d is its diameter, i.e. the distance between two opposing intensity maxima. The intensity profiles of the excitation and STED beams are shown in Figure 1.8A. The STED resolution depends strongly on the STED intensity. The higher the STED intensity is, the narrower the STED PSF becomes, as shown in Figure 1.8B.

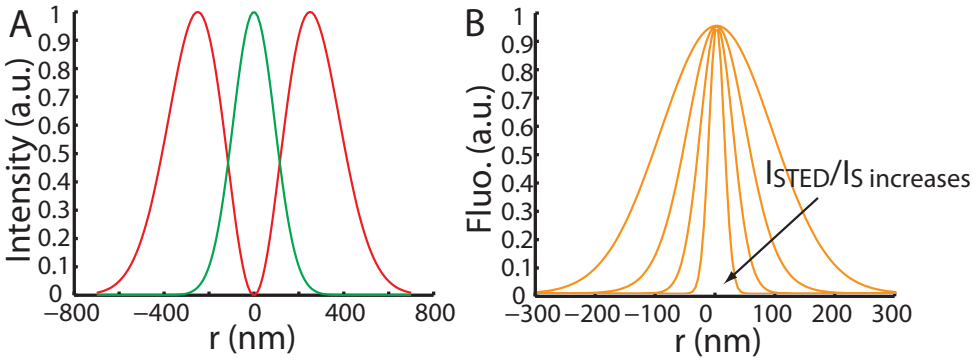

Figure 1.8: (A) Intensity profiles of the excitation Gaussian beam (green) and the depletion doughnut beam (red); (B) effective excitation PSFs of STED microscopy as a function of I_{STED}/I_S. Calculated for a Gaussian beam of the FWHM of 220 nm, a doughnut beam of the diameter of 500 nm and I_{STED}/I_S = 0, 5, 20 and 100.

1.2.1.3 Calculation of the resolution of pulsed-STED

For simplification, we approximate the doughnut beam with a sinus function near the optical axis [92]:

$$I_{donut}(r) = I_{STED}\, sin^2(\frac{\pi r}{d}). \tag{1.11}$$

Figure.1.9 compares the intensity profiles of a doughnut beam calculated with respectively Equation 1.10 and Equation 1.11. The two profiles overlap well around the "zero" intensity ($-d/2 \leq r \leq d/2$), with an intensity difference within 10 %.

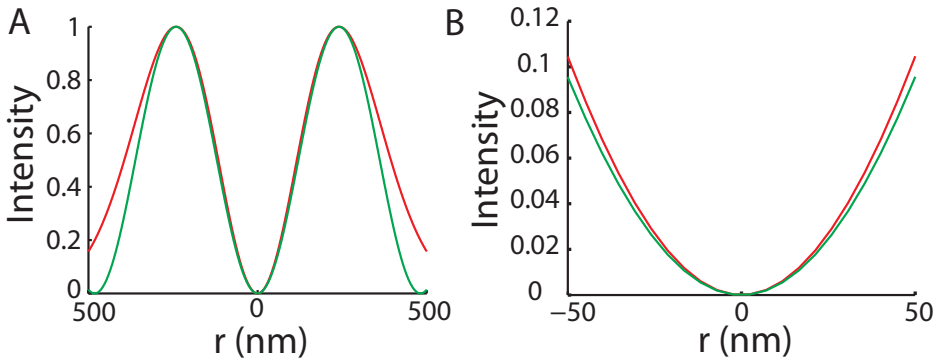

Figure 1.9: Intensity profiles of a doughnut beam, calculated with a LG(0,1) function (green) and a sinus function (red). The two profiles overlap well around the doughnut center, with intensity differences within 10%.

In the vicinity of the zero-intensity position, the STED profile is a parabola and its intensity distribution can be approximated as:

$$I_{donut}(r) \approx I_{STED}(\frac{\pi r}{d})^2. \tag{1.12}$$

Using Equation 1.8 and Equation 1.9, the PSF of pulsed-STED microscopy writes:

$$h_p(r) = h_{conf}(r)\, \eta_{rad}\, exp(-\Gamma t_p)\, exp(-\frac{\pi^2 r^2}{d^2}\, \frac{\sigma \lambda}{hc}\, I_{STED}\, T_p). \tag{1.13}$$

The resolution of STED microscopy can be defined as the FWHM of its PSF $h_p(r)$

and is given by:

$$\begin{aligned} \Delta r_p &= d_c \Big/ \sqrt{1 + \frac{\pi^2 d_c^2}{4d^2} \frac{\sigma\lambda}{ln2\, hc} I_{STED}\, T_p} \\ &= d_c \Big/ \sqrt{1 + \frac{\pi^2 d_c^2}{4d^2} \frac{I_{STED}}{I_S}}. \end{aligned} \tag{1.14}$$

Equation 1.14 shows that at high STED intensities, i.e. $I_{STED} \gg I_S$, the STED resolution scales with $1/\sqrt{I_{STED}/I_S}$. In order to obtain high resolution, one can use high STED intensities. By applying STED intensity up to several GW/cm^2, resolutions less than ten nanometers have been achieved with single N-V centers in diamond [93,94].

1.2.1.4 Calculation of the resolution of gated continuous-STED

Pulsed-STED microscopy provides the most efficient fluorescence depletion, since it provides high laser peak intensities and the laser sequences can be optimized for efficient STED action. However, this configuration usually requires careful synchronization of the excitation and STED lasers and the use of complex and costly laser assemblies such as mode-locked laser systems [86, 95]. A simplification to STED microscopy has therefore been realized with continuous-wave (CW) lasers for both excitation and depletion [96]. However, in CW-STED, the STED energy is stretched out and the depletion occurs gradually after the excitation of molecules. Consequently, a non-negligible part of the molecules emit fluorescence before having been sufficiently exposed to the STED light. This will lead to residual fluorescence outside the zero-intensity point of the STED light which adds a pedestal in the effective STED PSF, resulting in increased image blur. A remedy to this is using a time-gated detection scheme, referred to as "gated-STED" [97, 98]. In this case, a CW STED laser is used in combination with a pulsed excitation laser, the detection begins after a delay time T_g from the arrival of the excitation pulses, as shown in Figure 1.10.

To explain why time-gated detection can improve the performances of CW-STED,

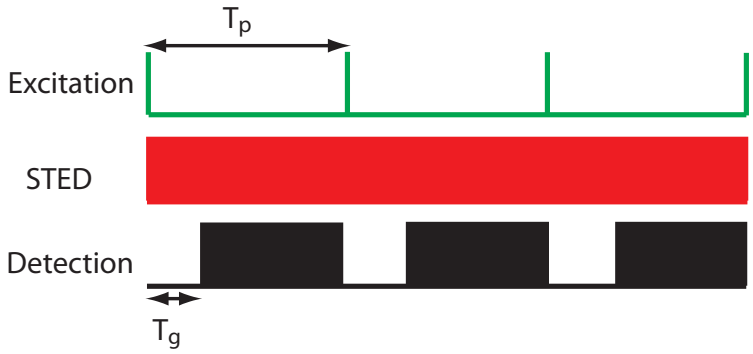

Figure 1.10: Laser sequences and the detection scheme in gated-STED. Excitation pulses are typically of a few picosecond and can be therefore considered instantaneous, whereas the STED beam is continuous. Detection is delayed for T_g after the arrival of the excitation pulses.

we will compare the temporal PSFs of pulsed-STED and gated-STED microscopies. The temporal PSF is defined as the spatial distribution of the fluorescence emission rate of the fluorophores at a given time, which is proportional to the population of S_1.

For $0 \leq t \leq T_p$, the temporal PSF of pulsed-STED writes:

$$\tilde{h}_p(t,r) = h_{conf}(r)\,\eta_{rad}\Gamma\,exp(-\Gamma t)\,exp(-\frac{\pi^2 r^2}{d^2}\frac{\sigma\lambda}{hc}I_{STED}\frac{T_p}{t_p}\,min(t,t_p)). \tag{1.15}$$

In the case of gated-STED, the temporal evolutions of the populations of S_0^* and S_1 follow the same equations as pulsed-STED, with the only difference that t_p equals to T_p. For $0 \leq t \leq T_p$, the temporal PSF of gated-STED is given by:

$$\tilde{h}_g(t,r) = h_{conf}(r)\,\eta_{rad}\Gamma\,exp(-\Gamma t)\,exp(-\frac{\pi^2 r^2}{d^2}\frac{\sigma\lambda}{hc}I_{STED}\,t). \tag{1.16}$$

In Figure 1.11, we show simulations of the temporal PSFs in the gated-STED and pulsed-STED configurations. In pulsed-STED, the STED pulses reach the focal plane virtually simultaneously or within a few picoseconds after the excitation pulses so as to instantly inhibit fluorescence emission from excited molecules. In gated-STED case, the

STED process takes place during the whole temporal interval between excitation cycles. Molecules can in principle emit fluorescence before having been de-excited by the STED light, which enlarges the effective STED PSF.

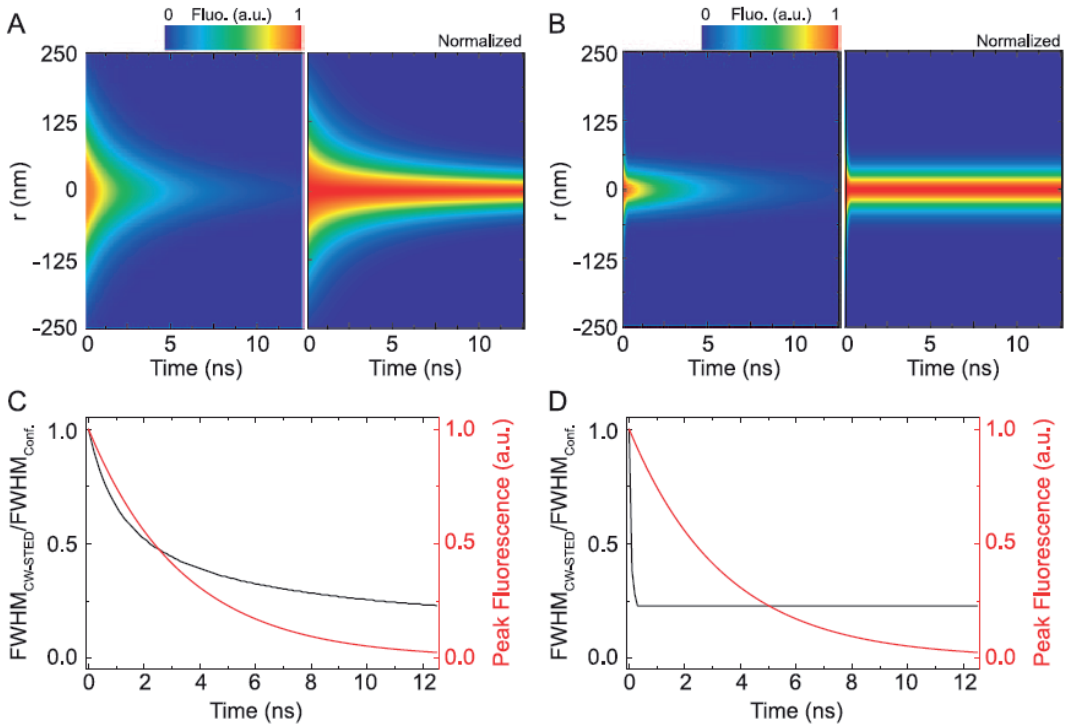

Figure 1.11: Temporal evolution of the PSF of STED microscopy. (A) and (C) for CW-STED configuration; (B) and (D) for pulsed-STED configuration. (A) (or B) Lateral intensity distribution $\tilde{h}_g(t,r)$ (or $\tilde{h}_p(t,r)$) (left panel: normalized by $\eta_{rad}\Gamma$; right panel: normalization to 1 at each time). (C) (or D) FWHM (black, left axis) and the peak signal $\tilde{h}_g(t,0)$ (or $\tilde{h}_p(t,0)$) (red, right axis) of the STED PSF as a function of time (excitation at time 0). Calculated for an objective of NA = 1.4, $\tau = 3.4$ ns, $T_p = 12.5$ ns, $t_p = 300$ ps, excitation wavelength 635 nm, STED wavelength 760 nm, the same average intensities for both configurations, with $I_{STED} = 25 I_S$. Figure extracted from [99].

A time-gated detection can therefore improve the resolution of CW-STED by rejecting the early fluorescence, where the temporal PSF is large.

More precisely, the effective PSF of gated-STED writes:

$$\begin{aligned} h_g(r) &= h_{conf}(r)\,\eta_{rad}\Gamma\int_{T_g}^{T_p} P_{S1}(t)dt \\ &\approx h_{conf}(r)\,\eta_{rad}\,exp(-\Gamma T_g)\,exp(-\frac{\pi^2 r^2}{d^2}\frac{\sigma\lambda}{hc}I_{STED}\,T_g) \\ &\quad (1+\frac{\pi^2 r^2}{d^2}\frac{\sigma\lambda}{hc}I_{STED}\,\tau)^{-1} \end{aligned} \tag{1.17}$$

In the absence of gating ($T_g = 0$), the PSF of CW-STED has a Lorentzian shape. When a gated detection is applied ($T_g > 0$), the PSF consists of a Gaussian term and a Lorentzian term. The Gaussian term reflects the fluorescence depletion due to the STED action before the detection. By replacing the Lorentzian term with a Gaussian term having the same FWHM, the FWHM of the gated-STED PSF is given by:

$$\Delta r_g = d_c \Big/ \sqrt{1+\frac{\pi^2 d_c^2}{4d^2}\frac{\sigma\lambda}{ln2\,hc}I_{STED}\,(ln2\,\tau+T_g)} \tag{1.18}$$

Note that the resolution of CW-STED without time-gated detection can be obtained from Equation 1.18 by setting $T_g = 0$. For pulsed-STED the resolution depends on the pulse energy $I_{STED}T_p$, whereas for gated-STED it depends on $I_{STED}(ln2\,\tau + T_g)$. Therefore higher laser powers have to be applied in CW-STED to achieve the same resolution as in pulsed-STED, typically by about a factor of five $(T_p/(ln2\,\tau + T_g))$.

A sharpening of the PSF of gated-STED is obtained with increasing time delay T_g, at the expense of a decrease in fluorescence signal. The PSF of gated-STED can also be regarded as a weighted sum of different Gaussian distributions with decreasing FWHMs and decreasing weights represented by the temporal PSF. Collecting the photons after a time delay Tg from the excitation pulse, i.e. performing time-gated detection, removes the early temporal PSFs with larger FWHMs and therefore improves the effective resolution at the expense of a loss in overall signal, as outlined in Figures 1.11.

1.2.1.5 Other developments in STED microscopy

Besides CW-STED, another development for setup simplification was proposed under the acronym easySTED microscopy [100]. It uses a special phase plate which selectively modulates the phase of the STED beam but leaves the excitation beam unaffected, so that the excitation and STED beams can share the same optical path. The alignment requirements and the mechanical drifts are both reduced in this case.

Dual-color STED is an important development to determine the relative sites and proximities of different molecules in specimens. For this purpose, two pairs of excitation/depletion beams, each pair exciting and depleting one specific emitter, can be used [101, 102]. This approach has several drawbacks due to its complexity, cost and the cross-photobleaching of the more red-emitting dyes by the STED lasers with shorter wavelength. A preferable approach for dual-color STED is to use fluorophores with partially overlapping emission spectra so that only one depletion beam is needed for both fluorophores. In this case, the two fluorophores are either excited at different wavelengths [103, 104] or detected in two spectral channels [105].

In many STED microscopy applications, imaging with two-dimensional resolution enhancement is good enough to reveal details of molecular assemblies. Still, many applications require imaging with super-resolution in all three dimensions. Two-photon excitation STED allows imaging in thick brain tissues [106–108], however with the axial resolution being diffraction-limited. To improve resolutions along all spatial directions, different phase plates have been adapted in STED microscopy to create the desired fluorescence restriction [109–111]. The implementation of adaptive optics has further allowed three-dimensional super-resolution imaging in strongly aberrating specimen [45]. More complex setups for three-dimensional STED have been realized in combination with 4Pi microscopy [104, 112] or with light-sheet microscopy [113].

STED microscopy has showed applications in immuno-stained fixed samples [114], lithography [115, 116], condensed matter [117] and living cells [47, 48]. It has been

also combined with fluorescence correlation spectroscopy, which allows a more detailed investigation of molecular interaction at small spatial scales [118, 119].

1.2.1.6 Generalization of STED principle

STED microscopy can be generalized to other methods based on different fluorescence depletion processes. Reversible saturable optical fluorescence transitions (RESOLFT) is a general term which represents such methods. Ground state depletion (GSD) microscopy [35] depletes the ground state of the emitter either by pumping it to the excited state [120] or to a metastable dark state [121]. RESOLFT methods using reversible photoswitchable proteins have been also demonstrated [41, 122, 123]. To be switched "on" and "off", reversible photoswitchable proteins require low light intensity, which reduces the bleaching of the fluorophores and the photo-toxicity to the sample. However, protein switching is a relatively slow on-off process (10 ms), which sets a limit to the imaging acquisition rate.

1.2.2 Structured illumination microscopy

Structured illumination microscopy (SIM) uses spatially modulated (e.g. sinusoidal) intensity patterns to illuminate the sample. The period patterns can be obtained by two-beam interference, as shown in Figure 1.12A. An object containing fine details can be decomposed in Fourier components where the finer details are encoded in the higher frequencies. Suppose that an object, which has a single Fourier component, is illuminated by a period pattern, the resulting image contains "moire fringes" at lower frequencies than the original object, and can become observable by the microscope even if the original object is too fine to resolve (see Figure 1.12B). The illumination pattern needs to be scanned within a period (by changing the relative phases between the two beams) and be rotated, to render isotropic lateral resolution. A camera acquires successive wide-field images during the scan and the rotation. Post data-processing is required in order to

retrieve an image of the object, with resolution improved by a factor of two compared to the diffraction-limited resolution.

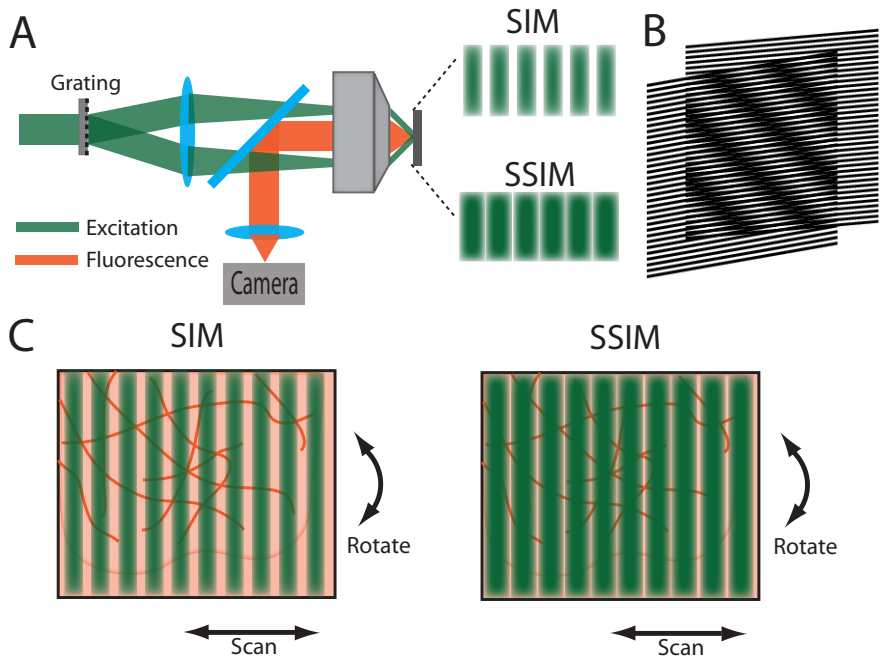

Figure 1.12: Principle of SIM and SSIM microscopy. (A) Diagram of the experimental setup. A grating diffracts the excitation beam into two beams which recombine on the sample to create one-dimensional periodic structures. SIM applies low excitation intensities whereas SSIM applies high intensities to saturate the fluorophores. A camera acquires fluorescence images. (B) Moire effect. Two overlapping fine patterns generate a beat pattern which contains lower frequencies than the original patterns. (C) The camera acquires successive wide-field images while the illumination pattern is scanned and rotated. Post data-processing is needed to reconstruct a super-resolution image.

Multicolor and three-dimensional resolution enhancement with SIM has been realized [124]. Live cell imaging has also been demonstrated [125]. Instead of the period patterns, SIM can be also performed with unknown speckle illumination [126]. SIM has been combined with tunable surface plasmon interference as an illumination source to offer higher resolution in the near-field [127].

Saturated structured illumination microscopy (SSIM) applies modulated patterns with higher excitation intensities to saturate the fluorescence emission of the fluorophores.

Under such strong excitation, most emitter molecules are pumped to the excited state, additional intensity increases will not yield proportional increases in the emission rate. The effective applied modulation pattern is not sinusoidal any more, but contains higher frequency components. The saturation effect therefore can further improve the resolution. From another viewpoint, SSIM can be seen as 'negative' imaging methods. The super-resolution information is from the valleys of the illumination pattern where the fluorophores are not excited and therefore do not fluoresce. SSIM simply confines the regions where fluorophores do not emit fluorescence to a smaller volume which offers better resolution. Since SSIM applies high laser intensities on the fluorophores, its implementation was long impeded by the photobleaching of the fluorophores. The first experimental realization of SSIM was then based on photoswitchable proteins [128].

1.2.3 Localization based super-resolution techniques

1.2.3.1 Principles

An image of a sample labelled with fluorophores is essentially defined by the spatial coordinates of each emitter convoluted by the PSF of the microscope. If one can determine the position of each emitter individually with precision better that the diffraction-limited resolution, a super-resolution image could be reconstructed by assigning corresponding coordinates to the fluorophores. Indeed, for an isolated emitter, although its image is a finite spot (see Figure.1.13A), its position can be determined with high precision by fitting the image with a two-dimensional Gaussian function (approximation of the PSF). For a shot noise limited detection, the localization precision in the transverse plane is given by:

$$\sigma_{x,y} \approx \frac{\Delta r}{\sqrt{N}} \tag{1.19}$$

where Δr is the FWHM of the PSF and N is the photon number. Given the fact that more than 10^4 photons can be detected from a single emitter, the localization precision

can reach $\sim$ 1 nm [129, 130].

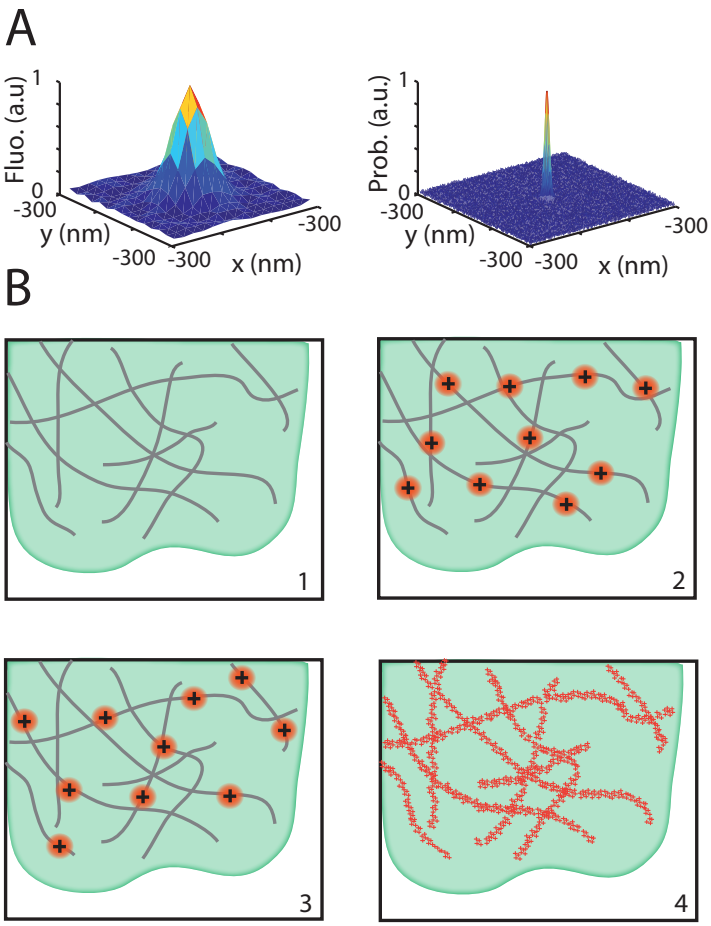

Figure 1.13: Principle of super-resolution methods based on single molecule localization. (A) Single molecule localization. Left side is a diffraction-limited image of a fluorphore. Right side is the localization precision of its centroid. (B) Super-resolution process. The sample shown in B.1 is labelled with thousands of fluorophores. Only a subset of the fluorophores is allowed to fluoresce and imaged each time, their positions are then localized (B.2 and B.3). Repeating this process until a large number of fluorophores are localized, one can reconstruct a super-resolution image (B.4). Figure adapted by the author from [84].

In general, a biological sample is labelled with hundreds up to millions of fluorophores at high density. Under excitation, all fluorophores simultaneously emit photons, leading

to overlapped "single molecule images". Therefore it becomes impossible to localize the positions of each fluorophore. In order to perform super-resolution imaging, strategies are used where only a subset of fluorophores are allowed to fluoresce and imaged in each raw image. The number of emitting fluorophores is small so that they can be optically resolved and localized individually. The positions of the fluorophores are mapped and these fluorophores are subsequently desactivated (or photobleached). A new subset of fluorophores are then imaged, localized and desactivated. Iterating this process until a large number of fluorophores are localized and mapped will reveal the ultrastructures of the sample with super-resolution, as shown in Figure1.13B.

1.2.3.2 Different approaches to sequentially image isolated single molecules

Different approaches have been implemented, distinguishing how fluorescent molecules are stochastically isolated from nonfluorescent ones.

The development of PALM [28,29] is closely linked to the advent of photoactivatable proteins, which allows the optical control of the density of fluorescing proteins in each raw image. Although it is restricted to expression systems, preventing the study of endogenous proteins in their native environment, PALM has the advantage of being versatile and specific and allows the study of intracellular biomolecules. By tracking the movement of individual proteins, PALM can be used to measure local diffusion properties in living cells on short timescales [131–133] and cellular structural changes in three dimensions on longer timescales [134].

STORM [30] and dSTORM [31] use switchable organic fluorophores placed in specific buffers (e.g. with reducing properties) instead of using fluorescent proteins as in PALM. Those probes can be targeted on genetically encoded or endogenous proteins using adequate ligands. STORM was first demonstrated using Cy3-Cy5 pairs [30] but was quickly extended in dSTORM to other synthetic fluorophores which can be stochastically and reversibly switched in imaging buffers. STORM and dSTORM are particularly pow-

erful for fixed cell applications [135–137]. Analogously to dSTORM, where stochastic photoswitching is applied to control the number of emitting fluorophores, ground state depletion microscopy followed by individual molecular return (GSDIM) [138] employs the transition between the fluorescent singlet state and the metastable triplet state as a stochastic on-off switch. More precisely, the majority of fluorophores are switched to the long-lived triplet state by using high excitation intensities together with an imaging buffer (triplet quencher). The triplet state lifetime is long enough ($\sim$ 100 μs - 100 ms) to leave only a few fluorophores at singlet states at any time in each image. Under these conditions, GSDIM has been employed for imaging living cells using both fluorescent protein tags [139] (as in PALM) or various organic fluorophores (as in STORM) that selectively bind to tagged proteins [140].

In contrast to PALM, STORM and GSDIM, which are based on the stochastic photoswitching of the emitters, (u)PAINT [32, 33] captures real-time molecular interactions to control the density of fluorescent emitters in each image. In uPAINT, target molecules are individually imaged when binding to a specific ligand coupled to a fluorescent dye. Unbound ligands freely diffuse in the imaging buffer with typical diffusion constants of $\sim$ tens of $\mu m^2/s$, in contrast to bound ligands, which diffuse together with a membrane receptor with typical diffusion constants of <1 $\mu m^2/s$. Due to an oblique illumination, unbound ligands are not excited in an efficient manner and are therefore not detected efficiently by a detector operating at a typical video rate. With uPAINT, any binding entity conjugated to fluorophores having high specificity toward a target molecule (e.g., natural/synthetic ligand, antibody) can be used as fluorescent probes to reveal the target molecule. uPAINT has been applied to image and track endogenous receptors such as glutamate receptors in neurons [33] and epidermal growth factor receptors (EGFRs) at high densities in culture living cells [141].

1.2.3.3 Other developments in localization-based techniques

Three-dimensional super-resolution has been achieved with localization based techniques by also localizing the positions of the fluorophores along the z-axis, with the engineering of the detection PSF. This can be done by using a cylindrical lens to introduce astigmatism [135], dual focal-plane imaging [142] and double-helix PSF imaging [143]. Multi-color imaging can be achieved either by using fluorophores with different activation wavelengths [144–146] or (and) with different emission wavelengths [147, 148].

The fluorophores are dipoles with different orientations, thus they are either fixed in the specimen or have certain degree of rotational mobility. While the emission PSFs of rotating fluorophores can be well fitted with a two-dimensional Gaussian function [149], those of fluorophores with fixed orientation cannot, which induces localization bias [150]. When imaging molecules with quasi-fixed orientations, several methods [151, 152] allow measuring the molecular orientation and subsequently correcting the localization bias.

1.2.4 Other super-resolution methods

Besides these three major super-resolution techniques, other methods based on distinct mechanisms have also been proposed and realized.

1.2.4.1 Saturated excitation microscopy

Saturated excitation in confocal microscopy has been used to improve the spatial resolution [153,154]. Similar as in SSIM, high excitation intensity is applied and the fluorescence signal is saturated. Consequently, the excitation PSF gets flattened and widened, which contains high spatial frequency components. Since these high spatial frequency components occur first at the peak of the laser excitation, they carry structural information on a scale that is smaller than the PSF and thus, may be used to improve resolution in all three dimensions. In contrast to SSIM, the high spatial frequency is extracted by modulating the excitation intensity at a frequency (ω) and by demodulating the flu-

orescence intensity at the corresponding harmonic frequencies (2ω, 3ω, . . .). When the excitation intensity is high enough to generate saturation in fluorescence excitation, harmonic frequencies appear in the modulated fluorescence signal because the relationship between fluorescence and excitation intensity becomes nonlinear. This effect can be seen prominently at the center of the PSF of excitation, and can be used to detect fluorescence intensity at the position close to the center of PSF. This technique has been recently extended to other saturation effects to perform super-resolution, such as the scattering saturation of single gold nanoparticles [155, 156].

1.2.4.2 Super-resolution optical fluctuation imaging

Dertinger et al. introduced a concept for resolution enhancement referred to as super-resolution optical fluctuation imaging (SOFI), which is based on higher-order statistical analysis of temporal fluorescence fluctuations recorded in a sequence of images (movie) [157–159]. To perform SOFI, several requirements needs to be satisfied: (i) the fluorophores have to exhibit at least two different emission states; (ii) different emitters have to switch between states repeatedly and independently from each other in a stochastic way; (iii) the image should be acquired with pixels smaller than the diffraction limit. The pixel value of a SOFI image (of the order n) is obtained from the n^{th}-order cumulant (a quantity related to the n^{th}-order correlation function) of the original pixel time series. The signal in a pixel of conventional wide-field images is given by the sum of the fluorescence originating from different, nearby emitters. The n^{th}-order cumulant filters this signal based on its fluctuations in such a way that only highly correlated fluctuations are left over. Since the fluorescence signal contribution of emitters to neighbouring pixels will nonlinearly yield lower correlation values, the higher order signal is limited to emitters within the pixel, which leads to an increased resolution. In contrast to the localization-based techniques, SOFI enables the separation of fluorophores with spatially overlapping diffraction patterns.

1.2.4.3 Super resolution by polarization demodulation

When excited with rotating linear polarized light, differently oriented fluorophores emit periodic signals peaking at different times. The measurement of the average orientation of fluorescent dyes attached to rigid sample structures mapped to regularly defined image nanoareas (typically 50 nm by 50 nm) can provide sub-diffraction resolution. Because the polarization angle range for effective excitation of an oriented molecule is rather broad and unspecific, this range can be narrowed by simultaneous irradiation with a second, de-excitation, beam possessing a polarization perpendicular to the excitation beam. The shortened periodic emission flashes allows better discrimination between molecules or nanoareas. This method has been implemented to standard wide-field microscopy with camera detection and to two-photon scanning microscopy, to image the fine structural details of neuronal spines [160].

C H A P I T E R 2

Parallelization of STED microscopy with optical lattices

The aim of this chapter is to present the technique that we developed to massively parellelize STED microscopy. After discussing the motivations, I will describe the method of STED parallelization based on optical lattices. The experimental realization of the parallellized Lattice-STED microscopy is then detailed, followed by the presentation of experimental results. A summary and a discussion of the perspectives of Lattice-STED microscopy are given at the end of this chapter.

2.1 Motivations

Super-resolution optical microscopy methods [161] provide resolutions far beyond the diffraction limit, down to nanometer scale. The break of the diffraction barrier relies on the sequential selective imaging of fluorescent emitters, which are detected one after another in a diffraction-limited volume and consequently become resolvable. This sequential imaging modality implies that the resolution gain is at the expense of the imaging speed, which could be a severe limitation when studying dynamic structures in living cells. Indeed, many biological phenomena occur at timescales from milliseconds to seconds, such as the movement of synaptic vesicles in neurons [47], the morphological deformation of the dendritic spines [48] and the motion of the cell-surface receptors [42,44].

Therefore, fast super-resolution microscopies are crucial for the study of such phenomena.

The trade-off between the spatial and temporal resolutions of super-resolution microscopy can be also explained in terms of sufficient sampling density. According to the Nyquist criterion [162], the size of the pixel of an image must be smaller than half of the desired resolution. Therefore compared to a diffraction-limited image, a super-resolution image needs N^D times more pixels if a N-fold resolution improvement is achieved in D dimensions.

We now discuss the imaging speed of several super-resolution microscopy methods in two dimensions.

Localization-based methods are intrinsically parallelized. They use wide-field illumination together with a camera for detection, which records simultaneously fluorescence images of multiple emitters. An emitter should be well separated spatially from the others, in order that its PSF can be fitted independently to determine the centroid with high precision. To reveal the nanostructure of the sample, a sufficient number of emitters needs to be imaged and localized. Two factors need to be considered for the imaging speed of these techniques: the density of the fluorescing emitters per raw image and the stochastic imaging process. Naturally, the higher the density of fluorescing emitters is, the less the raw images are needed to reconstruct a super-resolution image, and therefore the faster the imaging speed is. Different algorithms [40, 42, 163] have been developed for fitting the positions of emitters, with densities up to 10 μm^{-2} [40, 164] corresponding to $\sim$ 0.5 emitters per focal spot (FWHM $\sim$ 250 nm). Compared with other super-resolution methods, the stochastic imaging techniques have the drawback of slow imaging speed. The structure of interest in the field of view can be regarded as pixelized with pixels, i.e. formed by pixels named "Nyquist-pixel" having the size determined by the Nyquist criteria. To form a super-resolution image of the structure, at least one localization event should take place at each Nyquist-pixel. Due to the stochastic

character of the imaging process, more than one localization event could be registered at a Nyquist-pixel, which causes redundant sampling. However, the stochastic imaging process offers an advantage when imaging a sample of sparse sub-diffraction structures, such as transferrins in cells [44]. Each localization event surely occurs at the position of the structures, only a few raw images are required to reveal the structures of the sample. As demonstrated in [44] (see Figure 2.1), only $\sim$ 200 raw images are used to reconstruct a super-resolution image. The imaging speed of localization-based methods is thus determined by the aforementioned factors, and is usually between a few seconds per image to tens of minutes per image.

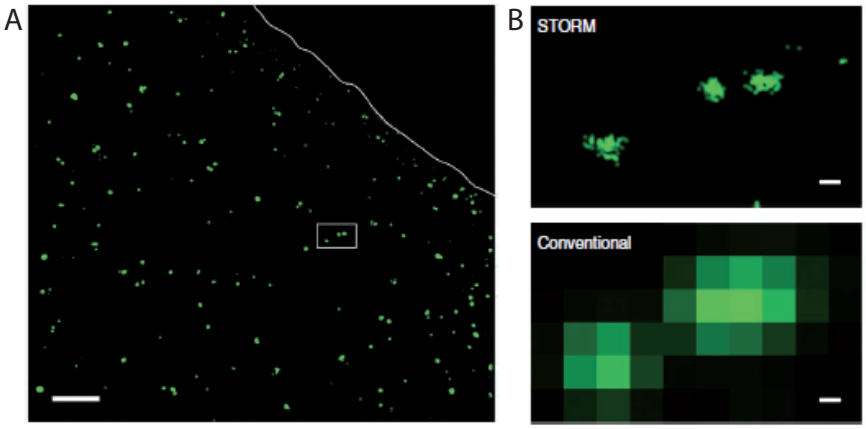

Figure 2.1: STORM images of transferrin in live cells. (A) Wide-field two-dimensional STORM image. (B) Close-up STORM (top) and conventional (bottom) images of the boxed region in A. Scale bars, 2 μm (A) and 100 nm (B). Figure extracted from [44].

SIM is also a parallelized microscopy [36]. To illuminate the sample, it applies periodic patterns, which are scanned and rotated to render isotropic resolution. For each scan and rotation, the camera acquires one raw image. In total, 9 raw images are acquired to reconstruct a super-resolution image. It is possible to achieve video-rate imaging (11 Hz super-resolution image rate) with SIM, which however only offers a 2-fold resolution enhancement [125]. SSIM can achieve better resolution [128], but at the expense of acquiring more raw images with a rather long exposure time, up to several

hundreds of ms [128], in order to perform post-processing of raw data. Thus the imaging speed of SSIM is from several seconds to tens of seconds per super-resolution image.

STED microscopy is a point-scanning microscopy [82]. It requires only a limited number of fluorescence photons, to obtain the molecular density at the position of the emission. It thus allows pixel dwell times down to several tens of μs [47], significantly shorter than other super-resolution microscopies. However, a drawback of STED microscopy is that its detection is not parallelized so that its imaging speed depends strongly on the size of the desired field of view. The parallelization of STED microscopy will make it possible to achieve fast wide-field imaging.

A straightforward approach for STED parallelization would be the duplication of the exictation/STED beam pair. A four-fold improvement of the imaging speed has been achieved using this approach [165], with four separated excitation/depletion beam pairs, together with four corresponding point-detectors for detection (see Figure 2.2). However, multi-doughnut STED faces a major limitation that the experimental setup will be very complicated for large parallelization.

Our approach is to use well-designed optical lattices to provide efficient depletion patterns for large parallelization of STED microscopy.

2.2 Optical lattices for STED parallelization

Optical lattices are periodic patterns generated by multi-beam interferences. They were first introduced for trapping cold atoms [166,167]. Their applications are then extended to other fields such as photonic crystal fabrication [168] and microfluidics [169]. Our target optical lattice should contain an array of zero-intensity minima, each of which surrounded by nearly isotropic intensity distribution. In Lattice-STED, each zero-intensity region plays the same role as the doughnut beam in doughnut-STED. To obtain a super-resolution image, the sample only needs to be scanned over a **unit cell** of the optical

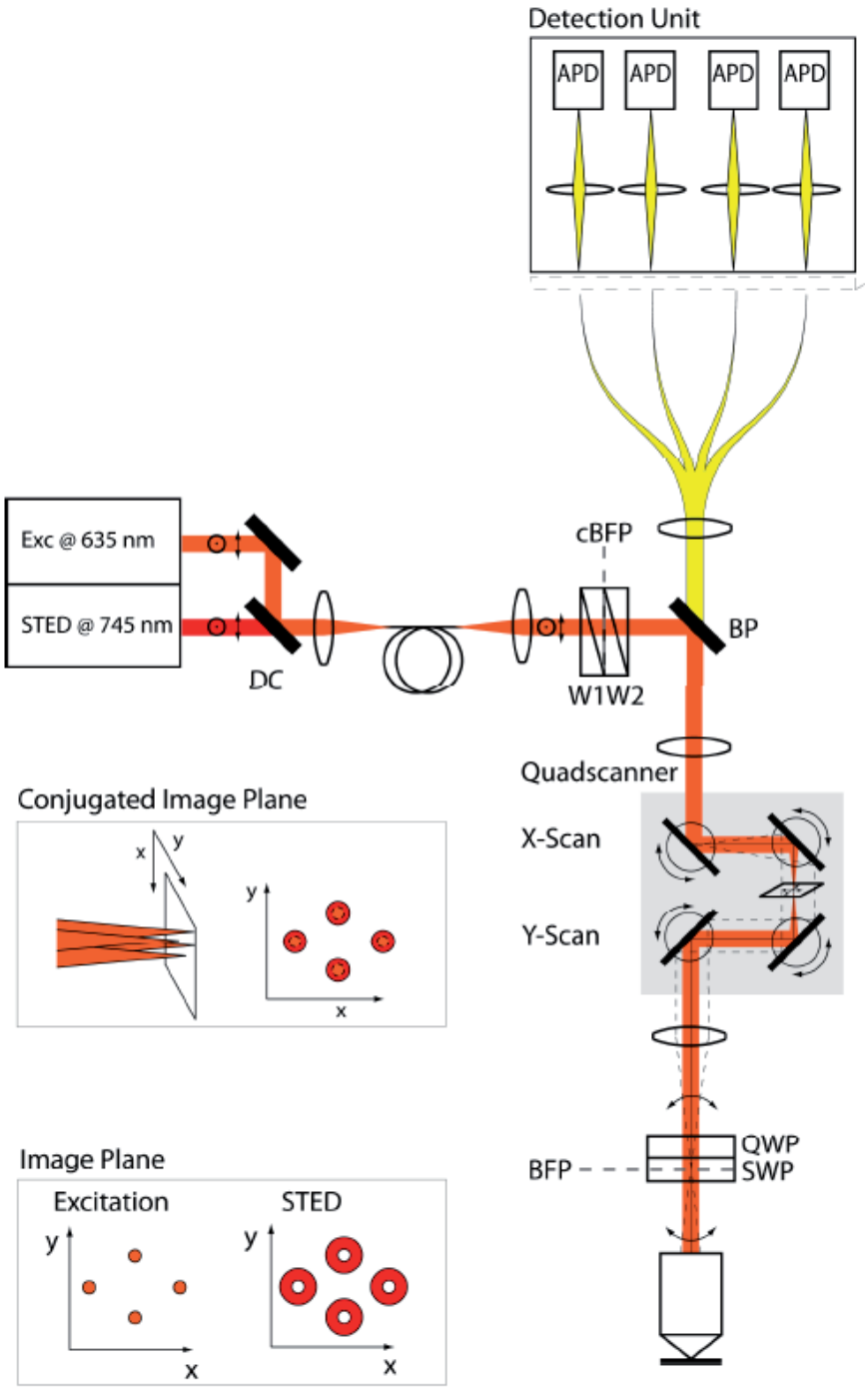

Figure 2.2: Multi-doughnut STED setup realized by Hell and co-workers in 2011 (extracted from [165]). The STED and excitation beams follow the same optical path. Two Wollaston prisms split both beams in four parts. A special optical shaping device (SWP) converts the STED beams into doughnut-shaped and leaves the excitation beams unaffected. Four dedicated avalanche photodiodes, conjugated with the sample plane, are used to collect the fluorescence.

lattice instead of over the entire field of view. During the scan, a two-dimensional detector can be used for parallelized detection. This will drastically improve the imaging speed of STED microscopy and allow fast wide-field super-resolution imaging.

The topographies of electric field and of intensity of the optical lattices depend on the relative directions, polarizations and phases of the interfering beams. Significant shifts or drifts of beam phases could modify the topographies of the optical lattice. If the number of independent interfering beams p and the spatial dimension of the optical lattice n satisfy the relation: $p-1=n$, variations of beam phases will only translate the optical lattice but its topography of electric field will remain the same.

To demonstrate this, we first write the total electric field $\vec{E}(\vec{r},t)$ of the interference pattern as the sum of the plane waves $\vec{E_j}(\vec{r},t)$:

$$\vec{E}(\vec{r},t)=\sum_{j=1,p}\vec{E_j}(\vec{r},t)=\sum_{j=1,p}\mathcal{E}\vec{e_j}e^{i\vec{k_j}.\vec{r}}e^{-i\omega t}e^{i\phi_j} \tag{2.1}$$

where $\mathcal{E}$, k_j, ω, ϕ_j and $\vec{e_j}$ are respectively the amplitude, the wave vector, the angular frequency, the phase and the polarization of the plane wave.

Equation 2.1 can be written as:

$$\vec{E}(\vec{r},t)=\mathcal{E}e^{i\vec{k_p}.\vec{r}}e^{-i\omega t}e^{i\phi_p}\Big(\vec{e_p}+\sum_{j=1,p-1}\vec{e_j}e^{i(\vec{k_j}-\vec{k_p}).\vec{r}}e^{i(\phi_j-\phi_p)}\Big). \tag{2.2}$$

Since the arbitrary choice of the time origin ($t=t^{'}+t_o$) allows cancelling the phase ϕ_p, the number of independent relative phases in Equation 2.2 is p-1. Furthermore, the arbitrary choice of the space origin ($\vec{r}=\vec{r}^{'}+\vec{r}_o$) allows rewriting the sum of Equation 2.2 as:

$$\sum_{j=1,p-1}\vec{e_j}e^{i(\vec{k_j}-\vec{k_p}).\vec{r}^{'}}e^{i[\phi_j-\phi_p+(\vec{k_j}-\vec{k_p}).\vec{r_0}]}. \tag{2.3}$$

It clearly shows that the relative phase variations can be compensated by spatial

translations of $\vec{r_0}$, if the following equations have solutions:

$$\phi_j - \phi_p + (\vec{k_j} - \vec{k_p}) \cdot \vec{r_0} = 0. \tag{2.4}$$

Equation 2.4 is a system of $p-1$ linear equations with n variables. For independent vectors $\vec{k_j} - \vec{k_p}$ $(1 \leq j \leq p-1)$, the system has a solution if:

$$p - 1 = n. \tag{2.5}$$

Two configurations have been used for the generation of two-dimensional optical lattices: three- and four-beam interference. The three-beam optical lattice has both the topographies of electric field and of intensity invariable to the beam phases. Although the four-beam optical lattice has the topography of electric field depending on the beam phases, we will show that in certain conditions its topography of intensity can still be invariable to the beam phases.

2.2.1 Three-beam interference optical lattices

To build the three-beam optical lattice in the focal plane of a high NA objective suitable for STED parallelization, we consider three beams propagating along the optical axis $\vec{e_z}$ of the objective, with the same frequency ω, linear polarization along $\vec{e_x}$ and the same intensity, as shown in Figure 2.3. The beams intersect the objective at the vertices of a centred equilateral triangle. After passing through the objective they are deviated by an angle θ toward the focal region where they interfere and form an optical lattice. The beams transmitted by the objective have wave vectors $\vec{k_j}$. α_j is the angle between the x-axis (polarization direction) and the projection of $\vec{k_j}$ in the x-y plane. The intensity distribution of the optical lattice is therefore determined by the angles α_j and θ. The incident beams are slightly focused Gaussian beams with beam waist located at the back focal plane of the objective. The transmitted beams are collimated and deviated by the

objective and have their polarizations rotated.

The polarization $\vec{e_j}$ and the wave vector $\vec{k_j}$ of the transmitted beam can be expressed respectively as (see Appendix.A.1 for details):

$$\vec{e_j} = \begin{pmatrix} cos^2\alpha_j\ cos\theta + sin^2\alpha_j \\ cos\alpha_j\ sin\alpha_j\ (cos\theta - 1) \\ -cos\alpha_j\ sin\theta \end{pmatrix}, j = 1, 2, 3 \tag{2.6}$$

and

$$\vec{k_j} = \begin{pmatrix} -cos\alpha_j\ sin\theta \\ -sin\alpha_j\ sin\theta \\ cos\theta \end{pmatrix} k, , j = 1, 2, 3 \tag{2.7}$$

where $k = 2\pi n/\lambda$, $\alpha_1 = \alpha$, $\alpha_2 = \alpha + 120°$ and $\alpha_3 = \alpha + 240°$.

We approximate the field of a transmitted beam by a plane wave with amplitude $\mathcal{E}$

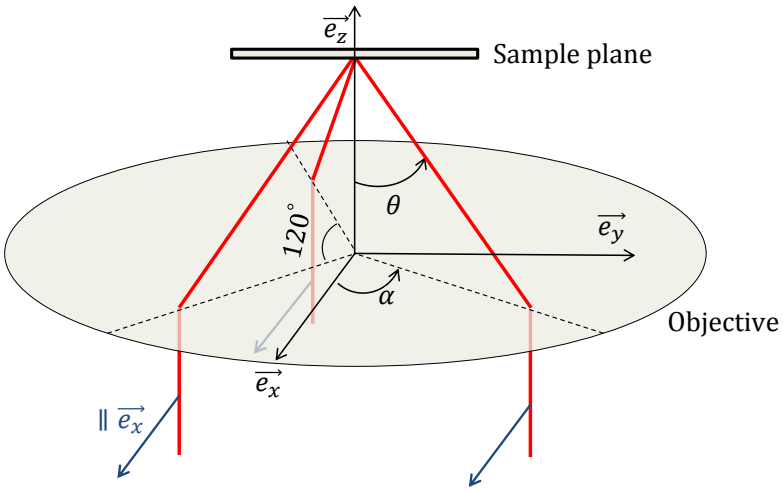

Figure 2.3: Geometrical configuration of the three beams arriving on the sample plane. The three beams have the same polarization (along the x-axis) and propagate parallel to the optical axis before the objective. They intersect the back focal plane of the objective at the vertices of a centered equilateral triangle. Red lines show the wave vectors of the three beams, blue arrows indicate the polarizations.

as:

$$\vec{E_j}(\alpha_j, \theta) = \mathcal{E}\vec{e_j}e^{i\vec{k_j}.\vec{r}}, j = 1, 2, 3. \tag{2.8}$$

The three beams then overlap in the focal plane of the objective (sample plane) and interfere. The intensity distribution of the interference pattern is given by:

$$\begin{aligned} I(\vec{r}) &= (\vec{E_1} + \vec{E_2} + \vec{E_3}) \cdot (\vec{E_1} + \vec{E_2} + \vec{E_3})^* \\ &= |\vec{E_1}|^2 + |\vec{E_2}|^2 + |\vec{E_3}|^2 + 2\mathcal{R}(\vec{E_1} \cdot \vec{E_2}^*) + 2\mathcal{R}(\vec{E_2} \cdot \vec{E_3}^*) \\ &\quad +2\mathcal{R}(\vec{E_3} \cdot \vec{E_1}^*), \end{aligned} \tag{2.9}$$

with

$$\begin{aligned} \mathcal{R}(\vec{E_p} \cdot \vec{E_q}^*) &= \mathcal{R}\Big(\mathcal{E}\vec{e_p}\, e^{i\vec{k_p}\,\vec{r}} \cdot \mathcal{E}\vec{e_q}\, e^{-i\vec{k_q}\,\vec{r}}\Big) \\ &= \mathcal{E}^2\vec{e_p} \cdot \vec{e_q} \cdot cos\Big(\Big(\vec{k_p} - \vec{k_q}\Big) \cdot \vec{r}\Big) \end{aligned} \tag{2.10}$$

where $p, q = 1, 2, 3$ and $p \neq q$.

The lattices have hexagonal structures with periodicity as a function of θ, given by (see AppendixA.2 for details):

$$p = \frac{2\lambda}{3n\ sin\theta}. \tag{2.11}$$

At θ= 60° and at STED wavelength λ= 760 nm, the period of the optical lattice is therefore 390 nm.

In Figure 2.4, we show that the intensity distribution of the three-beam optical lattices depends on α and θ. Varying α and θ affects the topography of electric field and also the topography of intensity within a unit cell of the lattice. The figures also show that the desired configuration (i.e. local zero-intensity minima, each of which surrounded by nearly isotropic intensity distribution) can be obtained at $\alpha = 30°$ and $\theta = 70°$. The

contrast of the interference pattern is defined as:

$$C(\theta, \alpha) = \frac{I_{max} - I_{min}}{I_{max} + I_{min}} \tag{2.12}$$

where I_{max} and I_{min} are respectively the maximal and minimal intensities in the interference pattern.

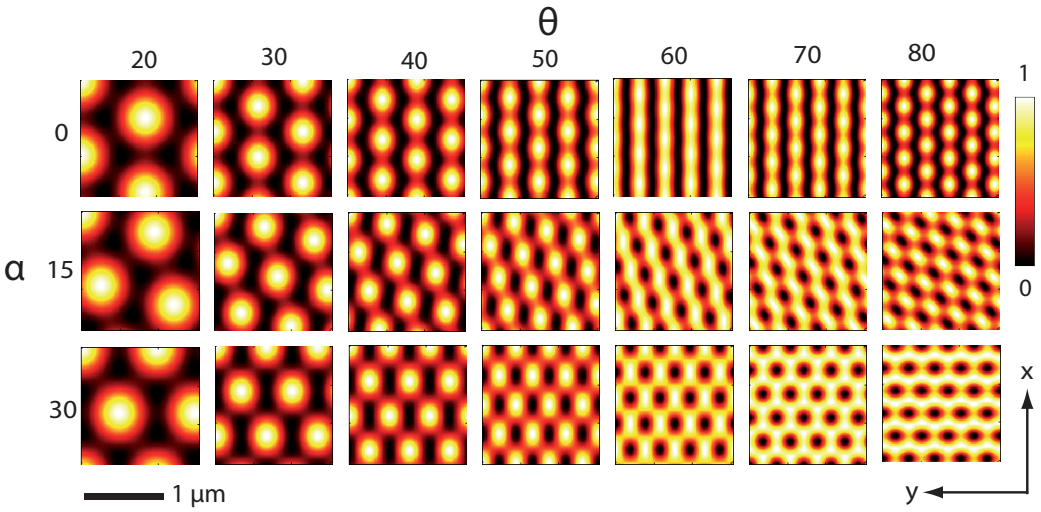

Figure 2.4: Simulations of the intensity distribution of three-beam optical lattices as a function of α and θ. Each image is the sum of the squared electric field components along the x-, y- and z-axes, and is normalized to its maximal intensity value. Simulated with $\lambda = 760$ nm and $n = 1.515$.

Figure 2.5A shows the three-dimensional plot of the contrast $C(\theta, \phi)$ as a function of α and θ. Clearly, the highest contrasts are obtained when α=30°. Figure 2.5B shows the evolution of the contrast as a function of θ for α=30°. The maximal contrast (more than 99.9%) is reached when θ=70°. In practice, the angle of incidence is limited both by the size of the beams at the back aperture of the objective and the size of the back aperture. In our experiment, a high NA objective (NA=1.49) is used, which allows an angle of incidence up to θ=60°, where the size of the beams is $\sim$ 1 mm and the size of the back aperture is 10 mm. At $\alpha = 30°$ and $\theta = 60°$, the theoretical contrast is still

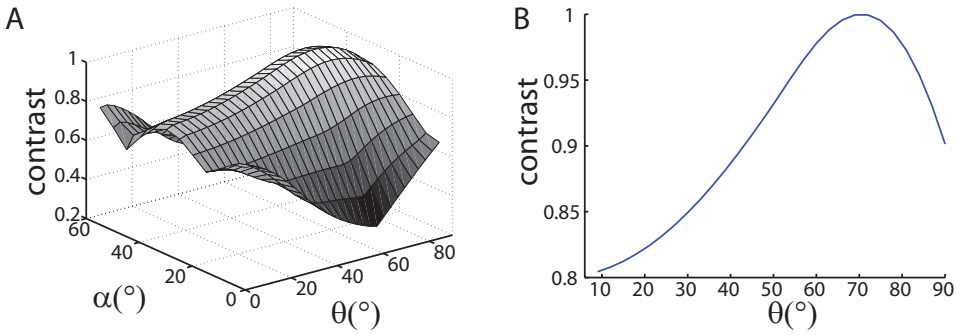

Figure 2.5: (A) Contrast of the three-beam interference pattern as a function of α and θ. (B) Evolution of the contrast for α=30° (optimal value).

close to unity (98%).

The topography of intensity of the interference pattern in the optimal experimental configuration, i.e. $\alpha = 30°$ and $\theta = 70°$, is obtained and shown in Figure 2.6A. The pattern displays a hexagonal array of intensity "zeros", surrounded by quasi-isotropic intensity maxima. This is illustrated in Figure 2.6B where we plot the spatial variations of the optical intensity along two directions in the x-y plane (blue and green lines in Figure 2.6A). Clearly, the two intensity curves show the same spatial evolution up to more than 150 nm away from the position of the zero intensity. The intensity distribution of the three electric field components $|E_x|^2$, $|E_y|^2$ and $|E_z|^2$ are shown in Figure 2.6C. The values of $|E_x|^2$ and $|E_z|^2$ are much higher than $|E_y|^2$. The polarizations of different combinations of field components are shown in Figure 2.6D. Since the field components $|E_x|^2$ and $|E_z|^2$ are more significant than $|E_y|^2$, we are particularly interested in the polarization of $\vec{E_x} + \vec{E_z}$. Around the intensity minima, its evolution is linear along the x-axis and along directions ±60° to the x-axis and is elliptical elsewhere.

Since molecules are dipoles, the STED efficiency depends on the dot product of the dipole moment and the electric field as $|\vec{E}(t) \cdot \vec{d}(t)|^2$, where $\vec{d}$ is the dipole moment. $\vec{d}(t)$ is a function of time and is related to the rotational mobility of the molecules. We define τ_{rot} as the characteristic rotating time of the molecule. For timescales longer than τ_{rot},

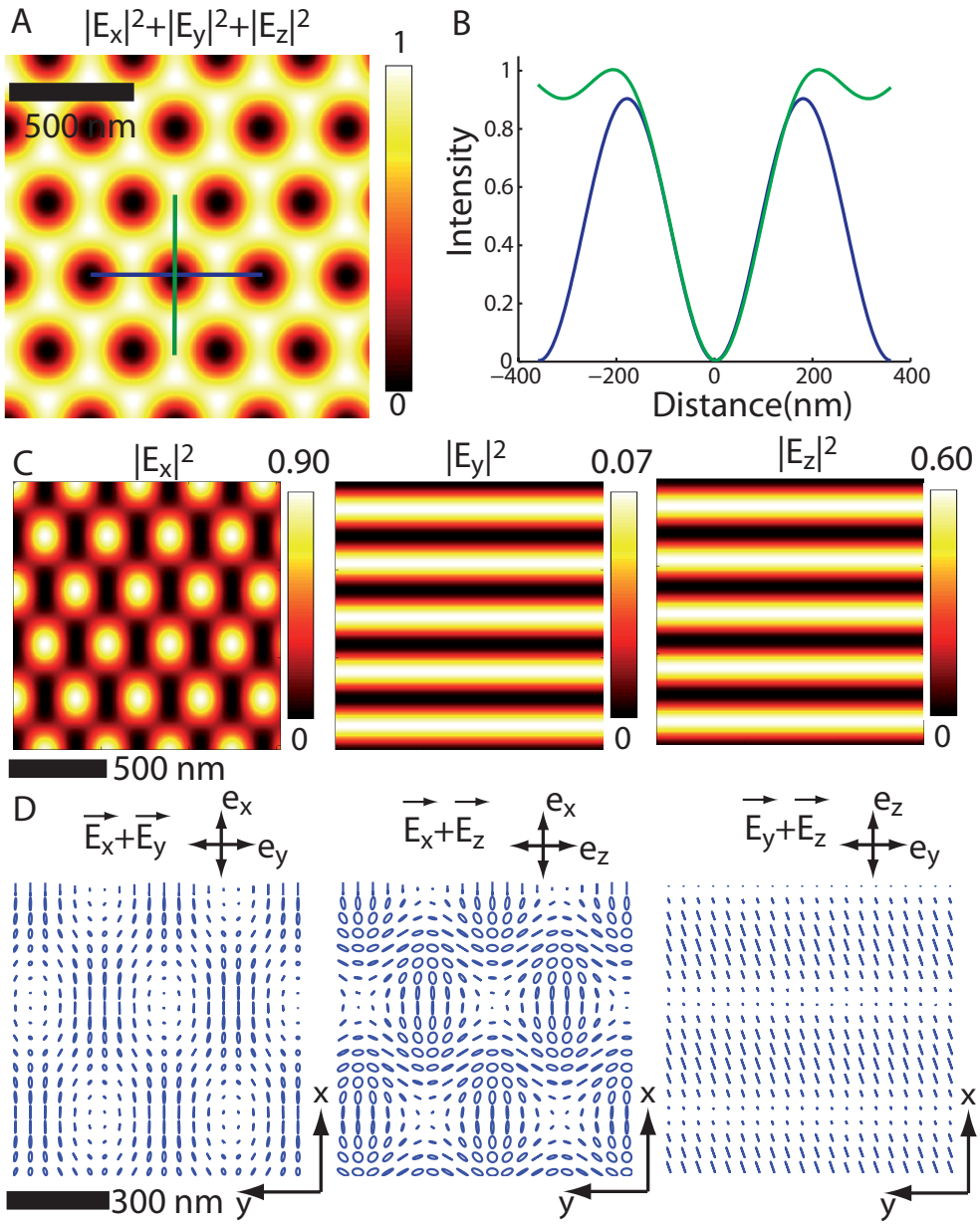

Figure 2.6: Optical lattice generated by three-beam interference for $\alpha = 30°$ and $\theta = 70°$. (A) shows the topography of intensity, by summing the three squared electric field components. The period is 390 nm. (B) shows the intensity plots along the blue and green lines in (A). (C) presents the intensity distributions of different electric field components. Intensities are normalized to the maximal intensity in (A). (D) shows the polarizations of different combinations of electric field components. Straight lines, ellipses and circles indicate respectively linear, elliptical and circular polarizations.

the molecule can be regarded as isotropic.

Figure 2.7 shows the timescales in pulsed-STED microscopy, where t_p (200 ps) is the STED pulse duration, T_p (12.5 ns) the laser repetition period and T_{int} ($\sim$ 1 ms) the integration time per camera frame. Three different regimes of rotational mobility should be considered :

(i) fast rotating molecules, where $\tau_{rot} \lessapprox t_p$.

(ii) fixed molecules, where $\tau_{rot} \gg T_{int}$.

(iii) slowly rotating molecules, where $t_p \ll \tau_{rot} < T_{int}$. Slowly rotating molecules can be regarded as fixed during each STED pulse.

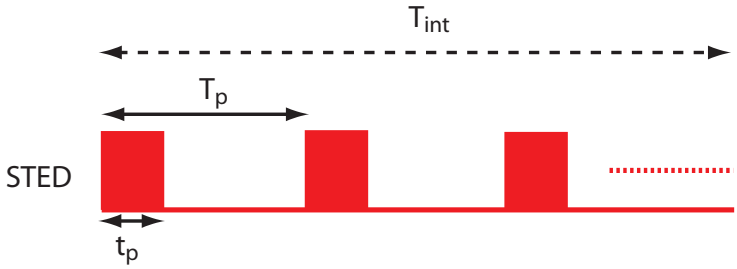

Figure 2.7: Timescales in pulsed-STED microscopy. t_p, T_p and T_{int} are respectively STED pulse duration, laser repetition period and integration time per camera frame. t_p = 200 ps, T_p = 12.5 ns and $T_{int} \sim$ 1 ms.

For a fast rotating molecule, the interaction between the dipoles and the electric field during the STED pulses can be viewed as an average effect between the electric field and a series of fixed molecules with different dipole moments. This interaction can be characterized by an effective intensity I_{fast}, i.e. the intensity "seen" by the molecule.

The dipole moment with an amplitude equalling unity of a fixed molecule can be described as:

$$\vec{d} = sin\theta cos\alpha\, \vec{e_x} + sin\theta sin\alpha\, \vec{e_y} + cos\theta\, \vec{e_z} \tag{2.13}$$

where θ and α are the azimuthal and polar angles in a spherical coordinate system, with $0 \leq \theta \leq 2\pi$, $0 \leq \alpha \leq \pi/2$.

The electric field writes as:

$$\vec{E}(t) = (E_x e^{i\phi_x}\,\vec{e_x} + E_y e^{i\phi_y}\,\vec{e_y} + E_z e^{i\phi_z}\,\vec{e_z})e^{iwt} \tag{2.14}$$

where ϕ_x, ϕ_y and ϕ_z are phases.

Then the effective intensity for a fast rotating molecule is given by:

$$\begin{aligned} I_{fast} &\approx \frac{1}{2\pi}\int_0^{2\pi}\int_0^{\pi/2} |\vec{E_t}\cdot\vec{d}(\alpha,\theta)|^2 sin\theta d\alpha d\theta \\ &= \frac{1}{2\pi}\int_0^{2\pi}\int_0^{\pi/2} |E_x e^{i\phi_x} sin\theta cos\alpha + E_y e^{i\phi_y} sin\theta sin\alpha + E_z e^{i\phi_z} cos\theta|^2 sin\theta d\alpha d\theta \\ &= \frac{1}{3}(|E_x|^2 + |E_y|^2 + |E_z|^2) = \frac{1}{3}I. \end{aligned} \tag{2.15}$$

According to Equation 2.15, the effective intensity is a third of the STED intensity regardless of the polarization of the electric field. The resolution of Lattice-STED microscopy for fast rotating molecules is thus directly related to the intensity distribution of the optical lattice. It will be isotropic, as the intensity gradient around the intensity minima of the optical lattice.

The effective intensity applied on a fixed dipole writes as:

$$\begin{aligned} I_{fixed} &= |\vec{E}(t)\cdot\vec{d}|^2 \\ &= |E_x e^{i\phi_x} sin\theta cos\alpha + E_y e^{i\phi_y} sin\theta sin\alpha + E_z e^{i\phi_z} cos\theta|^2. \end{aligned} \tag{2.16}$$

Equation 2.16 shows that for slowly rotating and fixed molecules, the effective intensity is related to the polarization of the electric field.

To simulate the effective excitation PSF (the volume in which fluorescence is not depleted) of a fast rotating molecule, we assume that the molecule is illuminated with a homogeneous wide-field excitation and the three-beam depletion optical lattice. Scanning the molecule across the focal plane of the objective and recording simultaneously its

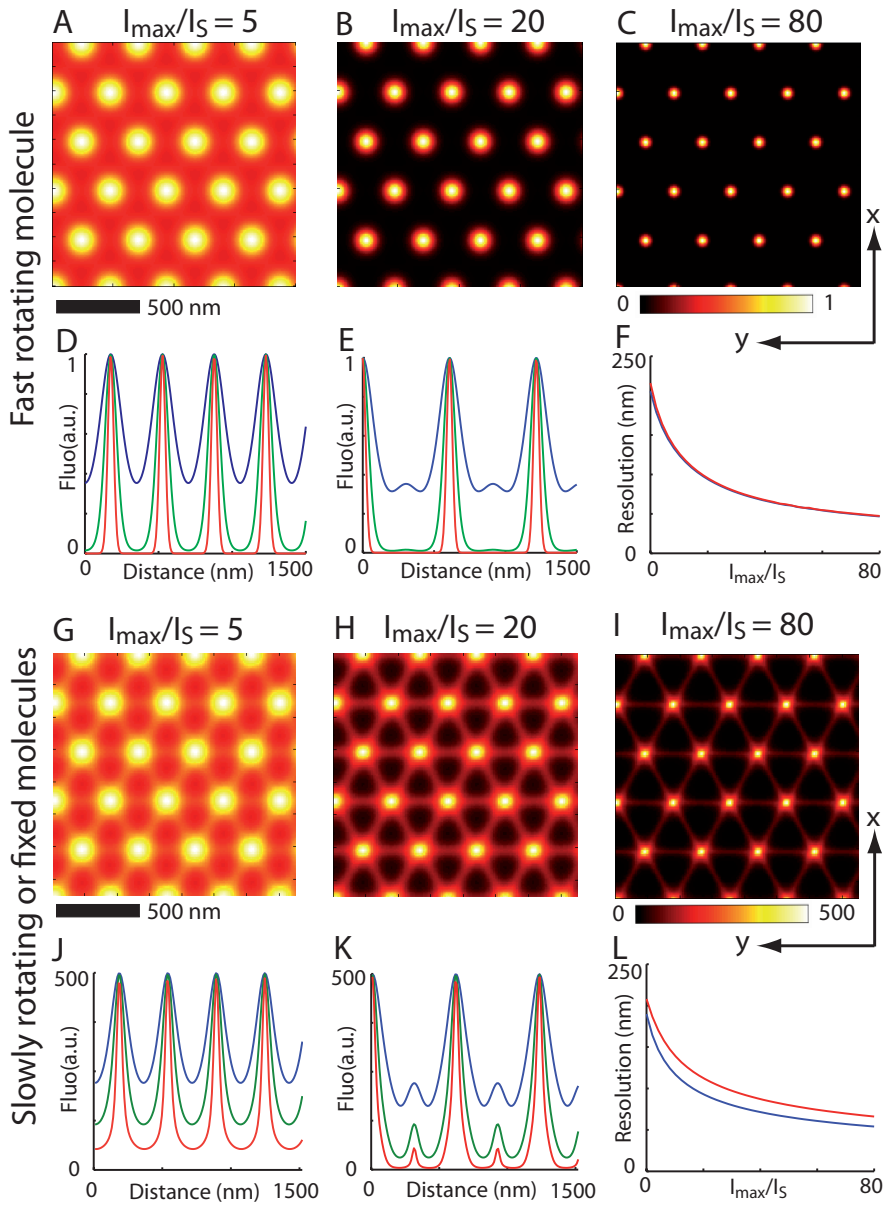

Figure 2.8: Simulated effective excitation PSF of Lattice-STED, with a homogeneous wide-field excitation and the three-beam depletion optical lattice. The PSFs are obtained by scanning a fluorescent object over the field of view and recording its fluorescence signal. The fluorescent object is either a fast rotating molecule (A-C) or a bead containing 500 randomly oriented molecules (G-I). The cross-sectional profiles of the fluorescence images along the y- (D,J) and x-axes (E,K) are also shown. Blue, green and red lines correspond respectively to I_{max}/I_S= 5, 20 and 80. (F) and (L) show the FWHMs of the PSFs along the y- (blue) and x-axes (red) as a function of I_{max}/I_S. The FWHMs are obtained by fitting the profiles of the PSFs with a Gaussian function. The FWHMs of the bead are averaged over 20 independent simulations.

fluorescence signal allows to reconstruct the effective excitation PSF. The fluorescence signal of the molecule can be described as (see Equation 1.8):

$$Fluo(x,y) = exp(-ln2\ \frac{I_{fast}(x,y)}{I_S}). \tag{2.17}$$

We show the effective excitation PSF of the molecule in Figure 2.8A-C for $I_{max} = 5, 20$ and $80 I_S$. The molecule is efficiently depleted at higher STED intensities where its fluorescence drops to zero. As predicted, the resolution of a fast rotating molecule is indeed isotropic. This is further confirmed by the comparison between the FWHMs of the effective excitation PSFs along the y- (blue curve) and x-axes (red curve), shown in Figure 2.6F.

To numerically evaluate the depletion effect of the three-beam optical lattice on slowly rotating or fixed molecules, we consider a fluorescent bead containing 500 randomly oriented (in three-dimensional space) molecules with fixed dipole moments. Similarly, we scan the bead over a homogeneous wide-field excitation and the three-beam depletion optical lattice while recording simultaneously its fluorescence signal to reconstruct the effective excitation PSF. The fluorescence signal of the bead is given by:

$$Fluo(x,y) = \sum_{i=1}^{500} exp(-\frac{ln2\ I_{fixed,i}(x,y)}{I_S}) \tag{2.18}$$

where $I_{fixed,i}$ is related to the dipole moment of the molecule and the spatial distributions of polarization and amplitude of the STED field. Figure 2.8G, H and I show respectively the effective excitation PSF of the bead for I_{max}/I_S=4, 20 and 80. The cross-sectional profiles along the y- and x-axes of the effective excitation PSF are shown respectively in Figure 2.8J and K. Since the depletion of fixed molecules depends strongly on the polarization of the field, all molecules are efficiently depleted where the polarization is elliptical, whereas molecules oriented perpendicular to the field of linear polarization are not depleted. Therefore cross-sectional profiles along the y-axis does not decrease

to zero even at high STED intensities. The FWHMs of the PSFs along the y- and x-axes (Figure 2.8L) show that the resolution exhibits slightly anisotropy, with relative differences between the FWHMs along the two directions being about 9 % - 22 % for I_{max} between 0 and $80I_S$. At $I_{max} = 80I_S$, the resolution along the y- (or x-) axis of a fluorescent bead is about 1.15 (or 1.38) times of the resolution of a fast rotating molecule.

2.2.2 Four-beam interference optical lattices

A key point for faster Lattice-STED imaging is to generate lattices with the smallest possible unit cell. For this purpose, one can increase the incidence angle θ of the interfering beams in the three-beam configuration, but the back aperture of the objective sets a limit. Alternatively, one can use a four-beam interference configuration where a smaller unit cell can be obtained with the same angle θ. Although the topography of electrical field of a two-dimensional optical lattice generated by four-beam interference varies with the relative phases between the beams, we will show that the topography of intensity of the four-beam optical lattice could be independent to the relative phases under certain conditions. Indeed, if the four beams are composed by two orthogonally polarized pairs of beams, each pair of beams will generate a one-dimensional interference pattern independently from the other pair of beams. The intensity distribution of the final optical lattice is just the sum of the two one-dimensional interference patterns. A square optical lattice can be obtained with a periodicity $p = \lambda/(2n\ sin\theta)$.

Figure 2.9 shows the geometrical configuration of the four beams. One pair of beams is polarized along the x-axis and is propagating in the y-z plane; the other pair is polarized along the y-axis and is propagating in the x-z plane. Therefore all the beams transmitted by the objective maintain their initial polarization (s-polarization).

Writing the electric field of each beam as $\vec{E_j} = \vec{e_j}\mathcal{E}e^{i(\vec{k_j}\cdot\vec{r}+\phi_j)}$, $j = 1-4$, with $\vec{e_1}, \vec{e_2} = \vec{e_x}$ and $\vec{e_3}, \vec{e_4} = \vec{e_y}$, we derive the electric field and the intensity distribution of

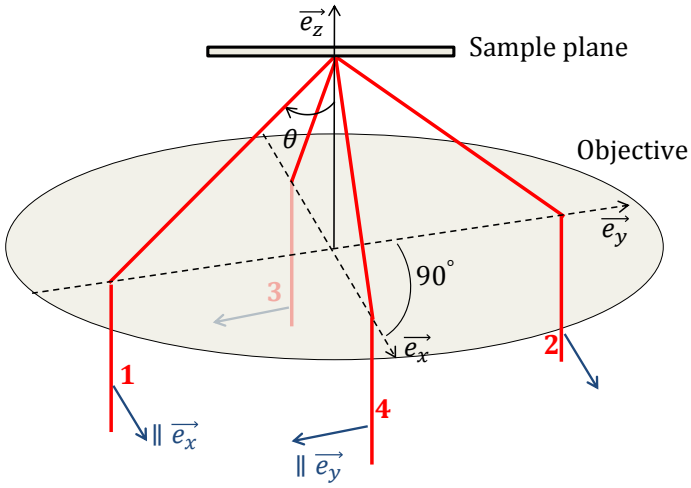

Figure 2.9: Geometric configuration of the four beams arriving on the sample plane. Beams 1 and 2 have polarization along the x-axis, and beams 3 and 4 have polarization along the y-axis. The four beams intersect the back focal plane of the objective at the vertices of a centered square.

the four-beam optical lattice at the focal plane:

$$\vec{E}_{tot} = 2\mathcal{E}\vec{e_x}e^{i(\frac{\phi_1+\phi_2}{2})}cos(\frac{2n\pi}{\lambda}xsin\theta + \frac{\phi_1-\phi_2}{2}) + 2\mathcal{E}\vec{e_y}e^{i(\frac{\phi_3+\phi_4}{2})}cos(\frac{2n\pi}{\lambda}ysin\theta + \frac{\phi_3-\phi_4}{2}), \tag{2.19}$$

$$I_{tot} = \frac{I_{max}}{2}(2 + cos(\frac{4n\pi}{\lambda}xsin\theta + \phi_1 - \phi_2) + cos(\frac{4n\pi}{\lambda}ysin\theta + \phi_3 - \phi_4) \tag{2.20}$$

where $I_{max} = 4\mathcal{E}^2$.

The topography of intensity of the four-beam optical lattice is shown in Figure 2.10A, as well as those of the field components $|E_x|^2$ and $|E_y|^2$ (Figure 2.10C). The optical lattice displays a rectangular array of intensity "zeros" surrounded by intensity maxima. The period is 290 nm, for $\theta = 60°$ and $\lambda = 760$ nm. Figure 2.10B shows the intensity plots along the y-axis (green) and the diagonal direction (blue). The maximal intensity

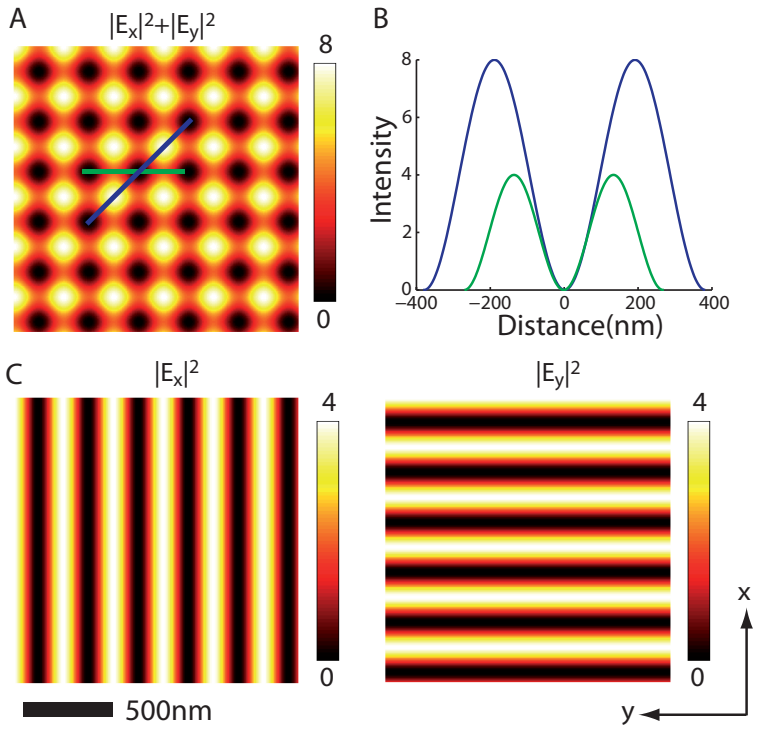

Figure 2.10: Optical lattice generated by the four-beam interference. (A) is the topography of intensity, with contributions of both field components $|E_x|^2$ and $|E_y|^2$. (B) shows the intensity plots along the blue and green lines in A. (C) presents the intensity distribution for different field components. Intensities in the unit of $\mathcal{E}^2$.

along the diagonal direction is two times that along the y-axis, nevertheless the intensity gradients around the intensity "zeros" are about the same. Therefore the resolution is still isotropic for faster rotating molecules.

The topography of electric field depends on the relative phases, as is illustrated in Figure 2.11. If the relative phase difference between the four beams satisfy the relation $\Delta\Phi = \frac{\phi_1+\phi_2-\phi_3-\phi_4}{2} = 0$, the polarization of the field is linear everywhere. If $\Delta\Phi = \pi/2$, the polarization is only linear along the x- and y- axes, but is circular along the directions $\pm 45°$ to the x- and y- axes and is elliptical elsewhere. For other relative phase values, the polarization is elliptical everywhere except along the x- and y-axes where it is linear. Therefore the effective excitation PSF of slowly rotating or fixed dipoles depends on $\Delta\Phi$.

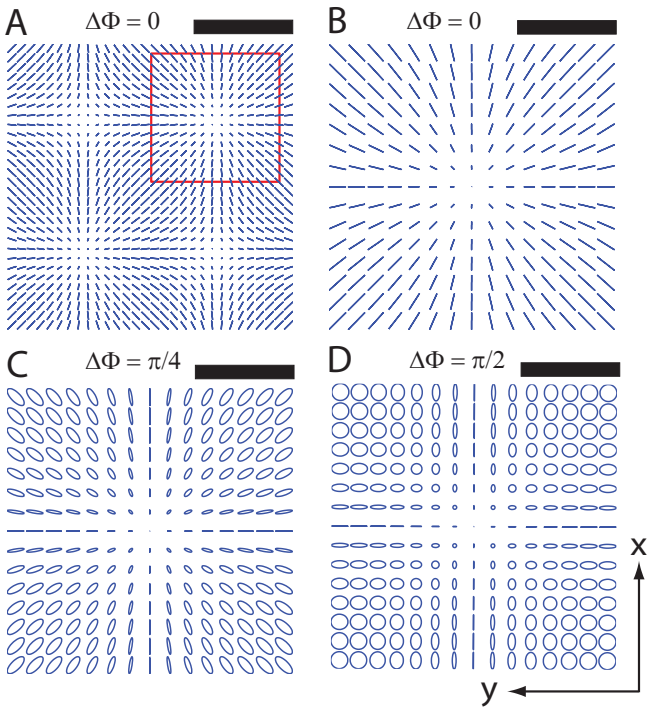

Figure 2.11: Polarizations of the electric field of the four-beam optical lattice, shown for different values of relative phases $\Delta\Phi$ ($= \frac{\phi_1+\phi_2-\phi_3-\phi_4}{2}$). (B) is the magnified view of which is in the red square from (A). Straight lines, circles and ellipses indicate respectively linear, circular and elliptical polarizations. Scale bar: 200 nm (A) and 100 nm (B-D).

We simulate the effective excitation PSFs of both a fast rotating molecule and a fluorescent bead containing 500 randomly oriented (in three-dimensional space) fixed molecules, shown in Figure 2.12.

Since the depletion of a fast rotating molecule depends only on the STED intensity, its fluorescence signal can be reduced to zero in all directions around the intensity minima, as shown by the fluorescence intensity profiles along the y-axis and the diagonal direction (45° to the y-axis). The resolution is isotropic for $I_{max} > 4I_S$.

The effective excitation PSF of the bead is shown in three cases for $\Delta\Phi = 0, \pi/4$ and $\pi/2$. For $\Delta\Phi = 0$, since the polarization of the field is linear everywhere, molecules are not depleted where their dipole moments are perpendicular to the local field. Therefore

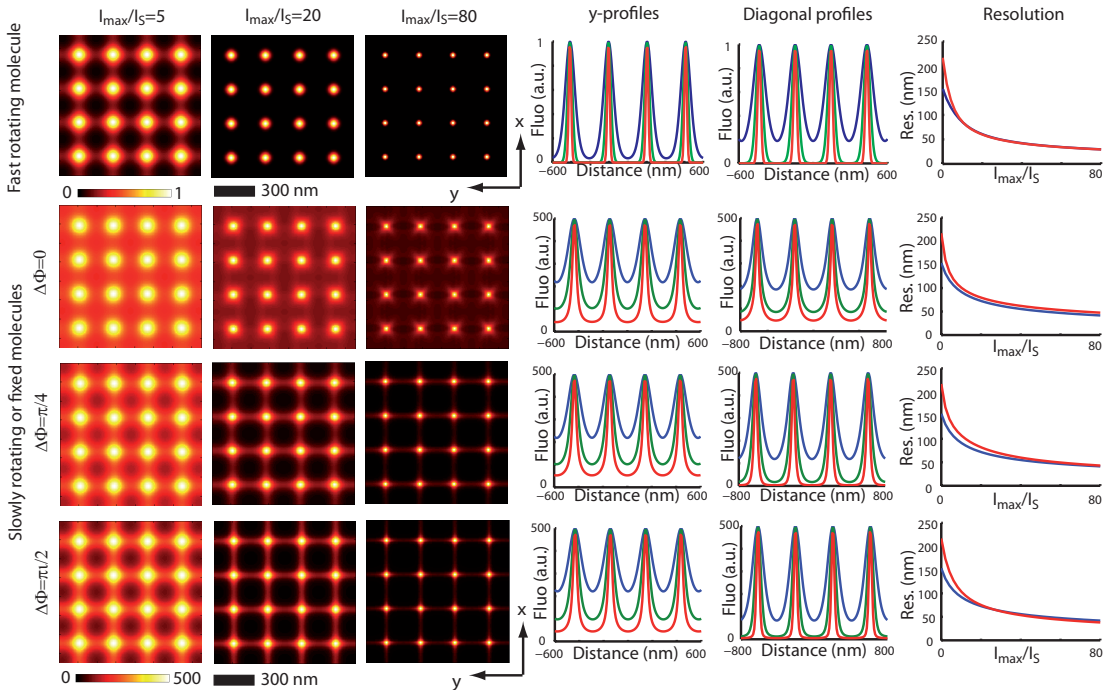

Figure 2.12: Simulated effective excitation PSF of four-beam Lattice-STED, obtained with a homogeneous wide-field excitation and the depletion optical lattice. Images are simulated for a fast rotating molecule and for a bead containing 500 randomly oriented fixed molecules (in three-dimensional space). The fluorescence signal is in units of the maximal emission rate of one molecule. Effective excitation PSFs are shown for different values of $\Delta\Phi$ and I_{max}/I_S. The profiles of the PSFs along the y-axis and the diagonal directions (45° to the y-axis) are also given, where the blue, green and red curves correspond respectively to $I_{max}/I_S = 5$, 20 and 80. The FWHMs of the PSFs for both the fast rotating molecule and the bead are shown as a function of I_{max}/I_S, where the blue and red curves correspond respectively to the resolutions along the y-axis and the diagonal direction. The FWHMs are obtained by fitting the profiles of the PSFs with a Gaussian function. The FWHMs of the bead are averaged over 20 independent simulations. Color bar and scale bar apply to all figures.

the fluorescence signal of the bead is not depleted down to zero even at higher STED intensities. The resolution along the y-axis (blue curve) is about 87% - 90% of that along the diagonal direction (red curve) at $I_{max} > 10I_S$. For $\Delta\Phi = \pi/2$, the molecules are efficiently depleted where the polarization of the field is close to circular. Therefore the fluorescence signal of the bead can be depleted to near zero at higher STED intensities (see the fluorescence intensity profiles along the diagonal direction). However, the fluorescence signal of the bead is not reduced to zero along the y- (and x-) axis, where the polarization of the field is linear. The effective excitation PSF of the bead thus exhibits cross-like structures. The resolution along the y-axis (blue curve) is slightly larger (less than 10%) than that along the diagonal direction (red curve), at $I_{max} > 10I_S$. Moreover, the resolution of a fluorescent bead is about 1.5 times of that of a fast rotating molecule at $I_{max} = 80I_S$.

2.2.3 Resolution comparison between multi-doughnut STED and Lattice-STED

Besides the advantages of being able to easily generate a large array of intensity minima, the optical lattices also require less depletion power than a multi-doughnut STED setup, for the same number of intensity minima and the same target resolution. This is due to the fact that with interference one can achieve higher depletion intensities and better-confined zero-intensity regions than those with isolated doughnuts.

We theoretically compare the resolution obtained in Lattice-STED and in multi-doughnut STED microscopies. For simplicity, we consider the case of a fast rotating molecule. Since the effective intensity applied on the molecule is a third of the STED intensity regardless of the polarization, we will neglect the orientation effect of the molecule in the following discussions.

An analytical expression of the doughnut STED resolution Δr_d (FWHM) has been

derived in Chapter 1:

$$\Delta r_d = d_c \Big/ \sqrt{1 + \frac{\pi^2 d_c^2}{4d^2} \frac{I_d}{I_S}} \tag{2.21}$$

where d_c is the confocal resolution, d is the diameter of the doughnut beam and I_d the maximal intensity of the doughnut beam.

We use the same theoretical approach to establish an analytical expression for Lattice-STED resolution. Here, we focus on the four beam optical lattice. The intensity distribution of the optical lattice $I(x, y)$ at the sample plane writes as:

$$I(x,y) = I_l \Big[sin^2(\frac{2\pi n x sin\theta}{\lambda}) + sin^2(\frac{2\pi n y sin\theta}{\lambda}) \Big]. \tag{2.22}$$

The resolution along the x-axis (for y=0) is given by:

$$\Delta r_l \approx d_c \Big/ \sqrt{1 + \frac{\pi^2 d_c^2}{4p^2} \frac{I_l}{I_S}} \tag{2.23}$$

where $p = \lambda/(2n\ sin\theta)$ is the period. Compared to Equation 2.21, d and I_d are simply replaced respectively by p and I_l.

To compare the performance of Lattice-STED to multi-doughnut STED, we calculate the power needed to achieve a given resolution for a same number N of intensity "zeros" for the two experimental configurations. For this purpose, we first express the intensity maxima I_d and I_l as a function of the total STED powers P_d and P_l used for each configuration. In the doughnut STED, using a Laguerre-Gauss mode intensity profile:

$$I(r) = I_d \frac{4er^2}{d^2} exp(-\frac{4r^2}{d^2}), \tag{2.24}$$

one obtains

$$I_d = \frac{4}{e\pi d^2 N} P_d. \tag{2.25}$$

While in the case of the four-beam Lattice-STED, one has:

$$I_l = \frac{cos\theta}{Np^2} P_l. \tag{2.26}$$

The factor $cos\theta$ takes into account of the oblique incidence of the four beams on the interference plane.

Equalising Equation 2.21 and Equation 2.23, we obtain:

$$\frac{P_d}{P_l} = \frac{e\pi}{4}\left(\frac{d}{p}\right)^4 cos\theta. \tag{2.27}$$

It clearly shows that Lattice-STED is more efficient than multi-doughnut STED. For θ= 60°, p = 290 nm and d = 450 nm, multi-doughnut STED microscopy requires 6.2 times more depletion power than Lattice-STED microscopy.

2.3 STED with a single doughnut depletion beam

We have realized in the first place a home-built pulsed-STED microscope with a single doughnut depletion beam, which allows us to better understand the mechanism of STED microscopy and to prepare the experimental requirements for STED parallelization such as the laser synchronization.

2.3.1 Experimental setup

Pulsed laser sources and their synchronization

The doughnut-STED microscope is based on two pulsed laser sources, as shown in Figure 2.13A. A pump laser (Verdi V18, Coherent) provides 18 W laser power at 532 nm which is separated by a non polarizing beamsplitter (NPBS) to pump two Ti-sapphire oscillators: the oscillator 1 (passively mode-locked picosecond laser, Mira 900 Coherent) and the oscillator 2 (actively mode-locked laser, Tsunami, Spectra Physics). The oscillator 1

pumps a frequency doubled optical parametric oscillator (Mira-OPO, Coherent), which delivers the excitation beam at 560 nm. The pulses are of 2 ps duration and have a repetition rate of 76 MHz and an average power of 200 mW. The oscillator 2 delivers Fourier-transform-limited STED pulses of $\sim$ 200 ps at 760 nm with 1.5 W average output power. This pulse duration is chosen such that the pulse duration is much longer than the relaxation time of the vibrational states of the fluorophores and much shorter than the lifetime of the excited state.

The excitation and STED beams are synchronized by locking the cavity length of the oscillator 2 to the repetition rate of the oscillator 1 (see Figure 2.13B). Small reflections of the output beams of the two oscillators are sent to two fast photodiodes. An electronic controller compares the repetition rates of the two oscillators and translates a motorized mirror in the cavity of the oscillator 2 to match its length to that of the oscillator 1. The controller also drives the RF frequency of the acousto-optic modulator (AOM) used for active mode-locking of the oscillator 2. By tuning the phase of the RF field, we can adjust the delay between the STED and excitation pulses.

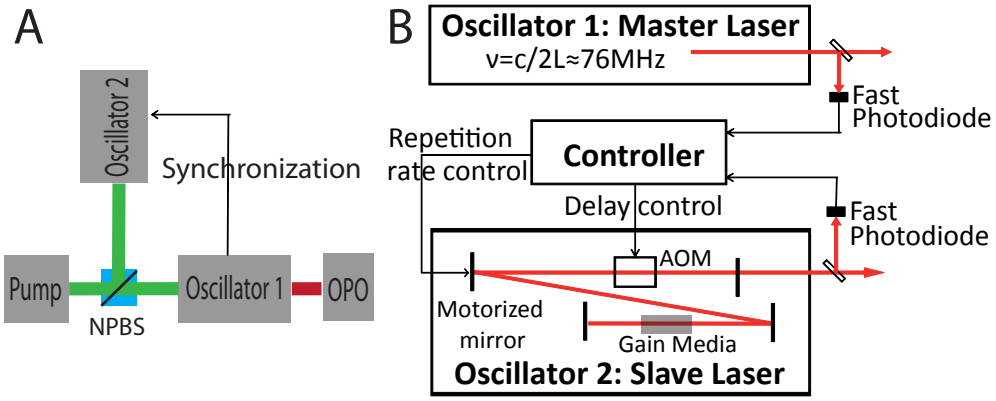

Figure 2.13: Laser synchronisation. Oscillator 1 is coupled with an optical parametric oscillator and delivers a train of pulses at a fixed repetition rate (76 MHz). The repetition rate of oscillator 2 is adjusted by changing its cavity length with a motorized mirror to match that of the oscillator 1. The pulse delay between the two oscillators are adjusted with a delay applied on the RF field of the acoustic-optic modulator (AOM) .

Optical setup

We show the optical setup of the doughnut-STED microscope in Figure 2.14. The oscillator 1 and OPO deliver the excitation beam. The excitation power is adjusted by a zero-order half-wave plate together with a polarizing beamsplitter. An AOM (AOM1, MT110-A1-VIS, AA OPTO-ELECTRONIC) performs on/off switching of the beam in order to control the illumination time during image acquisition. A collimated beam with a Gaussian profile is obtained after coupled to a single-mode polarization-maintaining fiber. The polarization of the beam is transformed from linear to circular using a quarter-wave plate.

The STED beam delivered by the oscillator 2 is sent through a Faraday isolator in order to avoid any optical feedback, which can alter the pulsed operation of the oscillator. A zero-order half-wave plate placed before the Faraday isolator and an AOM (AOM2, MT110-A1-VIS, AA OPTO-ELECTRONIC) are used to respectively control the STED power and to perform on/off switching of the STED beam. An excitation filter (zet750/20x, Chroma) suppresses spontaneous light emitted from the Ti-Sapphire crystal of the oscillator to reduce the background signal. The STED beam is also coupled into a single-mode polarisation-maintaining fiber and collimated by a triplet fiber coupler. The beam is then expanded and sent on a spatial light modulator (SLM, LCOS-SLM X10468-02, Hamamastu) which imprints a spatial phase distribution on the beam and turns it into a doughnut beam (see Section 2.4.2 for more details).

Two dichroic mirrors (DM1 605 DCXR and DM2 T700DCSPXXR-UV, Chroma) are used to combine the excitation and STED beams, and to separate the fluorescence emitted from the sample. The two beams are focused by an oil-immersion objective (Apo-TIRF X60 NA=1.49, Nikon) to a diffraction-limited Airy disc (excitation) and a doughnut spot (STED), which spatially overlap at the same sample plane. The STED beam reflected by the sample can be sent to a camera (DCC-1545M-GL, Thorlabs), in order to characterize its intensity distribution. A piezoelectric stage (P-733.3DD,

PI) is used for sample scanning. The fluorescence is collected by the objective, filtered from the excitation and STED photons using two emission filters (Bandpass 641/75 and FF01-720/SP, Semrock) and sent to an avalanche photodiode (single photon counting module).

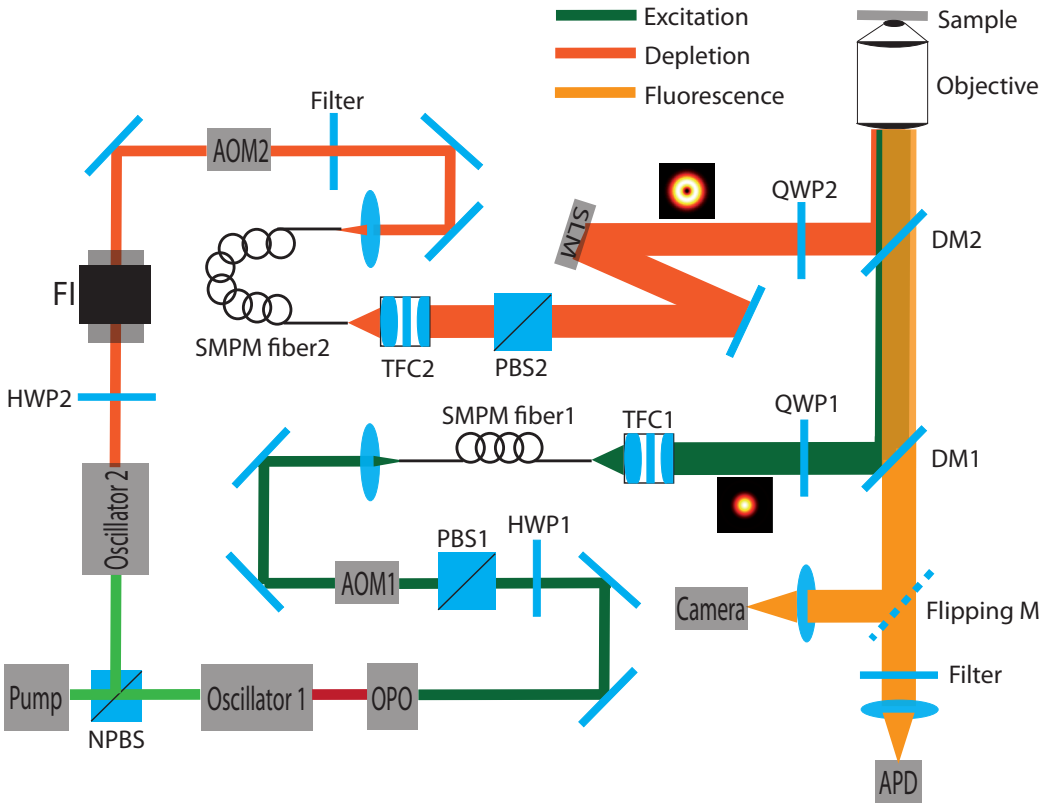

Figure 2.14: Optical setup of the doughnut-STED microscope. The doughnut shape of the STED beam is obtained with a helix phase (see Figure 2.24) applied on the spatial light modulator (SLM). The excitation and STED beams are combined with two dichroic mirrors (DM)and focused on the sample plane with an oil-immersion objective (NA = 1.49). An avalanche photodiode (APD) is conjugated with the sample plane and records the fluorescence signal. A control camera is used to monitor the beam profile. Abbreviations: NPBS: Non-Polarising cube BeamSplitter; HWP: Half-Wave Plate; PBS: Polarizing Beamsplitter; AOM: Acousto-Optical Modulator; SMPM fiber: Single-Mode Polarisation-Maintaining fiber; TCF: Triplet Fiber Collimator; QWP: Quarter-Wave Plate; FI: Faraday Isolator; Flipping M: Flipping Mirror.

2.3.2 Characterizations of the pulse sequences of the lasers and of the spatial profile of the STED beam

Pulse sequences

The time delay Δt (see Figure 2.15) between the excitation and STED pulses affects the fluorescence depletion efficiency in pulsed-STED microscopy. An optimal delay between the excitation and STED pulses needs to be found to reach the maximal depletion efficiency. To look for this delay experimentally, we illuminate a 20 nm fluorescent crimson bead with the excitation and STED beams, both Gaussian-shaped. The absorption and emission spectra of the bead are shown in Figure 2.16. The green and red lines indicate respectively the excitation and STED wavelengths; the yellow zone shows the fluorescence collection band. A STED wavelength closer to the emission peak would be more efficient. However, in this case, due to overlap of the emission and excitation spectra, the probability that the STED beam excites the beads by anti-Stokes process is non-negligible. Therefore a STED beam at 760 nm minimizes the anti-Stokes excitation and maximizes the STED efficiency.

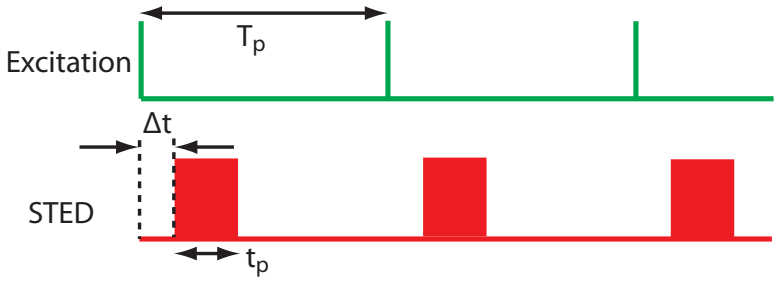

Figure 2.15: Pulses sequences of the excitation and STED beams. T_p is the laser repetition period, t_p the STED pulse duration and Δt the delay.

We first numerically evaluate the depletion efficiency as a function of Δt. For this purpose, we consider that the excitation pulses are extremely short. For $-t_p < \Delta t < 0$, the STED pulses arrives before the excitation pulses, the population of the electronic

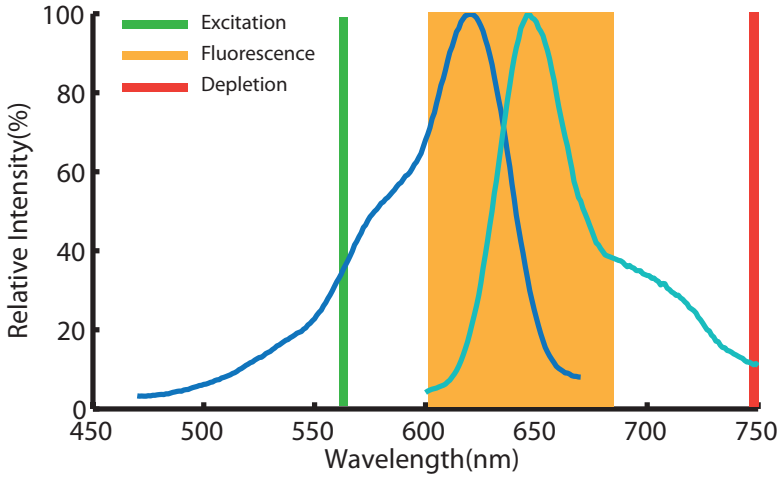

Figure 2.16: Absorption and emission spectra of a crimson fluorescent bead. Green line: excitation wavelength at 560 nm; red line: depletion wavelength at 760 nm; yellow zone: fluorescence detection zone (600 nm - 680 nm) corresponding to the transmission windows of the emission and dichroic filters.

excited state P_{S1} writes (see Equation 1.7):

$$P_{S1}(t) = exp(-\Gamma t)\, exp(-\frac{\sigma\lambda}{hc} I_p\, min(t, t_p + \Delta t)) \tag{2.28}$$

where Γ is the spontaneous emission rate of the bead, λ the wavelength of the STED beam, σ the corresponding cross section, h the Planck constant, c the speed of light in vacuum and I_p the peak STED intensity.

The term $t_p + \Delta t$ indicates that only a part of the STED pulses contributes to fluorescence depletion.

For $0 < \Delta t < T_p - t_p$, the STED pulses arrives after the excitation pulses and P_{S1} reads:

$$P_{S1}(t) = exp(-\Gamma t)\, exp(-\frac{\sigma\lambda}{hc} I_p\, min(max(t - \Delta t, 0), t_p). \tag{2.29}$$

Before the arrival of STED pulses, P_{S1} decreases slowly due to spontaneous emissions, whereas P_{S1} follows a rapid reduction with the arrival of STED pulse. The effect of delays on P_{S1} is illustrated in Figure 2.17A, which shows the simulated temporal evolutions of

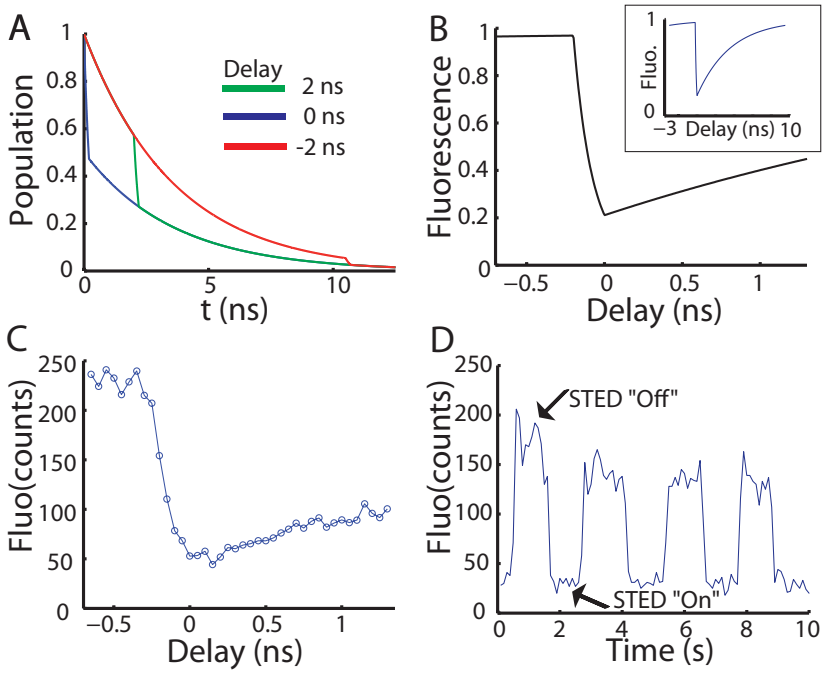

Figure 2.17: Effects of the delay between the excitation and STED pulses. (A) Temporal evolutions of the population level of S_1 of a molecule after an excitation pulse at t = 0 for delays of the STED beam of -2 ns, 0 ns and 2 ns. (B) Fluorescence of the molecule as a function of the delay. For t > 0, one recovers the lifetime of the excited state (3.4 ns). Data are calculated for $\tau = 3.4$ ns, $I_{STED} = 2.3\ I_S$, $t_p = 200$ ps and $T_p = 12.5$ ns. Population and fluorescence are normalized to 1. (C) Experimental data of fluorescence signal emitted by a fluorescent bead as a function of delay. Average intensities: I_{exc}=100 kW/cm^2 and $I_{STED} = 50$ MW/cm^2. (D) Temporal evolution of the fluorescence of a single fluorescent bead while applying a periodic on/off STED beam together with a constant excitation beam. Average intensities: $I_{exc} = 100$ kW/cm^2, $I_{STED} = 300$ MW/cm^2, integration time per point 100 ms.

P_{S1} for three different delays.

The probability of the emission of one photon during one excitation cycle is related to P_{S1} as:

$$P_{em}(\Delta t) = \eta_{rad}\Gamma \int_0^T P_{S1}(t, \Delta t)dt. \tag{2.30}$$

where η_{rad} is the quantum yield.

Figure 2.17B shows P_{S1} as a function of the delay. At $\Delta t = 0$, the fluorescence de-

pletion is most efficient, whereas the fluorescence increase with the delay since molecules can emit fluorescence before being depleted by the STED light.

Figure 2.17C shows the fluorescence signal of a single bead recorded as a function of the delay, which is similar to the simulated data (Figure 2.17B). At Δt=0, the depletion and excitation pulses arrive simultaneously on the sample and the depletion efficiency is maximal. No depletion occurs when the entire depletion pulse arrives before the excitation pulse. For increasing delays, the depletion efficiency decreases and the fluorescence signal increases with a time constant of the order of the excited state lifetime of the molecules.

Figure 2.17D presents the temporal evolution of the fluorescence of an excited bead submitted to successive on/off time periods for $\Delta t = 0$. The fluorescence signal, which is approaching 2000 c/s without depletion beam, drops to the background level 200 c/s when the depletion beam is switched "on" with an average depletion intensity 300 MW/cm^2.

Spatial profile of the STED beam

Careful characterization of the intensity distribution of the STED beam in the focal plane of the objective is very important for STED imaging. Achieving zero intensity at the central region of the doughnut beam is a crucial point since any residual light will lead to unwanted fluorescence depletion and a deterioration of the achievable resolution. The intensity distribution should also be isotropic around the doughnut center in order to achieve isotropic resolutions. To characterize the intensity distribution, one can use a camera image of the doughnut beam reflection at the sample plane. However, if a tightly focused beam is incident from the optically denser medium and is reflected at the interface, the plane-wave components of the focused beam with angles of incidence smaller than the critical angle have real reflection coefficients, whereas all the components with larger angles undergo total internal reflection and phase shifts. The reflection of

the beam is thus rather complex [170] and does not give access directly to the beam intensity distribution at the reflection plane.

Therefore, we choose to probe directly the intensity distribution of the doughnut beam at the sample plane by scanning a gold nanoparticle across the beam focus and simultaneously recording the scattered light with an avalanche photodetector (APD) conjugated with the sample plane. For this purpose, we spin-coat an aqueous solution containing nanoparticles of 60 nm diameter on a glass coverslip. We then deposit on the nanoparticles a drop of immersion oil having a refractive index (1.515) nearly matching that of the glass coverslip. This index matching minimizes the reflection of the doughnut beam at the coverslip surface which can blur the light scattered by the nanoparticle and even damage the APD. The signal delivered by the APD is proportional to the intensity of the field propagating in the backward direction of the objective which writes as [171]:

$$I_{det} = |E_r + E_s|^2 = |E_i|^2(r^2 + |s|^2 - 2r|s|cos\phi) \tag{2.31}$$

where E_i, E_r and E_s denote respectively the incident, reflected and backward scattered light fields. r is the field reflectivity at the glass-oil interface, s is proportional to the particle polarizability and ϕ is the phase shift between the two components (mainly determined by the Gouy phase shift). The term proportional to r^2 is simply the background intensity which originates from the reflection at the interface between the sample's surface and the immersion oil. The term proportional to $|s|^2$ is the pure scattering signal while the last term represents the interference between the reflected and scattered fields. In the case of good matching of refraction indices and large particles, r is much smaller than $|s|$, therefore the detected intensity I_{det} is dominated by the scattered light and is proportional to the incident light intensity $I_i(= |E_i|^2)$. Recording the detected signal while scanning a nanoparticle across the STED beam therefore allows us to reconstruct its intensity distribution. Figure 2.18 shows the intensity profile of the doughnut

beam prepared using a SLM. In the focal plane, the diameter of the doughnut beam is 500 nm. The signal at the center of the doughnut is at the background level, suggesting that the doughnut beam has a intensity minimum close to zero.

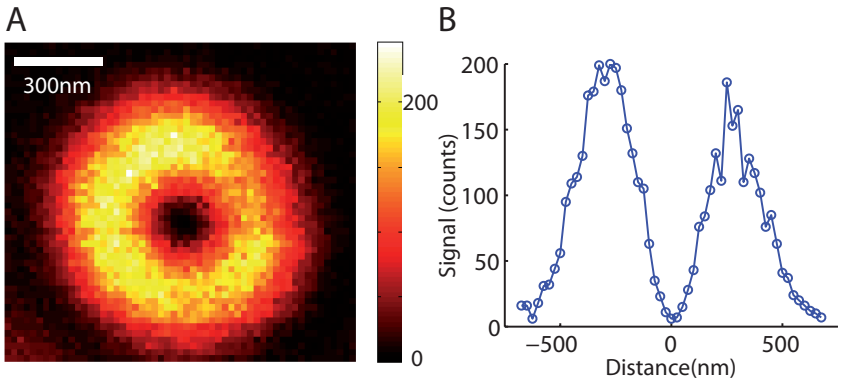

Figure 2.18: Intensity profile of the doughnut beam. (A) Two-dimensional intensity distribution of the STED beam in the sample (focal) plane. This measurement was obtained by scanning a 60 nm gold nanoparticle across the focused beam and recording the scattered light. Pixel dwell time 10 ms. (B) Cross-sectional intensity profile.

2.3.3 Experimental results

In this section we will present the results obtained with our home-built doughnut-STED microscope. Figure 2.19A shows a 2 μm * 2 μm confocal image of 20 nm fluorescent beads spin-coated on a glass coverslip recorded without STED beam. Figure 2.19B is the corresponding STED image recorded with an average STED intensity of 75 MW/cm^2 (average STED power 400 mW). The STED image clearly demonstrates resolutions beyond the diffraction limit. The images presented are raw images, without deconvolution. Figure 2.19C shows the confocal and STED profiles of an individual bead. The FWHM of the STED profile gives a resolution of about 40 nm, much smaller than that of the confocal profile ($\approx$ 230 nm, diffraction limited).

We then use our doughnut-STED microscope to image microtubules in fixed fibroblast-like COS cells. Microtubules are a component of the cytoskeleton, they can grow as long

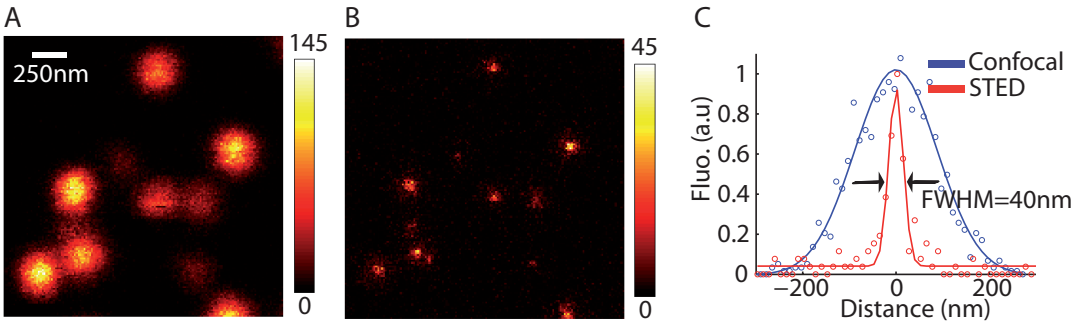

Figure 2.19: Confocal (A) and STED (B) images of 20 nm fluorescent beads recorded for I_{exc} = 100 kW/cm^2, I_{STED} = 75 MW/cm^2. (C) Confocal and STED profiles of a single bead. Pixel dwell time 1ms.

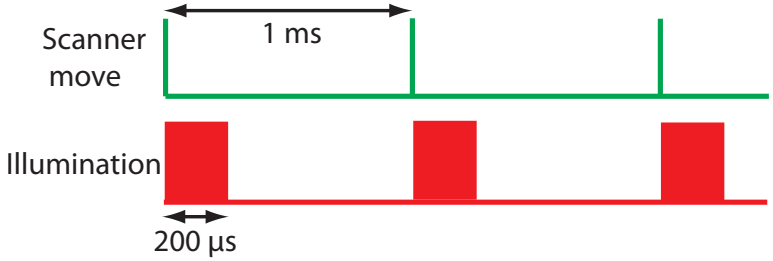

Figure 2.20: Illumination time for biological sample. The scanner moves the sample every 1 ms, whereas the illumination time is set by the AOM to 200 μs.

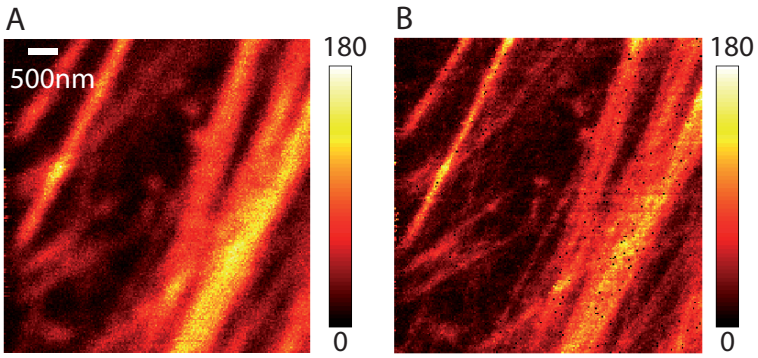

Figure 2.21: Confocal (A) and STED (B) images of microtubules labelled with ATTO 647N dye in COS cells. I_{exc} = 200 kW/cm^2, I_{STED} = 87 MW/cm^2. Illumination time per pixel 200 μs.

as 50 micrometres, with an average length of 25 μm. The outer diameter of a microtubule is about 24 nm while the inner diameter is about 12 nm. The microtubules were stained using a standard immunofluorescence protocol involving a primary antibody (anti beta-tubulin) and a secondary antibody labelled with fluorescent dyes (Atto647N).

When imaging nanoscale structures in biological samples, photobleaching of fluorescent dyes constitutes a serious problem. Illuminated with high STED intensities, fluorescent dyes can be driven into highly excited and reactive states which lead to efficient photolysis processes [172, 173]. Furthermore, since STED microscopy offers better resolution than confocal microscopy, its sampling is more dense. For a same imaging area, the dye molecules are exposed longer to laser beams and therefore are more prone to photobleaching.

To limit the photobleaching effect, one has to increase the scanning speed (reduce the pixel dwell time), so that the laser beams shine on the sample for shorter times during the data acquisition. However, the response time of the piezoelectric translation stage limits the scanning speed to ~ 1 ms per step. Therefore we used two AOMs in the setup to switch "on" and "off" the excitation and STED beams. For each scanning step, the light beams only shine on the sample for 200 μs (see Figure 2.20). Figure 2.21A and B are respectively the confocal and STED images of microtubules in fixed cells recorded with this procedure. The STED image shows clearly better resolution than the confocal image, giving access to more structural details.

In summary, we presented a STED microscope of a single doughnut depletion beam, based on two pulsed lasers. The lasers are synchronized and the delay between them is adjusted to maximize the STED efficiency. A STED experiment is performed with 20 nm fluorescent beads to evaluate the resolution. 40 nm resolution is achieved with an average STED intensity of 75 MW/cm^2. To reduce the photobleaching of the fluorescent dyes caused by the high STED intensity, we implemented two AOMs in the setup to control the time (per pixel acquisition) that the two beams shine on the sample. A STED

experiment is then performed on microtubules in COS cells and demonstrates better resolution than that limited by diffraction.

2.4 Experimental implementation of Lattice-STED

2.4.1 Optical setup

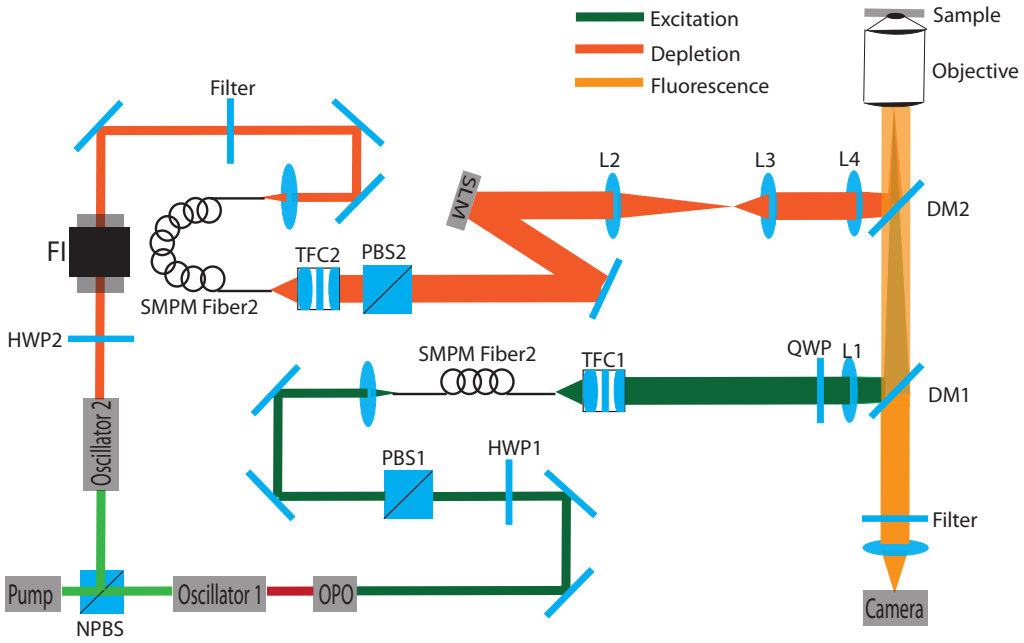

Figure 2.22: Optical setup of the Lattice-STED microscope. The oscillator 1 and the OPO together deliver the excitation beam which provides a wide-field illumination (10 μm * 10 μm). The oscillator 2 delivers the STED beam, divided by a SLM into multiple beams which interfere on the sample plane to generate optical lattices of the size of 3 μm * 3 μm. A sCMOS camera records the fluorescent signal. Abbreviations: NPBS: Non-Polarising cube BeamSplitter; HWP: Half-Wave Plate; PBS: Polarizing Beamsplitter; SMPM Fiber: Single-mode Polarisation-Maintaining Fiber; TFC: Triplet Fiber Collimator; QWP: Quarter-Wave Plate; L: lens; FI: Faraday Isolator; DM: Dichroic Mirror.

The optical setup of the Lattice-STED microscope is shown in Figure 2.22. Its laser system is the same as that of the doughnut-STED microscope: two synchronized pulsed lasers provide excitation (560 nm, 2 ps) and depletion (760 nm, 200 ps) beams. The

excitation beam is circularly polarized and provides a wide-field homogeneous illumination ($\sim$ 10 μm * 10 μm) at the sample plane than being focused to a diffraction-limited spot as in the doughnut-STED microscope. The STED beam is sent to a SLM which applies a phase mask on the STED beam to generate three (or four) lattice beams. The STED beam has linear polarization along the horizontal direction of the SLM surface. Therefore in the four-beam configuration, the polarization of the diffracted lattice beams are rotated by half-wave plates to obtain two orthogonally polarized pairs of beams. The SLM is conjugated with the sample plane via three lenses and the objective. Therefore the multiple beams, which originate from the SLM surface, recombine at the sample plane to generate the optical lattices ($\sim$ 3 μm * 3 μm). The optical lattices overlap the wide-field excitation. A sCMOS camera, also conjugated with the sample plane, is used for parallelized detection.

2.4.2 Generation of light patterns with a SLM

The SLM used in this study is a phase modulator, whose principle is illustrated in Figure 2.23. It contains an array of pixels (800 * 600). Each pixel is a square cell (20 μm by 20 μm) filled with liquid crystal. When an electric voltage is applied on a pixel, the liquid crystal molecules are tilted. As liquid crystal molecules show optical anisotropy, this tilt changes the refractive index of the medium (for incident polarization along the long display axis) which causes a modified optical path length within the liquid crystal cell. Therefore an electric voltage will correspond to a phase level. An incident light passes through two times the liquid crystal layer and is imprinted with a phase $e^{i\Phi(x,y)}$ depending on the voltage map applied by the pixel electrodes.

For example, to obtain a doughnut beam, we apply a vortex mask to the incident beam (see Figure 2.24A). The vortex beam has a singular phase point in its center where the phase value is not defined, hence the intensity in the beam center is zero at planes conjugated to the SLM surface.

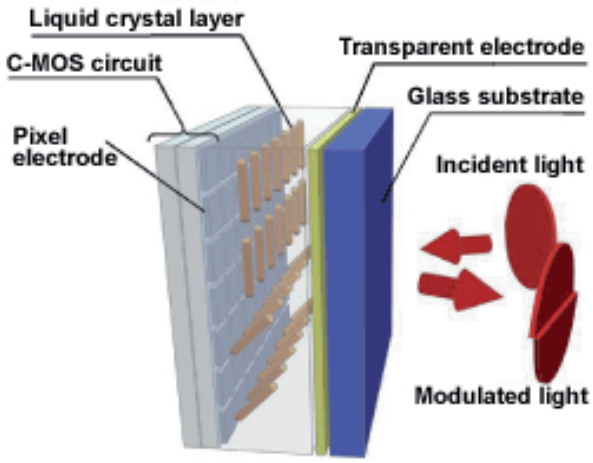

Figure 2.23: SLM Principle. An array of electrode applies on each pixel (filled with liquid crystal) a given voltage. This voltage locally modifies the orientations of the molecules and therefore modulates the refractive index of the medium. A phase pattern can be thus imprinted to the incident light when it passes through the liquid crystal layer.

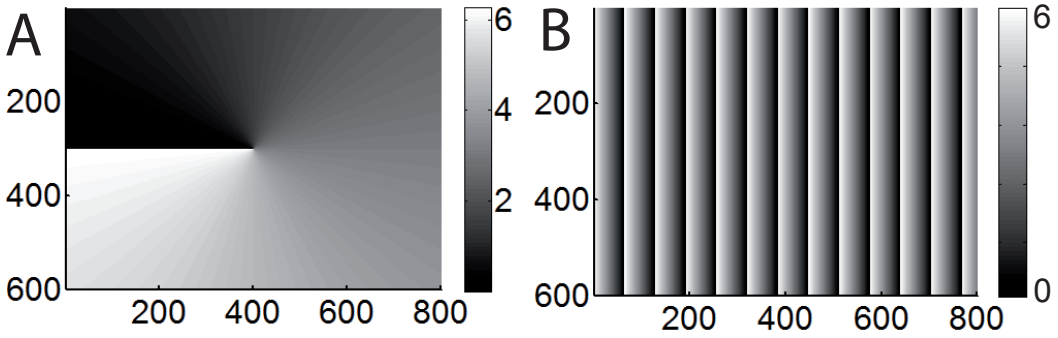

Figure 2.24: Images of the phase masks applied on the SLM in grey scale (255 levels coded over 8 bits). (A) Vortex mask with the phase varying from 0 to 2π azimuthally; (B) Blazed grating, phase value between 0 and 2π.

Only 93% of the SLM surface is filled with liquid crystal pixels. Therefore, part of the incident light reflected by the SLM is not modulated, which can induce residual intensity in the doughnut center. To eliminate this residual light, we apply together with the vortex mask a blazed grating (see Fig 2.24B). The grating diffracts 80% of the light to the first order. The zero order is subsequently blocked.

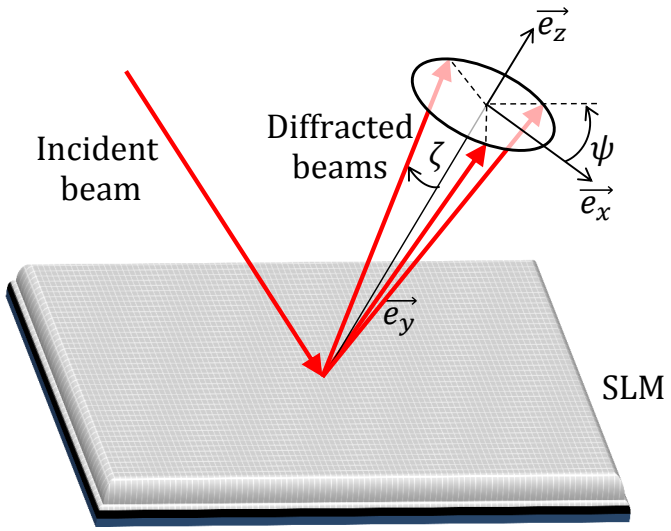

Figure 2.25: Geometrical configuration of the three beams diffracted from the surface of the SLM. The beams have linear polarizations along the x-axis and form a cone whose symmetry axis is the optical axis of the objective. The three beams intersect the base of the cone at the vertices of an equilateral triangle.

The SLM is also used to generate three beams (see Figure 2.25). The beams are diffracted from the SLM surface and form a cone whose symmetry axis is the optical axis of the microscope objective. The half aperture ζ of the cone is small ($\sim 3^{'}$), therefore all three beams approximately have the same linear polarisation along the x-axis. The intersections of the three beams with the base of the cone are the vertices of an equilateral triangle. ψ is the angle between the polarization and the projection of one of the wave vectors on the base.

We consider the electric field of the light at the SLM surface, the diffracted beams can be written as:

$$\vec{E_j} = E_j\vec{e_x} = \mathcal{E}\vec{e_x}e^{i\frac{2\pi}{\lambda}[cos(\psi_j)sin(\zeta)x+sin(\psi_j)sin(\zeta)y+\phi_j]} \tag{2.32}$$

where j=1,2 and 3, ϕ_j is the phase, ψ_1=ψ, ψ_2=$\psi + 120°$ and ψ_3=$\psi + 240°$.

In order to generate the three beams, the phase mask Φ_{SLM} imprinted by the SLM to the incident light is given by:

$$\Phi_{SLM}(x, y, \psi, \zeta) = Arg\left|\frac{E_1 + E_2 + E_3}{E_{in}}\right| \tag{2.33}$$

where E_{in} is the electric field of the incident beam. Figure 2.26A shows the phase mask, calculated for $\psi = 30°$, ζ=$2.8^{'}$ and ϕ_j=0. Changing the beam phase ϕ_j does not affect the topography of the generated optical lattice, but only translates the position of the intensity "zeros".

The phase mask not only generate the three beams but also other diffraction orders. These extra orders are blocked and only the three beams arrive at the sample plane to generate the optical lattice. We define the diffraction efficiency of the SLM with this

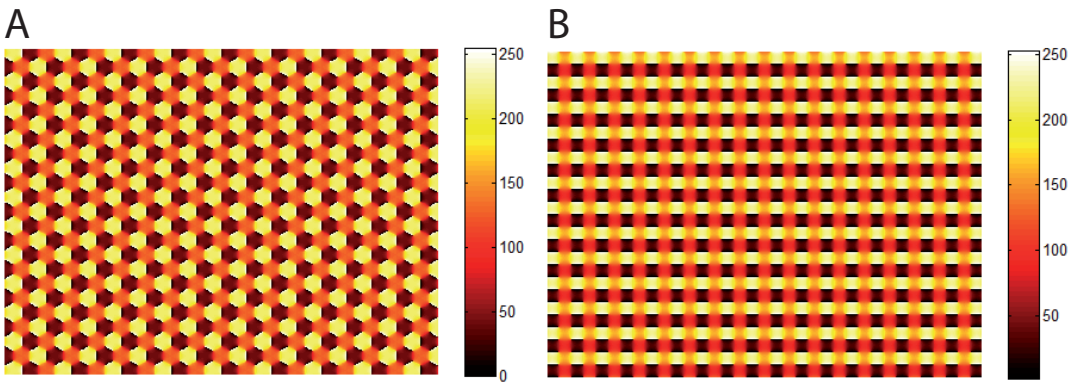

Figure 2.26: Images of phase masks applied on the SLM in grey scale (255 levels coded over 8 bits) for the three-beam (A) and four-beam (B) generations.

phase mask as the total power of the three beams divided by the power of incidence on the SLM, and found ≈ 40 %.

The four beams can be generated in the same way. Figure 2.26B shows the corresponding phase mask.

2.4.3 Experimental implementation of four-beam optical lattice

Due to its geometrical simplicity, we first discuss the experimental implementation of four-beam optical lattice.

2.4.3.1 Four-beam Lattice-STED

Figure 2.27A and B show the generation of the four-beam optical lattice with the SLM. The SLM surface is conjugated with the sample plane by three lenses and the objective, with respectively the focal lengths f_1, f_2, f_3 and f_0. The magnification of this optical system is $f_2 f_0/(f_1 f_3)$, which affects both the angle of incidence and the size of the optical lattice at the sample plane. The size of the optical lattice can be defined as the FWHM Δr_1 of the interfering beams at the focal plane of the objective. It is determined by the available STED laser power and the desired resolution. In order to obtain an optical lattice of 3 μm * 3 μm, the size of the beams at the back aperture of the objective is $\Delta r_2 \approx \frac{f_0 \lambda}{n \Delta r_1} \approx 0.55$ mm, with $f_0 = 3.3$ mm, n = 1.515 and $\lambda = 760$ nm.

The lens L3 is installed at the entrance of the microscope and its focal length is therefore set to 300 mm. The initial size (5 mm) of the four beams and the focal lengths of the lenses L1 (500 mm) and L2 (35 mm) are optimized in order to obtain the optical lattice with the target size. According to the magnification of the system, the angle ζ (between the wave vectors of the four beams originating from the SLM and the optical axis) is then set by the SLM to 2.8' to obtain an angle of incidence of 60° at the focal plane of the objective. The four beams diffracted by the SLM initially have linear polarizations along the x-axis, thus the polarizations of two of the beams have to be

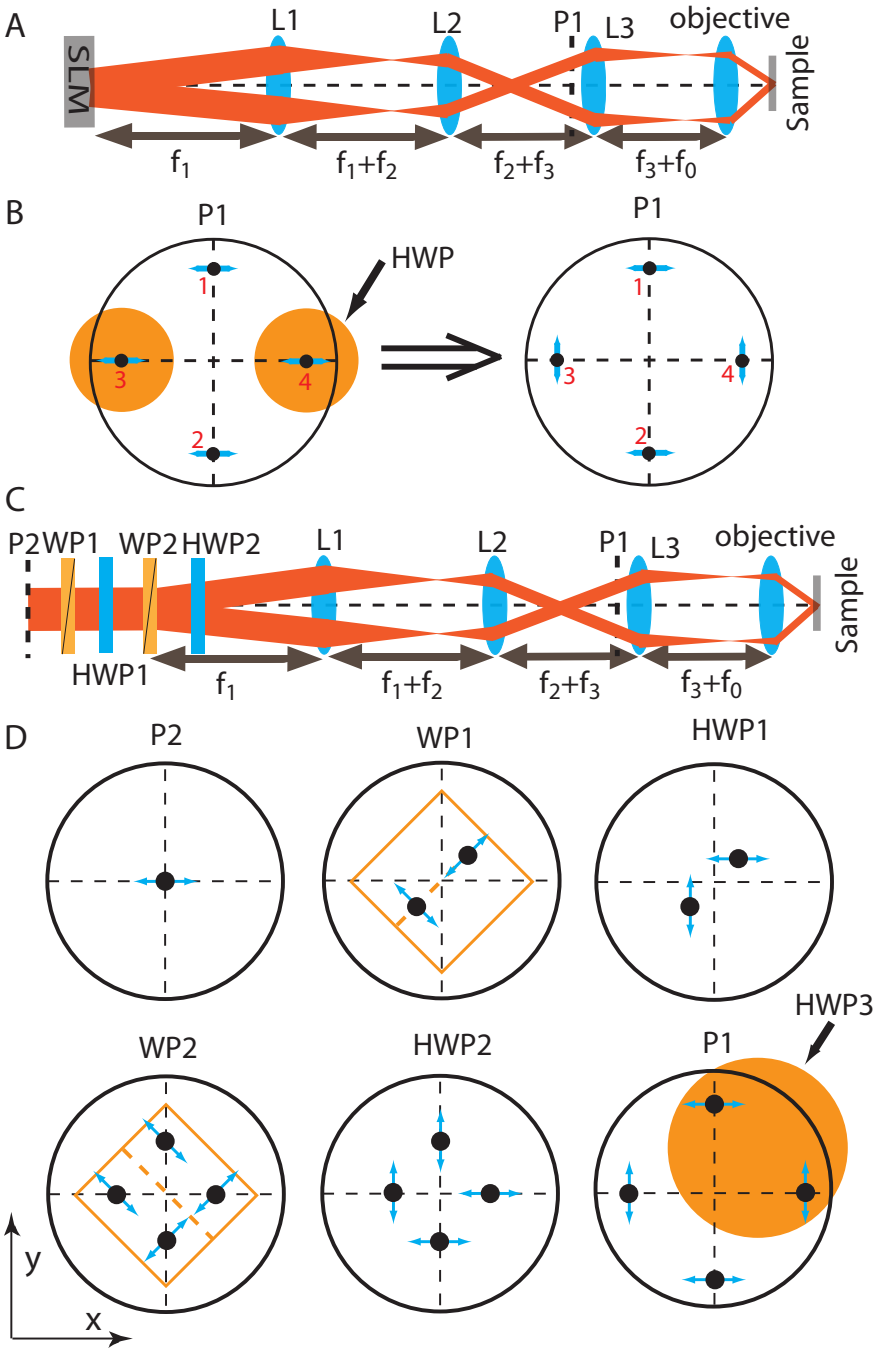

Figure 2.27: Optical setup to produce the four beams (A, C: side views; C, D: transversal planes). The four beams are generated with either a SLM (A, B) or two Wollaston prisms (C, D). The SLM (or the two Wollaston prisms (WP)) are conjugated with the sample plane by a set of lenses (L1, L2 and L3) and the objective, with focal lengths of f_1, f_2, f_3 and f_0, shown in (A) (or C). The polarization of each beam at given transversal planes is shown in (B) (or D). Black spots illustrate the intersections of the beams with the planes, blue double arrows show the polarizations. Yellow circles and squares indicate respectively the half-wave plates (HWP) and the Wollaston prisms. Dashed yellow lines show the beam splitting directions.

rotated with two half-wave plates to be along the y-axis, in order to obtain the desired optical lattice (see Figure 2.27B).

The diffraction efficiency of multi-beam generation with the SLM is about 40%. To minimize the STED power loss, we use two Wollaston prisms (WP) to generate the four beams, shown in Figure 2.27C and D. The initial polarization of the laser beam is linear along the x-axis. The WP1 splits the beam into two, with orthogonal polarizations, $\pm 45^\circ$ to the x-axis. A half-wave plate (HWP1) rotates the polarization of the two beams by 45° to be parallel to the x- or y-axes. The WP2 further splits the two beams into four. At last, two half-wave plates (HWP2 and HWP3) together set the polarizations of the four beams as desired. The efficiency of the two Wollaston prisms to generate the four beams is about 70%, which can be further improved by using prisms with anti-reflection coating at 760 nm.

2.4.3.2 Measurement of the effective excitation PSF

In order to visualize the obtained optical lattice at the focal plane of the objective, we scan a big fluorescent bead ($\sim$ 100 nm) over the field of illumination in presence of both the STED optical lattice and a homogeneous excitation, while recording its fluorescence signal with the camera. For each scanning step, a camera image is acquired and the fluorescence intensity is integrated over the PSF of the bead image. The reconstructed fluorescence map is therefore the effective excitation PSF of the Lattice-STED microscope, shown in Figure 2.28. The bright spots correspond to the intensity "zeros" of the optical lattice (see Figure 2.10A), where the depletion is minimal and the fluorescence is maximal. The effective excitation PSF exhibits cross-like structures, similar to the simulated PSF of a fluorescent bead containing large numbers of fixed molecules when the lattice beams have relative phases $\Delta\Phi \neq 0$ (see Figure. 2.12). The period of the optical lattice is 290 nm. We obtained 100 intensity "zeros" with sufficient depletion, corresponding to a field of view of 2.9 μm * 2.9 μm.

2.4.3.3 Unit cell scanning procedure

To obtain a super-resolution image with the Lattice-STED microscope, the sample is scanned over a unit cell of the optical lattice. We make N * N scan steps inside a unit cell, the distance of each step is then p/N, with p the period of the optical lattice. The scanning is performed with a calibrated piezoelectric scanner, which has relatively long response times (a few ms). In order that the scanner functions well at high speed (800 μs per step), we scan the sample in a zigzag way (see Figure 2.29), instead of a single-direction way.

To demonstrate that scanning the sample in zigzag is an optimal modality compared to single-direction scan, we measure the trajectories of a fluorescent bead for both scanning modalities. A fluorescence image of the bead is first acquired for each scan step. The image is then fitted with a two-dimensional Gaussian function to locate the centroid, which determines the position of the bead with several nanometer precision. Figure 2.30A and B show respectively the trajectories of the bead with the single-direction scan and zigzag scans. In the single-direction scan, the trajectory of the

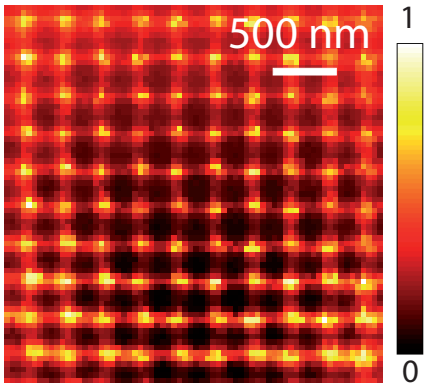

Figure 2.28: Effective excitation PSF of the four-beam Lattice-STED microscope. It is obtained by measuring the fluorescence emitted by a fluorescent bead with a CMOS camera while scanning the bead over a homogeneous excitation beam and the STED optical lattice (3 μm * 3 μm). I_{exc} = 100 W/cm^2, I_{max} = 1.68 MW/cm^2.

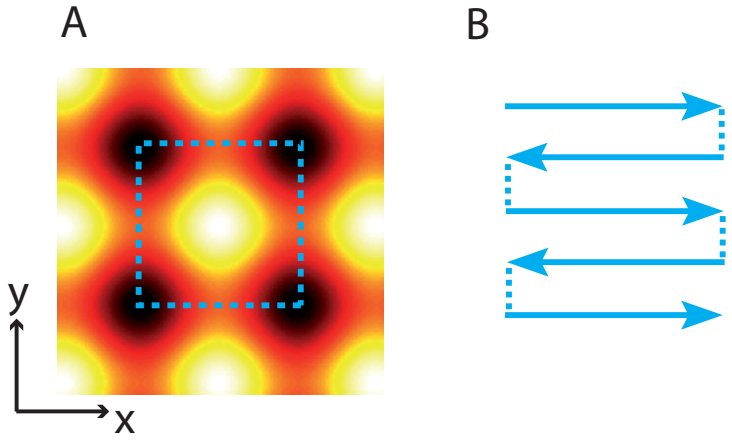

Figure 2.29: Scanning procedure of the four-beam Lattice-STED microscope. (A) shows the unit cell of the optical lattice (blue dashed square). (B) Scanning directions are shown in blue solid arrows. The first line is scanned from left to right, the second from right to left and etc.

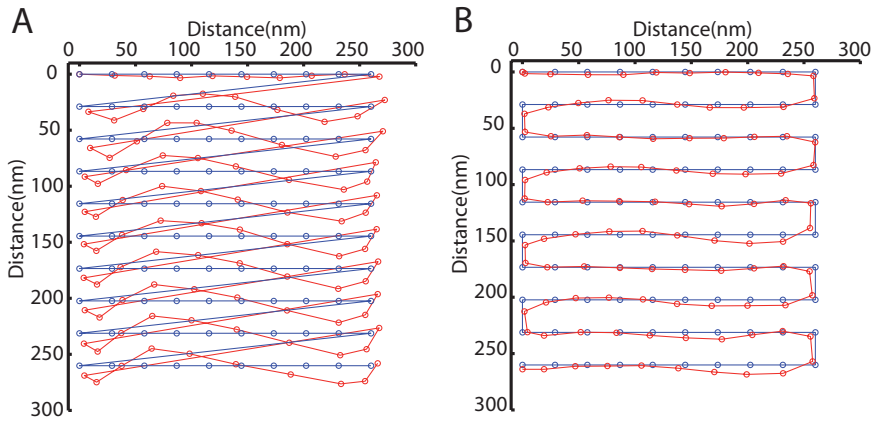

Figure 2.30: Two ways of scanning the sample with the piezoelectric scanner. (A) and (B) are respectively the trajectories of a bead scanned in single-direction and zigzag modalities. A fluorescence image of the bead is acquired for each scan step, the position of the bead is determined by fitting the image with a two-dimensional Gaussian function to locate its centroid. Blue and red lines indicate respectively the desired and measured positions of the bead. The scans in both (A) and (B) are from top to bottom. Time per step 800 μs.

bead exhibits deviations from the desired trajectory except for the first line, due to the response time of the piezoelectric scanner. To reduce these deviations, one can add several steps during the return of the scanner to the initial coordinates and (or) add a time delay before scanning of a new line. However, the acquisition time of a super-resolution image would be longer, thus undesirable. The zigzag scan produces the trajectory with deviations of less than ten nanometers from desired positions. Since the resolution of our Lattice-STED microscope is more than ten nanometers, these deviations are negligible.

2.4.3.4 Parallelized detection with CMOS camera

We use a fast CMOS camera to record the fluorescence signal during the scan. The camera has 2048 * 2048 pixels (6.5 μm * 6.5 μm pixel size), low readout noise (1.9 electrons, given in root mean square). A pixel of the CMOS image sensor is composed of a photodiode and an amplifier that converts charge into voltage. The voltage of each pixel is sent to an analog-to-digital converter and is read out subsequently (see Figure 2.31A). The top and the bottom halves of the sensor are read out independently, with two lines of column amplifier and analog-to-digital converter at the top and at the bottom, as showed in Figure 2.31B. The readout time of a centred region is therefore proportional to the number of lines divided by two. In our experiment, a centred region of 128 * 128 pixels is used, with a readout time of 800 μs.

The camera acquires one frame per scan step. To extract the fluorescence signal originating from each intensity "zeros" of the optical lattice, we overlay on these raw images a binary mask, shown in Figure 2.32B. The transparent parts correspond to the positions of intensity minima of the depletion pattern, i.e. the fluorescence maxima in Figure 2.32A. Therefore, the CMOS camera together with the digital mask act as an array of parallelized "point detectors", each of which records the fluorescence signal originating from corresponding intensity "zero". The magnification of the detection system is set to be 225, by combining the tube lens (X60) of the microscope, an internal and an

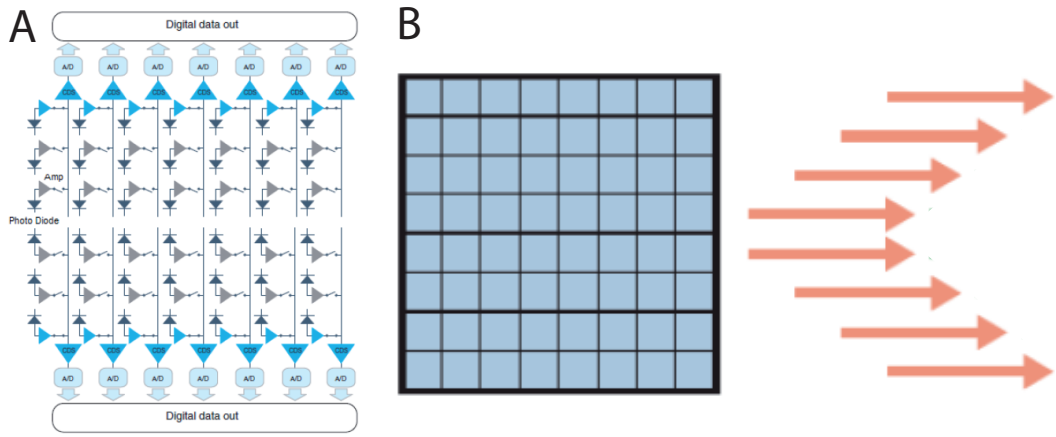

Figure 2.31: Principle of the CMOS camera. A) Electronic structure of the camera. Each pixel is composed of a photodiode and an amplifier. B) Readout of the sensor. The high speed readout is performed by splitting the sensor in two parts where both half sensors are read out simultaneously. Each part is read out line by line successively at a rate of 9.7 μs/line. A region of interest of 128 * 128 pixels is used in our Lattice-STED microscope.

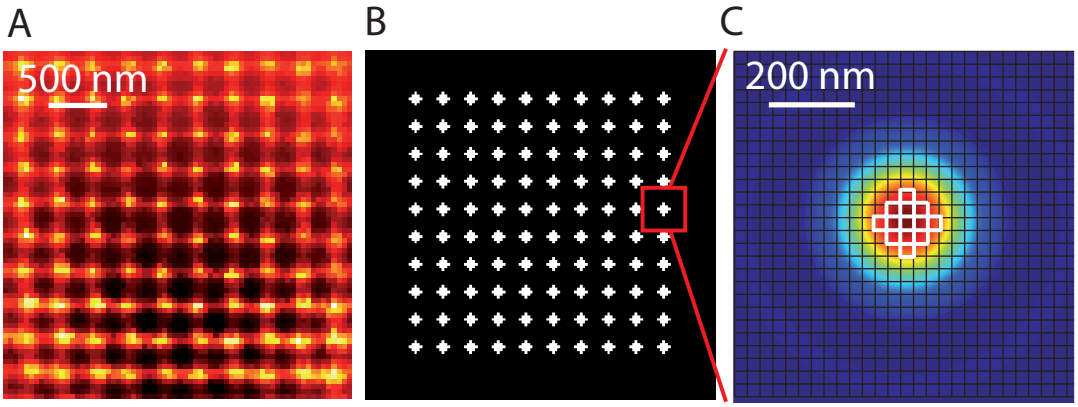

Figure 2.32: Binary mask for the four-beam Lattice-STED microscope. (A) Effective excitation PSF of the four-beam optical lattice combined with a homogeneous excitation. (B) Corresponding binary mask, with black and white parts being respectively opaque and transparent. Each white mask comprises 13 camera pixels and overlaps with one of the fluorescence maxima in A to extract the fluorescence signal. (C) Magnified view of the red square in B. The background shows the simulated emission PSF (FWHM 266 nm) of a fluorophore, with the emission wavelength at 650 nm. The black grid illustrates the pixels of the camera, and the white grid shows the mask.

external magnification systems (X1.5 and X2.5 respectively). Hence the corresponding size of the camera pixel on the focal plane of the objective is 30 nm.

The shape of the "point detectors" is close to a circle, whose size is optimized to obtain a better signal-to-noise ratio of the super-resolution images. The signal-to-noise ratio can be expressed as:

$$SNR = \frac{S_e(N)}{\sqrt{NN_r^2 + S_e(N)}} \tag{2.34}$$

where N is the number of camera pixels included in a "point detector", N_r the readout noise of the camera pixels and S_e the number of electrons detected which is a function of N.

If S_e is much higher than the readout noise, the signal-to-noise ratio is dominated by the photon shot noise. A bigger "point detector" allows collecting more fluorescence, but also increases the number of camera pixels involved, i.e. the related readout noise. Therefore a compromise needs to be found. We apply a binary mask with each "point detector" containing 13 pixels (see Figure 2.32C). The signal-to-noise ratio of the super-resolution image is then about 14 - 31, with $N_r = 1.9$ and S_r about 200 - 1000 (determined from experimental Lattice-STED images, see Figure 2.38 and Figure 2.40).

Another possible issue concerning the size of the "point detectors" is that a "detector" might detect fluorescence of a fluorophore while the fluorophore is around a neighbour intensity minimum, i.e. in the region of a neighbour "detector". To estimate this "cross-talk" between neighbour "detectors", we simulate two "detectors" separated by 290 nm (the period of the optical lattice), as shown in 2.33A. A fluorophore is assumed to be at the center of "detector" 1. The ratio between the fluorescence signals delivered by "detector" 2 and "detector" 1 is obtained as a function of the radius of the "detectors" (see Figure 2.33B). When the radius of the "detectors" is 100 nm, the cross-talk is 2%. The cross-talk between the neighbour "detectors" in the diagonal direction is also considered, which is about 1% for "detectors" with the radius of 100 nm. Despite the small amount

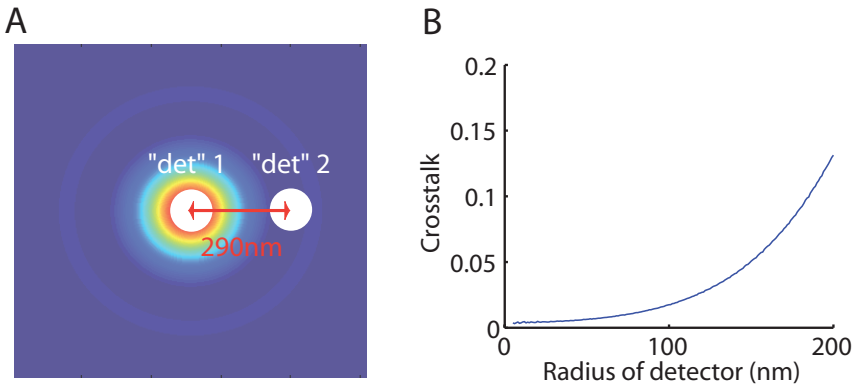

Figure 2.33: "Cross-talk" between two "detectors". A) Two detectors are separated with a distance of 290 nm (period of the optical lattice). The background shows the emission PSF of a fluorophore centred at "detector" 1; B) Evolution of the relative amount of fluorescence detected by "detector" 2 compared to that detected by "detector" 1, as a function of the size of the "detectors".

of cross-talk, the super-resolution images could have artefacts such as "ghosts", meaning that a fluorophore has a brighter image at the right coordinates and darker images appearing in adjacent areas. Therefore we apply a linear unmixing process to the signals delivered by the "detectors" to eliminate the cross-talk (see Appendix B for more details).

2.4.4 Three-beam Lattice-STED

The experimental implementation of three-beam optical lattice is similar to that of the four-beam optical lattice, and will be presented briefly.

We measure the effective excitation PSF by scanning a fluorescent bead in the presence of the three-beam optical lattice and a homogeneous excitation, as shown in Figure 2.34A. The signal maxima correspond to the regions of minimal depletion, which occur at the zero-intensity positions of the optical lattice. As expected, we obtain a hexagonal lattice with the periodicity of 390 nm. The bright spots have slightly elongated shapes due to an angle of incidence (60 °) smaller than the optimal angle (70 °). At the angle of incidence of 60 °, the intensity gradient of the optical lattice is steeper in the horizontal direction than in the vertical direction (see Figure 2.34B and C), there-

fore the resolution is better in the horizontal direction, leading to elongated effective excitation PSF.

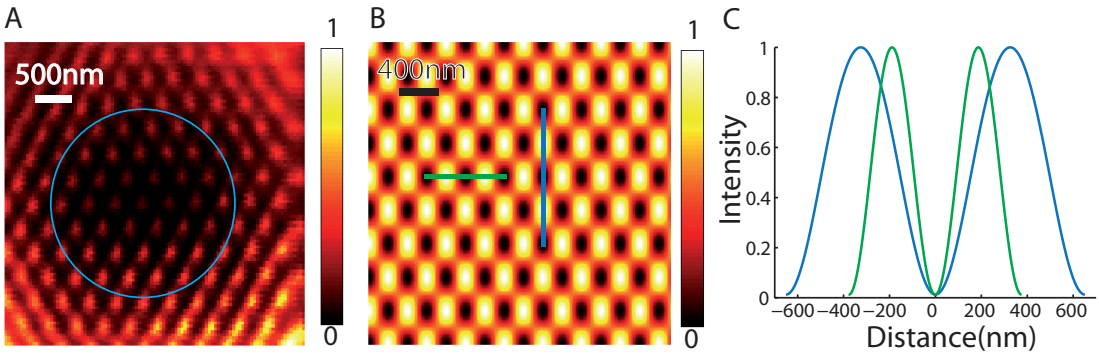

Figure 2.34: Effective excitation PSF of the three-beam Lattice-microscope with a homogeneous excitation. (A) Effective excitation PSF measured by scanning a fluorescence bead across the focal plane of the objective and recording its fluorescence simultaneously. The blue circle (diameter of 2.3 μm) is the region where depletion is efficient enough for the Lattice-STED microscope. Fluorescence is normalized to the maximal value. (B) Intensity distribution of the three-beam optical lattice for the angle of incidence of 60 °, normalized relative to the maximal value. (C) Intensity profiles along the blue and green lines in B.

The depletion intensity is also higher in the center of the field of view, this explains why the bright spot is smaller and darker there. Only the center region (inside the blue circle) with a diameter of 2.3 μm (6 * 390 nm) is used for the Lattice-STED microscope, containing 35 intensity "zeros".

The unit cell of the three-beam optical lattice is also scanned in a zigzag modality, as shown in Figure 2.35. The horizontal length of the unit cell is 390 nm and the vertical length is 338 nm. The number of scan steps are set to be 10 along the horizontal direction and 9 along the vertical direction. The resulting scan steps along the two directions are respectively 39 nm and 37.7 nm.

The camera records 10 * 9 raw images during the scan. We apply a binary mask (see Figure 2.36) on these raw images to extract the fluorescence signal originating from each intensity minima of the optical lattice. The CMOS camera together with the digital

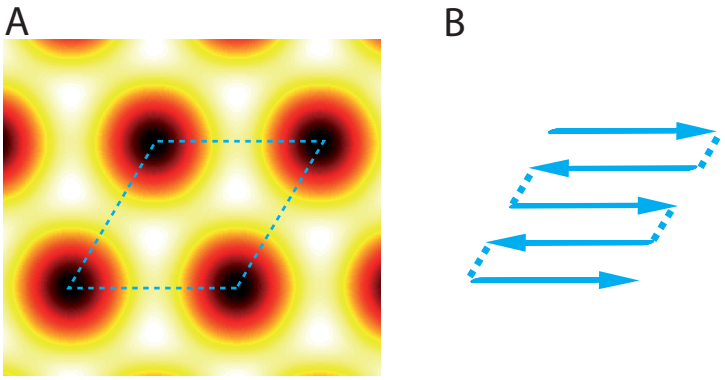

Figure 2.35: Scanning of a unit cell of the three-beam optical lattice. (A) Dashed parallelogram shows the unit cell; (B) Solid arrows show the scan direction.

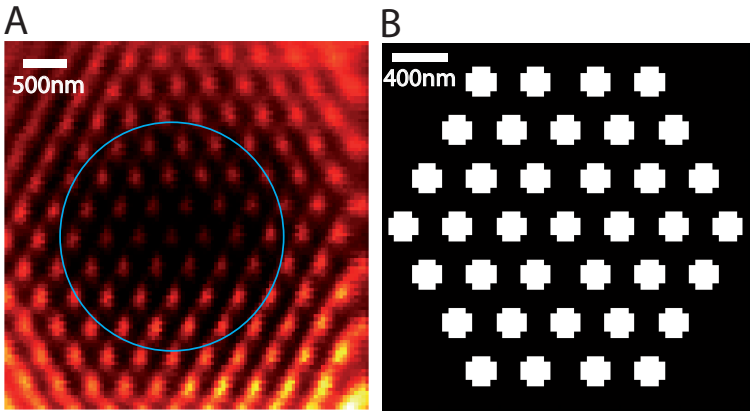

Figure 2.36: Binary mask for the three-beam Lattice-STED microscope. (A) Effective excitation PSF. (B) Binary mask. Black and white parts are respectively opaque and transparent. Each white mask comprises 21 camera pixels.

mask act as an array of parallelized "point detectors". Due to the large distance (390 nm) between neighbour "detectors", the crosstalk between them is small (about 1%) and is therefore negligible. Each "point detector" records a super-resolution sub-image. The final super-resolved image is obtained by assembling all the sub-images together. The sub-images have the parallelogram form as the unit cell of the optical lattice. In order to display the final image, we interpolate the super-resolution image pixels with the Delaunay triangulation [174] based on their coordinates and fluorescence values.

2.5 Results of Lattice-STED microscope

2.5.1 Results of three-beam Lattice-STED

We apply the three-beam Lattice-STED microscope on a sample containing 20 nm fluorescent beads spin-coated on a coverslip. Figure 2.37A and B show respectively the diffraction-limited and super-resolved images, with and without the depletion optical lattice. The super-resolved image clearly shows resolution beyond the diffraction limit. The resolution along the horizontal direction is 90 nm (see Figure 2.37C), about half of that along the vertical direction. The acquisition time of a super-resolution image is determined by the readout time of the camera (800 μs) and the number of scans for a

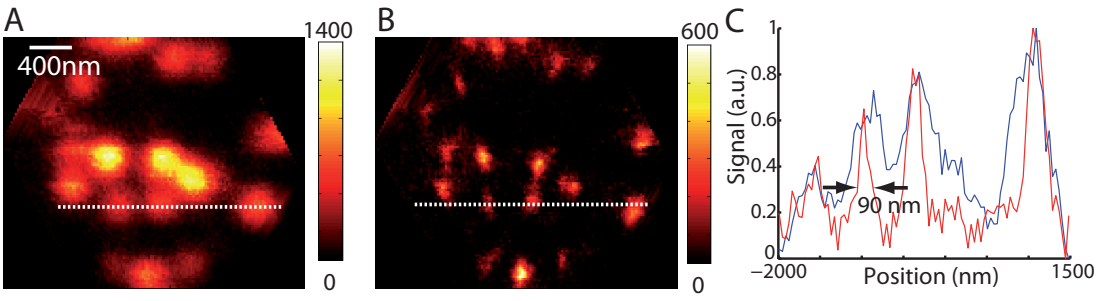

Figure 2.37: Three-beam Lattice-STED imaging of a sample containing 20 nm fluorescent beads. (A) Diffraction limited image; (B) super-resolved image; (C) intensity profiles along the dashed lines in A (blue) and B (red). P_{exc}=2 mW, P_{STED} = 400 mW. Acquisition time: 72 ms per super-resolution image.

unit cell, and is 72 ms.

2.5.2 Results of four-beam Lattice-STED

We then try the four-beam Lattice-STED microscope with 20 nm fluorescent beads. Fig. 2.38A and B show respectively the images without and with the depletion optical lattice, with a field of view of 2.9 μm * 2.9 μm. The diffraction-limited PSF of the beads has a FWHM of 290 nm, while the Lattice-STED image offers better resolution and resolves closely packed beads. The FWHM of the intensity profiles of a bead gives the resolution of the Lattice-STED microscope (70 nm), as showed in Fig. 2.38C. The resolution of STED microscopy depends on the STED intensity, which makes the resolution of the Lattice-STED microscope better in the center where the STED intensity is higher. The resolution at the edge is about 1.4 times (100 nm) that measured in the center.

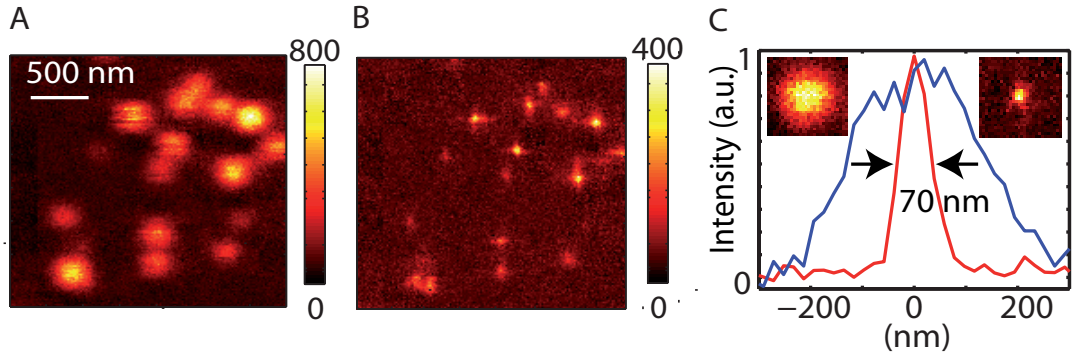

Figure 2.38: Four-beam Lattice-STED imaging of a sample containing 20 nm fluorescent beads. (A) and (B) are respectively the diffraction limited and the super-resolved images without and with the depletion optical lattice. (C) Intensity profiles of a bead without and with the depletion optical lattice. $I_{exc} = 2.5$ kW/cm^2, $I_{max} = 2.4$ MW/cm^2, acquisition speed: 80 ms per super-resolution image.

We then apply the four-beam Lattice-STED microscope to image microtubules labelled with Atto 647N in fixed COS cells. The photobleaching of fluorophores causes fluorescence signal to decrease as a function of time and induces artefacts in the Lattice-

STED image, as showed in Figure 2.39A. The photobleaching-induced artefact is mostly present in the vertical axis, which is the slow scan axis. To correct the signal decrease, we multiply a correction factor to the camera raw images. The correction factor is defined as $e^{N\Delta t/T_{bleach}}$, where N is the number of the raw camera frame, Δt the integration time per frame and T_{bleach} the characteristic time of photobleaching. T_{bleach} is found to be $\sim$ 800 ms for $I_{exc} = 2.5$ kW/cm^2, $I_{max} = 2.4$ MW/cm^2. The super-resolution image after photobleaching correction exhibits no longer discontinuous artefacts, as shown in Figure 2.39B.

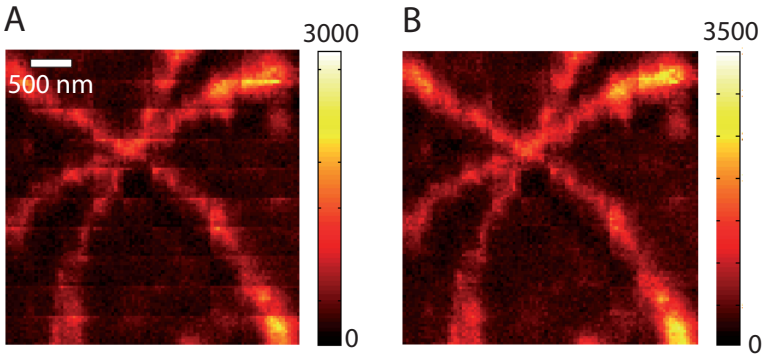

Figure 2.39: Photobleaching compensation in the four-beam Lattice-STED microscope. (A) and (B) show respectively Lattice-STED images without and with photobleaching correction. A correction factor as a function of time is applied to B (see text for more details). $I_{exc} = 2.5$ kW/cm^2, $I_{max} = 2.4$ MW/cm^2, acquisition speed: 80 ms per STED image.

As showed in Figure 2.40A-C, the Lattice-STED microscope gives super-resolved images of tubulin fibers. The resolution is below 100 nm and microtubules distant by less than the diffraction limit are clearly distinguished. Importantly, the acquisition time of an Lattice-STED image is 80 ms, which is only limited by the CMOS camera readout time. The doughnut-STED with fast scanning (fast-STED) requires pixel dwell time down to several μs to tens of μs [47, 175]. To acquire a super-resolution image with the same field of view and image pixel size as Figure 2.40B, the acquisition time of fast-STED is tens of ms to hundreds of ms, comparable to the current temporal

performance of Lattice-STED. However, fast-STED is limited by the number of photons detected during the short pixel dwell time, while the imaging speed of Lattice-STED can be further improved by using faster cameras.

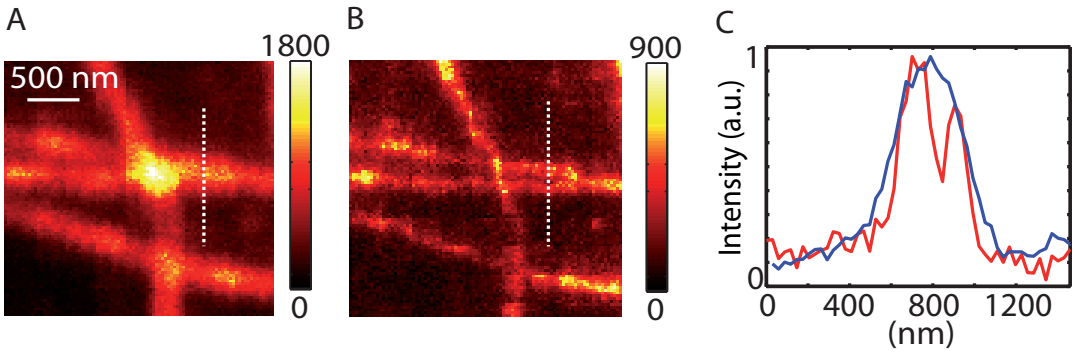

Figure 2.40: Four-beam Lattice-STED imaging of microtubules labelled with ATTO 647N dye in a fixed cell. (A) and (B) are respectively the diffraction limited and super-resolved images without and with the depletion optical lattice. (C) Normalized fluorescence intensity profiles (along the dashed lines). I_{exc} = 2.5 kW/cm^2, I_{max} = 2.4 MW/cm^2, acquisition speed: 80 ms per STED image.

2.6 Reducing the photobleaching of Lattice-STED with structured excitation

The photobleaching of the fluorophores in Lattice-STED microscopy is a constraint when recording large number of super-resolution images. Lattice-STED microscopy illuminates the sample with a homogeneous excitation, molecules are therefore excited even when they are not in the intensity minima of the optical lattice. By exciting the molecules only when they are in the intensity minima, the photobleaching can be reduced. For this purpose, we use a structured excitation instead of a homogeneous one to excite the molecules. As showed in Figure 2.41, we generate an excitation optical lattice (Figure 2.41A) complementary to the depletion optical lattice (Figure 2.41B) (having maxima where the other has minima, and vice versa). Excitation of molecules

occurs thus mainly at regions of zero depletion intensities and the probability that a molecule gets promoted to highly excited and reactive levels is reduced, causing less photobleaching [176, 177].

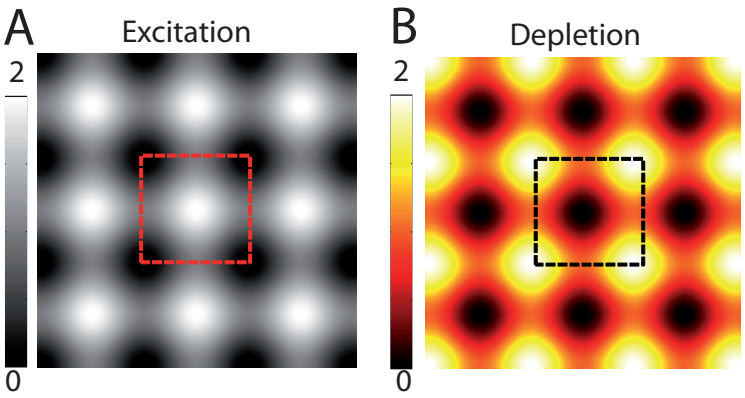

Figure 2.41: Simulations of the intensity distributions of the excitation (A) and STED (B) optical lattices for Lattice-STED. The optical lattices are complementary, i.e. A displays maxima where B has minima, and vice versa. The dashed boxes show the unit cells of the two optical lattices.

Figure 2.42 shows the experimental setup of the Lattice-STED microscope with structured excitation. The setup is similar to Figure 2.22, except that both the excitation and STED beams are divided into four beams, respectively with a SLM (Pluto-Vis, Holoeye) and two Wollaston prisms (W1 and W2), to generate complementary optical lattices. The SLM allows us to tune the incident angle and the relative phases of the excitation beams. The tuning of incident angle adapts the period of the excitation optical lattice to that of the depletion optical lattice. And the tuning of the relative phases can translate the excitation optical lattice, so as to overlay the intensity maxima of the excitation optical lattice with the intensity minima of the depletion optical lattice.

To compare the photobleaching rates of the homogeneous and structured excitation configurations, we record successive Lattice-STED images of a highly concentrated sample of 20 nm fluorescent beads in both cases. We then integrate over all the pixels of the camera images to obtain the total fluorescence and normalize the fluorescence values to

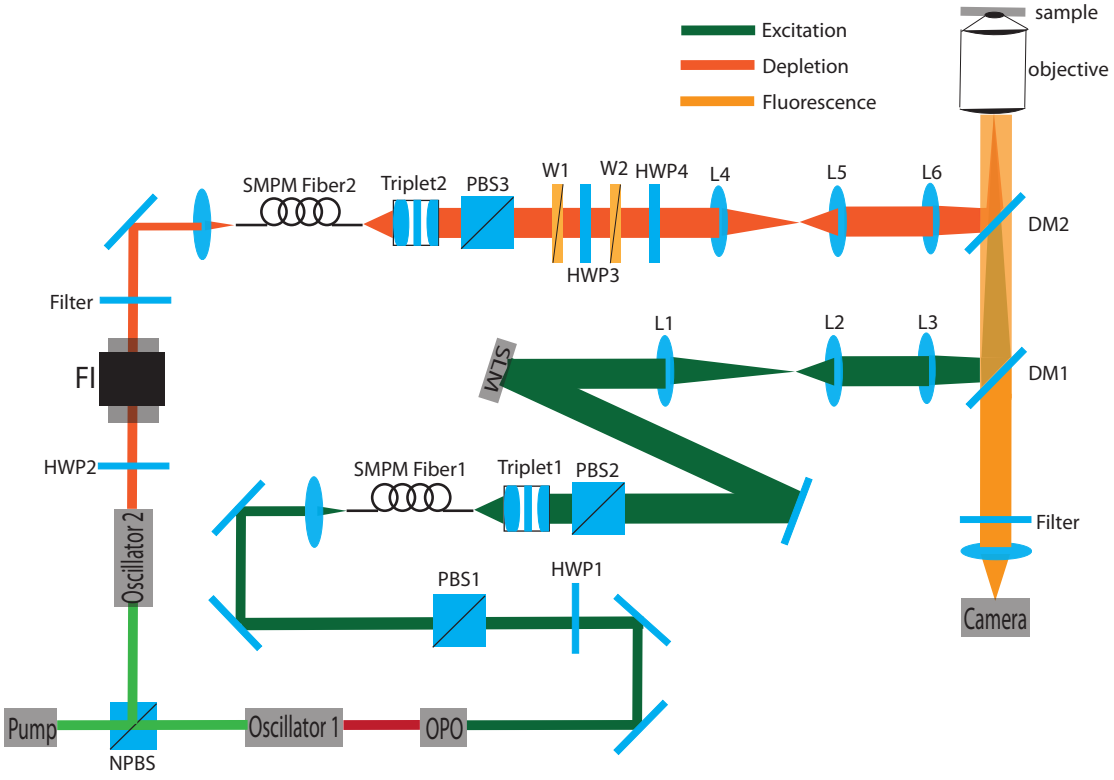

Figure 2.42: Experimental setup of the Lattice-STED microscope with structured excitation and depletion patterns. As before, the depletion optical lattice is obtained with two Wollaston prisms. The excitation one is generated with a spatial light modulator (SLM), which permits the control of the relative phases between the interfering excitation beams and the incident angle of the beams (affecting the period), in order to position the excitation optical lattice over the depletion one. Abbreviations: NPBS : Non-Polarising cube BeamSplitter; HWP: Half-Wave Plate; FI: Faraday Isolator; SMPM Fiber: Single-mode Polarisation-Maintaining Fiber; Triplet: Triplet Fiber Collimator; PBS: Polarizing Beamsplitter; W: Wollaston Prism; L: Lens; SLM: Spatial Light Modulator; DM: Dichroic Mirror.

that of the first image. Figure 2.43 shows the corresponding temporal evolutions of the fluorescence together with their exponential decay fits. In the case of structured excitation, the decay time (44.1 s) is found to be two times longer than that of homogeneous illumination (20.7 s). Therefore, we can acquire two times more super-resolution images using Lattice-STED with structured excitation.

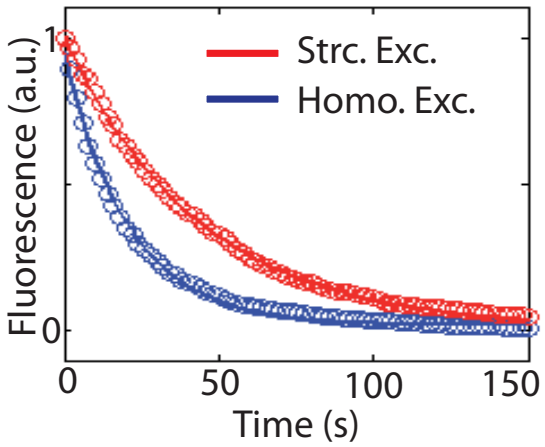

Figure 2.43: Fluorescence decays recorded for the same maximum excitation intensity in the case of structured (red) and homogeneous excitations (blue). An exponential fit gives a decay time of 44.1 s for the structured excitation, two times longer than that for the homogeneous case 20.7 s. $I_{exc} = 127$ W/cm^2, $I_{max} = 1.7$ MW/cm^2.

2.7 Super-resolution imaging of diffusing nanoparticles

The high-speed capability of the Lattice-STED microscope is demonstrated by imaging the movement of 20 nm fluorescent particles in a Carbopol gel (mass percentage 2%). Carbopol polymers [178] are polymers of acrylic acid cross-linked with polyalkenyl ethers or divinyl glycol. The Carbopol resins are hydrophilic substances that are not soluble in water. Rather, these polymers swell when dispersed in water forming a colloidal, mucilage-like dispersion. Most of the beads are static in the Carbopol gel while some of them diffuse. We record successive Lattice-STED images with structured excitation

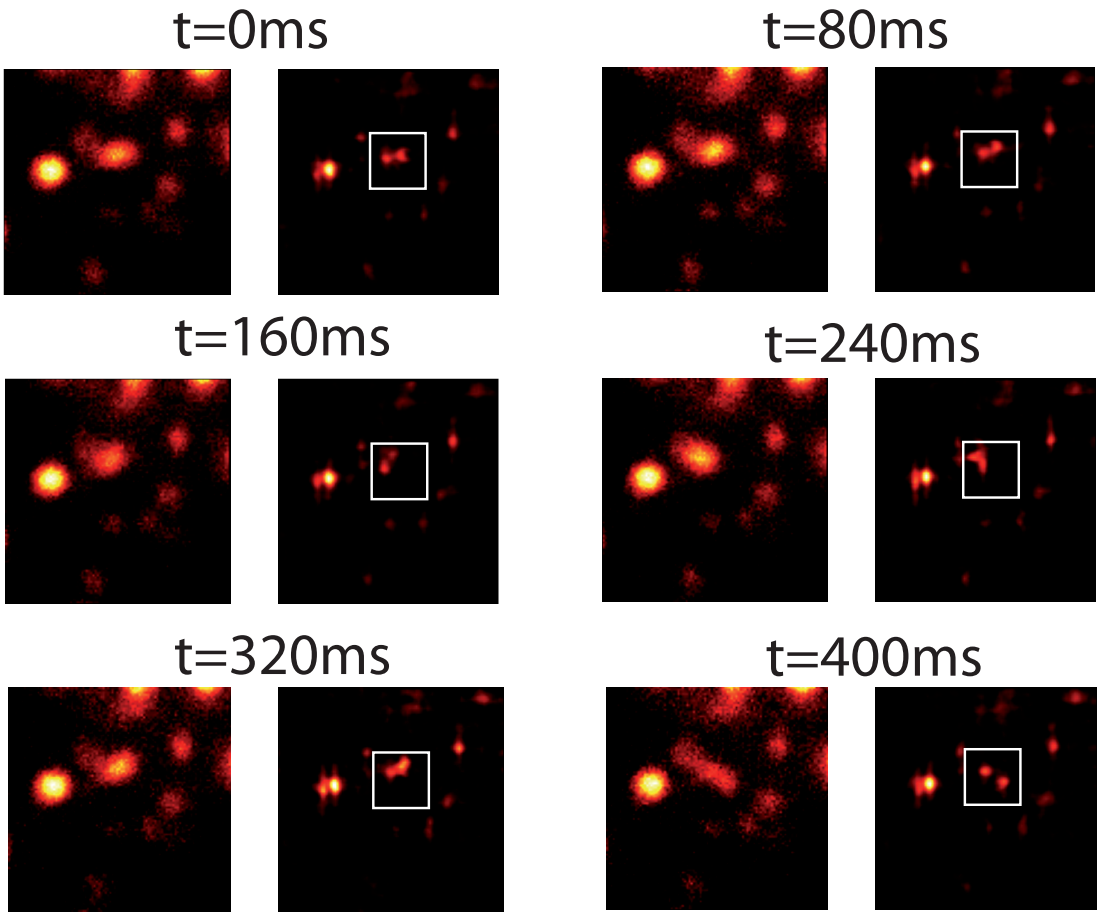

Figure 2.44: Diffraction-limited (left side) and Lattice-STED (right side) successive images of 20 nm fluorescent beads in carbopol gel (concentration 2%). Images are taken at the rate of 80 ms per image with $I_{exc} = 2.2$ kW/cm^2, $I_{max} = 1.7$ MW/cm^2. The squares indicate the region where one bead is moving around another one.

at 12.5 frames per second, shown in Figure 2.44. Interestingly, we clearly show that recording of fast relative movement of two particles separated by a distance well below the diffraction limit is possible with our methodology. We measured the root-mean-square speed of one 20 nm particle in the gel, ~ 450 nm^2/s.

In all microscopes, the moving speed of the diffusing objects should not exceed a certain limit in order to be captured. Similarly, in the Lattice-STED microscope, the moving speed of the nanoparticles should not diffuse more than the effective excitation PSF (FWHM 70 nm) during the acquisition of one super-resolution image, otherwise the resolution is deteriorated. Moreover, if one nanoparticle diffuses more than the size of the unit cell, it will appear in more than one sub-images, inducing "ghosts" in the super-resolution images.

2.8 Conclusion

In this chapter, we presented the parallelization of STED microscopy using both three-beam and four-beam optical lattices. The multi-beam optical lattices contain a large number of intensity minima, allowing a large degree of STED parallelization. Using the four-beam optical lattice, we achieved super-resolution imaging with 70 nm resolution over a field view of 2.9 μm * 2.9 μm at a rate of 12.5 images per second, both with fluorescent beads and microtubules in fixed cells. We also demonstrated the capacity of Lattice-STED at tracking diffusing nanoparticles with super-resolution, which has the potential to perform fast super-resolution imaging in living cells, for example to study cell shaping and migration.

C H A P I T E R 3

Cryogenic super-resolution microscopy by excited state saturation

This chapter presents a super-resolution microscopy based on excited state saturation (ESSat), performed on single organic molecules inserted in solid hosts (guest/host system) at liquid helium temperature. The motivations for performing super-resolution microscopy at cryogenic temperature are discussed in the first section. In the second section, we give a brief introduction to the photophysics of the guest/host system and to the optical saturation of single molecules. The principle of ESSat microscopy is described in the third section, together with analytic expressions for the resolution and with simulations of super-resolution images. The fourth section presents the experimental realization of ESSat microscopy. The experimental results are then shown in the next section. Sub-ten nanometer resolution has been achieved, mainly limited by the mechanical stability of the experimental setup. The last section gives a summary of this chapter and discusses the perspectives of ESSat microscopy.

3.1 Motivations

Far-field super-resolution microscopy techniques are based on the sequential selective imaging of fluorescent emitters [161]. Single organic molecules inserted in solid hosts exhibit distinctive absorption lines at liquid helium temperature, thus are spectrally separable [179]. Achieving super-resolution using spectrally selective imaging was first proposed in 1985 [87], and was experimentally realized in 1998 [88]. However it did not draw much attention at that time. Then, with the success of modern super-resolution microscopies [28,30,34,36], researchers have started again to look for methods to develop super-resolution microscopies at cryogenic temperature.

One of the motivations is for biological applications [180]. In order to preserve the biological structures in the best condition, living cells should be imaged, but this remains very challenging with super-resolution microscopy techniques [44,47]. Typically, at room temperature, the movements of the structures of interest in cells are immobilized by chemical fixation to achieve the best technical results, which however can cause structural change. The cryo-immobilization can preserve the structures in a near-native state in glass-like amorphous ice [181], and is frequently used in the fields of electron and X-ray cryo-microscopy [182, 183]. However, oil-immersion objectives are not compatible with cryogenic temperature and solid-immersion based optical systems have limited fields of view (a few tens of microns) [184, 185]. The lack of suitable high NA objectives therefore limits the resolution of a cryo-fluorescence microscope to ~ 500 nm, stimulating the development of cryogenic super-resolution methods. For this purpose, localization-based super-resolution microscopy [186–188] has been recently implemented at cryogenic temperature.

Another motivation for developing cryogenic super-resolution techniques is for quantum optical applications. In this context, single quantum emitters have been the subject of thorough investigations. They proved to be efficient and stable single photon

sources [189–191]; strong coherent coupling between single emitters [192, 193] or between emitters and nanostructures [194, 195] have attracted much attention in the applications to quantum computing and quantum communication. In 2002, Hettich et al. achieved super-resolution by performing cryogenic laser spectroscopy under a scanning probe electrode that induces a local electric field [193]. Two molecules separated by 12 nm underwent a strong coherent dipole-dipole coupling that produced entangled sub- and super-radiant states. Since the coupling strength scales with $1/r^3$, where r is the distance between the two dipoles [196], a nanometric distance is required to achieve the strong coupling regime. Super-resolution method are thus required to observe this phenomenon. However, this method applies only to molecules displaying Stark shift and is experimentally difficult to realize.

During this thesis, we performed both direct-ESSat and modulated-ESSat microscopies with single fluorescent organic molecules in solid hosts at liquid helium temperature. Sub-ten nanometer resolution can be obtained with reduced laser intensities (few tens of kW/cm^2), which offers new opportunities to study coherent coupling and interactions between single molecules.

3.2 Single molecules at cryogenic temperature and optical saturation

In 1989, W.E. Moerner and L. Kador [197] detected single molecules in a solid host at liquid helium temperature (T = 2 K) for the first time. Despite their technique of double modulation absorption, the signal-to-noise ratio was low. M. Orrit and J. Bernard [24] have introduced single molecule detection by fluorescence excitation which offers an excellent signal-to-noise ratio. It has opened the way for many single molecule applications, such as single molecule spectroscopy in condensed matter [198], imaging [84] and quantum information [189, 190].

3.2.1 Physical principles

The energy levels of a molecule inserted in a host matrix can be depicted as in Figure 3.1. The electronic states can be simplified as three states: the singlet ground state S_0, the first singlet excited state S_1, and the triplet excited state T_1. The molecular vibrational levels of the molecule and the phonon states of the host add on top of each electronic levels. Various transitions are possible. Radiative transitions are indicated by solid arrows and non-radiative transitions by dashed arrows. Excitation of the molecule can involve electronic, vibrational and phonon states. In most low-temperature experiments, molecules are excited from the lowest vibrational level of S_0 to the lowest vibrational level of S_1. This transition is referred to as the 0-0 transition and is a purely electronic zero-phonon transition. In well chosen host-guest systems at 2K, dephasing of the transition dipole owing to phonons is drastically reduced, and the zero-phonon linewidth of a single

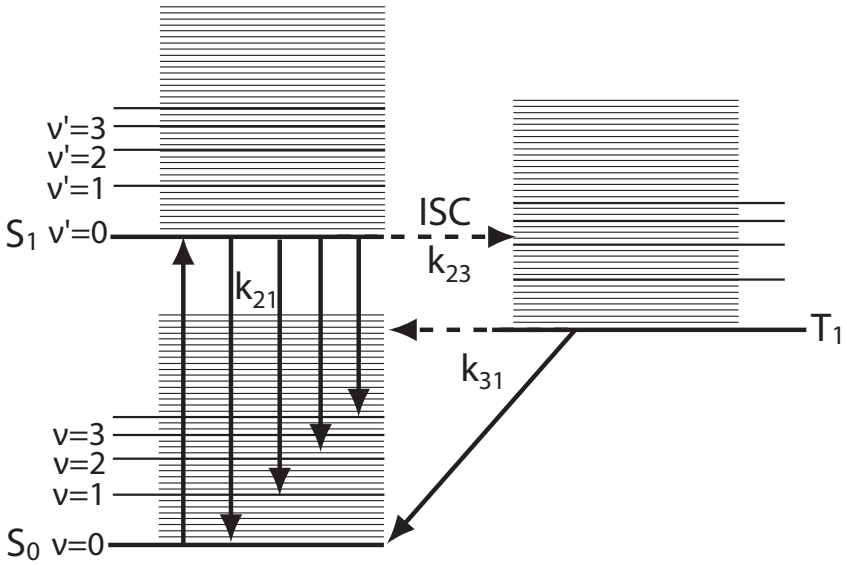

Figure 3.1: Jablonski diagram of a single molecule embedded in a solid. The thickest lines indicate the lowest energy levels of each state. Lines marked with ν are vibrational levels. The thinnest lines denote the phonon states of the host. Inter-system crossing (ISC) and decays rates (k_{21}, k_{23} and k_{31}) are shown. Solid arrows indicate the radiative transitions and dashed arrows show the non-radiative ones.

molecule is lifetime-limited. Excitations involving phonons are blue-shifted with respect to the zero-phonon transition, which build up the phonon sideband (see Figure 3.2). Optical transitions also exist between the ground state S_0 and vibronic states, i.e. exited vibrational levels of S_1. After excitation into a vibronic state, rapid (in the picosecond timescale) non-radiative relaxation brings the molecule into the lowest vibrational level of S_1, from which radiative relaxation to S_0 takes place. The linewidth of a vibronic transition is typically $\sim$ 1 cm^{-1}, three orders of magnitude broader than that of the zero-phonon line.

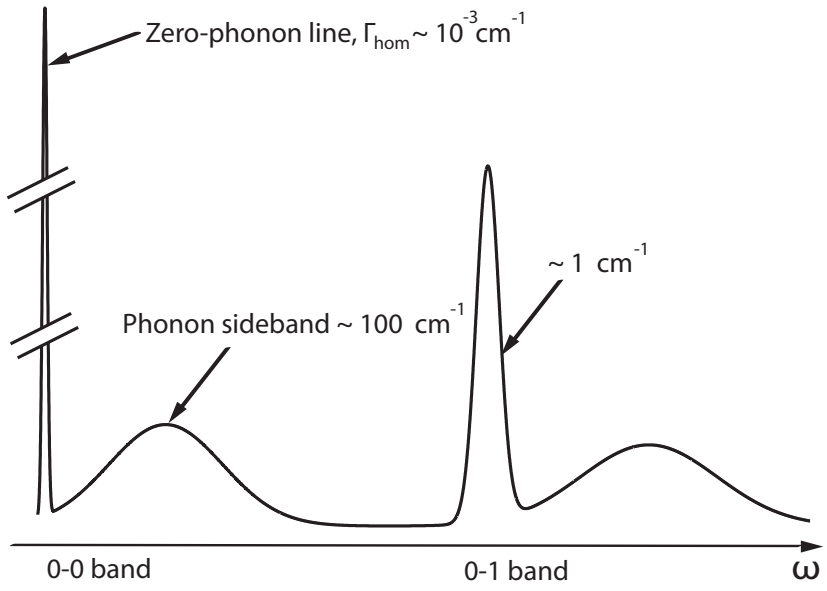

Figure 3.2: Schematic absorption spectrum of a single molecule showing only two vibronic bands.

After excitation to S_1, the molecule can decay to S_0 by emitting a photon. The emission of a photon with the same energy as the absorbed photon is called the "resonance fluorescence". Decay to exited vibrational levels of S_0 occurs by emission of a red-shifted photon, which is called the "Stokes-shifted fluorescence". Further de-excitation of the molecule to the lowest vibrational level of S_0 takes place by non-radiative processes,

converting the excess electronic energy into heat by the creation of phonons. Relaxation from S_1 to S_0 is also possible by the creation of a large number of phonons, called "internal conversion". Alternatively, a normally spin-forbidden transition from S_1 to the metastable triplet state T_1 can occur via a spin-orbit coupling between iso-energetic vibrational levels of the electronic states, called "inter-system crossing". Inter-system crossing to vibrational levels of T_1 is followed by a non-radiative decay to the triplet ground state, with the creation of phonons. From the triplet ground state, the decay to the singlet ground state takes place either by radiative transitions called "phosphorescence" or non-radiative transitions via back inter-system crossing. Since these transitions are spin-forbidden, they occur with low probability.

Decay rates are referred to as k_{ij}, where i denotes the state from which the transition takes place and j the state into which the transition ends up. The lifetime of the lowest vibrational level of S_1 is on the order of nanoseconds, much longer than that of other vibrational levels (picoseconds). The triplet ground state has a much longer lifetime (from microseconds to seconds), which limits the fluorescence emission rate at high excitation intensities, referred to as the "triplet bottleneck".

The relative intensities of the vibronic lines and phonon sidebands with respect to the zero-phonon line, in an absorption or an emission spectrum, are determined respectively by the Franck-Condon and the Debye-Waller factors. The Franck-Condon factor is determined by the intermolecular properties and takes into account the vibrational levels. The Debye-Waller factor is a measure of the relative intensity of the zero-phonon line and the phonon sideband. It decreases exponentially with temperature.

In fluorescence excitation experiments, the molecule is excited at the zero-phonon line. The Stokes-shifted fluorescence is detected by the photo-detector, with filters placed before to block the scattered excitation light.

3.2.2 Spectral selection of single molecule

One way to detect single molecules is to reduce the concentration of the impurity molecules. The concentration is sufficiently reduced when only one molecule is at resonance with the excitation frequency in the illumination volume. This method is referred to as "spatial selection". Due to the narrow zero-phonon lines at low temperature, the number of molecules at resonance with a single-frequency laser beam in the illumination volume is much less at cryogenic temperature than at room temperature, for a given concentration. Thus the zero-phonon lines give rise to an additional dimension to address single molecules, which is called "spectral selection".

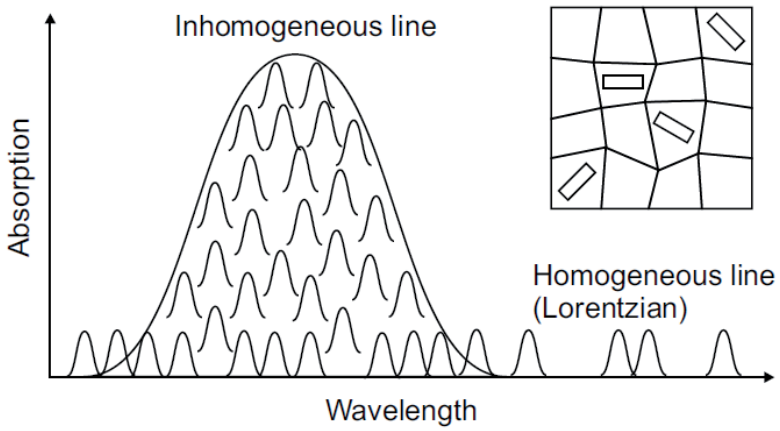

Figure 3.3: Principle of the spectral selection of single molecules in solid hosts at cryogenic temperature. The inhomogeneous line is formed by the sum of all the homogeneous lines of the molecules. Single molecules have absorption lines with different frequencies due to their different local host environments, as depicted in the right top corner. The general structure illustrates the host matrix and the rectangle indicates the impurity molecules.

Due to various local host environments, the zero-phonon absorption lines of single molecules have different frequencies (see Figure 3.3). The ensemble spectrum, which is the sum of the homogeneous zero-phonon lines of all single molecules, displays therefore a broad "inhomogeneous band". The width of the inhomogeneous band reflects the

distribution of interaction strengths between the impurity molecules and the host matrix. A laser with a bandwidth narrower than the homogeneous linewidth is used to perform spectral selection, such that a molecule goes in and out of resonance when scanning the laser frequency. A fluorescence excitation spectrum over the inhomogeneous band of terrylene molecules embedded in a p-terphenyl single crystal is exemplified in Figure 3.4. In the red wing of the inhomogeneous band, one can distinguish single molecules which are spectrally well isolated and display a signal to noise ratio better than ten.

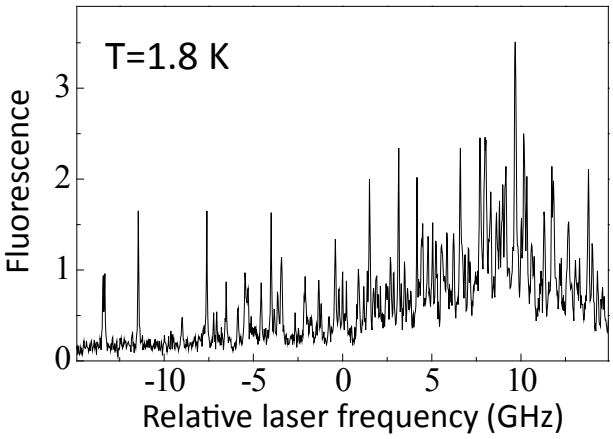

Figure 3.4: Excitation spectrum of single terrylene molecules in the X_2 site of a p-terphenyl crystal. Laser wavelength at 578.5 nm, excitation intensity 1 W/cm^2.

The FWHM of the homogeneous line of a single molecule in frequency units can be expressed as:

$$\Delta\nu_{hom} = \frac{1}{\pi T_2} = \frac{1}{2\pi T_1} + \frac{1}{\pi T_2^*} \tag{3.1}$$

where T_2 is the total dephasing time of the optical transition. T_1 represents the lifetime of the exited level, which takes into account both the radiative and non-radiative relaxation processes. T_2^* represents the pure dephasing time of the transition dipole. Dephasing is caused by a coupling of the molecular electronic transition to low frequency matrix vibrational modes like phonons and librations. Excitation of these modes strongly depends on temperature, such that dephasing usually vanishes below 2K. The zero-phonon

linewidth of a single molecule therefore reaches its fundamental lower bound determined by the excited state lifetime.

The effective photon-capture area of a single molecule under resonant excitation is given by the absorption cross-section. In the limit of low laser intensities, the absorption cross section σ of the zero-phonon line of single molecules in a solid can be written as

$$\sigma = \alpha_{FC}\alpha_{DW}\frac{3\lambda^2}{2\pi}\frac{T_2}{2T_{1,rad}}cos^2\theta \tag{3.2}$$

where λ is the wavelength and $T_{1,rad}$ the radiative lifetime of the excited sate. α_{FC} and α_{DW} are the Franck-Condon and the Debye-Waller factors. $cos^2\theta$ takes into account the angle θ between the transition dipole moment and the laser field polarization.

The main contribution of the cross section comes from the factor $3\lambda^2/(2\pi)$, which is $1.6 \cdot 10^{-9}$ cm^2 at $\lambda = 589$ nm. Taking $\theta = 0$, the other factors contribute by about 0.1 at low temperature. Therefore typical values of the absorption cross-section of a single molecule at 2K are at the order of 10^{-10} cm^2. They are about 10^6 times larger than the absorption cross-sections of dye molecules at room temperature, which are about 10^{-16} cm^2 [199, 200].

3.2.3 Optical saturation of single molecules

At low excitation intensity, the number of photons absorbed by the molecule varies linearly with the excitation intensity. Increasing the excitation intensity will eventually saturate the population of the excited state. Therefore the absorption cross-section of a molecule depends on the light intensity and can be described as [201]:

$$\sigma(I) = \frac{\sigma(0)}{1 + I/I_S} \tag{3.3}$$

where $\sigma(0)$ is the cross section at low light intensity, I the excitation laser intensity and I_S the saturation intensity. For a three-level system including S_0, S_1 and T_1, the

saturation intensity is derived from optical Bloch equations and is given by [202]:

$$I_S = \frac{h\nu}{2\,\sigma(0)\,T_1}\Big[\frac{1}{1+k_{23}/2k_{31}}\Big]. \tag{3.4}$$

Note that from Equation 3.4, we can obtain the saturation intensity of a two-level system by setting $k_{23}/2k_{31} = 0$.

The effects of optical saturation on the fluorescence emission rate $R(I)$ and the absorption linewidth $\Delta\nu_{hom}(I)$ of the molecule are given by:

$$R(I) = R_\infty \frac{I/I_S}{1+I/I_S}, \tag{3.5}$$

$$\Delta\nu_{hom}(I) = \Delta\nu_{hom}(0)\sqrt{1+I/I_S} \tag{3.6}$$

where R_∞ is the maximal emission rate and $\Delta\nu_{hom}(0)$ the homogeneous linewidth.

We have experimentally investigated the fluorescence saturation of single DBATT molecules in octadecane. Figure 3.5 shows fluorescence excitation spectra of a DBATT molecule with excitation intensities varying between 0.1 kW/cm^2 and 2.5 kW/cm^2. Increasing the excitation intensity leads to both a line broadening and a raise of the fluorescence signal. Figure 3.6A shows the experimental fit of the linewidths by Equation 3.6, yielding the homogeneous linewidth $\Delta\nu_{hom}(0) = 50$ MHz and the saturation intensity $I_S = 3$ W/cm^2. We find the same saturation intensity by fitting the intensity dependence of the fluorescence signal with Equation 3.5 (see Figure 3.6B). The polarization of the excitation light is set circular in order to excite identically molecules with dipole moments spread in the sample plane. The measured I_S for different molecules is between 1 W/cm^2 and 5 W/cm^2. Such saturation intensities are about 10^5 times lower than those obtained at room temperature.

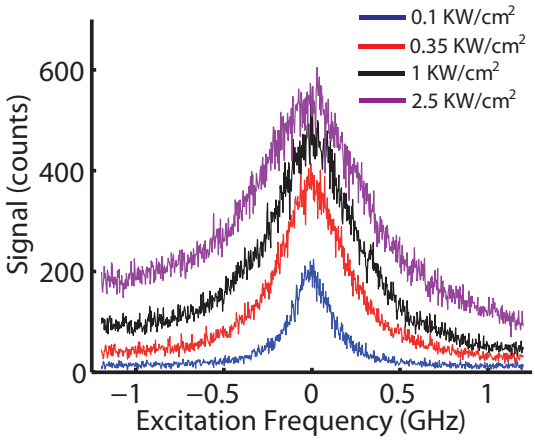

Figure 3.5: Fluorescence excitation spectra of a DBATT molecule in octadecane, measured at different excitation intensities.

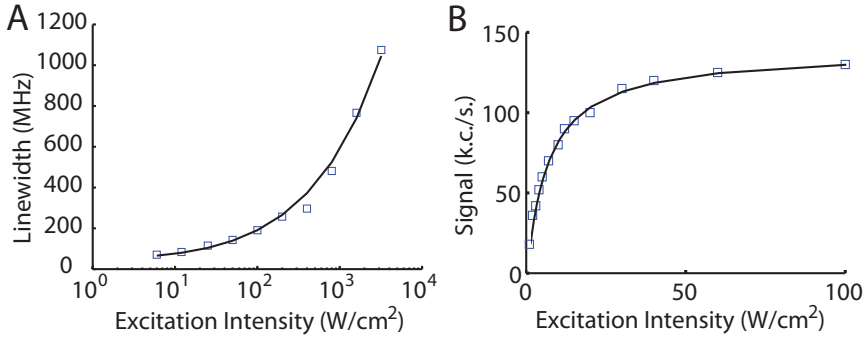

Figure 3.6: Optical saturation of a single molecule. (A) Broadening of the linewidth. (B) Saturation of the fluorescence signal. The squares indicate the experimental data, solid lines show the fits with Equation 3.6 (A) and Equation 3.5 (B).

3.3 Principle of super-resolution microscopy based on excited state saturation

In this section, I will explain how to achieve super-resolution by exploiting the optical saturation of single molecules at cryogenic temperature. Two methods will be presented. In the first one, named direct-ESSat microscopy, molecules are excited only with a doughnut-shaped beam. The resulting images of the molecules are "negative" super-resolution images, in which molecules are localized by local fluorescence minima. The second one is called modulated-ESSat microscopy. The molecules are excited with both a high intensity doughnut beam and a temporally-modulated Gaussian beam. The modulated-ESSat microscopy gives "positive" images which offer a better contrast than that obtained with direct-ESSat microscopy.

3.3.1 Direct-excited state saturation microscopy

We aim at simulating the fluorescence image of a molecule in direct-ESSat microscopy. The image is obtained by recording the fluorescence intensity emitted by the molecule while scanning the molecule across the doughnut beam in the focal plane of the objective. The intensity distribution of the doughnut beam can be described as:

$$I_{donut}(r) = eI_D \frac{4r^2}{d^2} exp(-\frac{4r^2}{d^2}) \tag{3.7}$$

where I_D is the maximal intensity of the doughnut beam and d the diameter (the distance between two opposing intensity maxima) of the doughnut beam. For $\lambda = 589$ nm and an objective with $NA = 0.95$, $d = \lambda/NA = 620$ nm.

At low intensity, the fluorescence of the molecule is proportional to the excitation intensity. The image of the molecule thus reproduces the intensity profile of the doughnut beam (see Figure 3.7A). The resolution can be defined as the FWHM (290 nm) of the

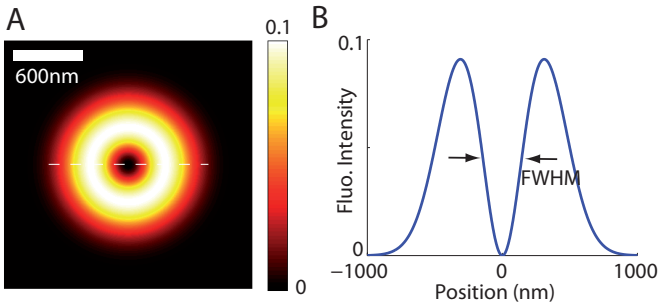

Figure 3.7: (A) Simulated image of a molecule excited with a doughnut beam. (B) Cross-sectional profile of the image along the dashed line in A, whose FWHM determines the resolution. $I_D = 0.1 I_S$. The fluorescence signal is given in unit of R_∞, the fluorescence signal given by one molecule at full saturation.

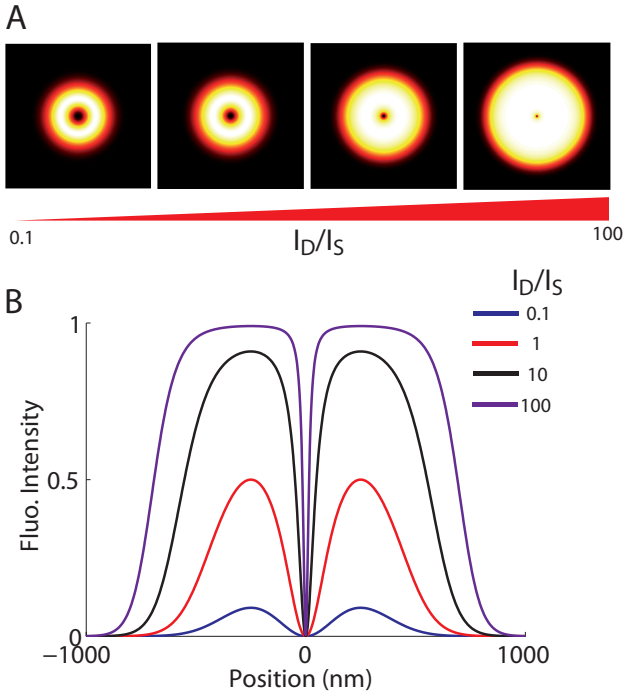

Figure 3.8: (A) Simulated images of a molecule excited with a doughnut beam for various saturation parameters I_D/I_S; (B) cross-sectional profiles of the fluorescence intensity. The fluorescence signal is given in unit of R_∞.

central dip of the doughnut image (see Figure 3.7B).

Due to the optical saturation of the molecule, increasing the excitation intensity leads to a broadening of the doughnut image and a sharpening of the central dip, i.e. to resolution enhancement. Simulated images of a molecule excited at various I_D between $0.1I_S$ to $100I_S$ are shown in Figure 3.8A. The cross-sectional profiles displayed in Figure 3.8B show that the width of the central dip is drastically reduced above the onset of optical saturation.

To provide an analytical expression of the resolution Δr as a function of the excitation intensity I_D, we approximate the intensity distribution of the doughnut beam with a sine function near the optical axis (see Chapter 1):

$$I_{donut}(r) = I_D sin^2(\frac{\pi r}{d}). \tag{3.8}$$

The maximal fluorescence emission rate in a doughnut image is therefore $R(I_D)$. Assuming that the fluorescence emission rate $R(I(r_0))$ is half of $R(I_D)$ at $r = r_0$, the resolution $\Delta r = 2r_0$ is given by:

$$\Delta r = \frac{2d}{\pi} arcsin\Big[\frac{1}{\sqrt{2 + I_D/I_S}}\Big]. \tag{3.9}$$

Figure 3.9 shows that the resolution of direct-ESSat microscopy tends to be infinitely small while increasing I_D/I_S, based on Equation 3.9. At high intensities $I_D \gg I_S$, Equation 3.22 can be simplified as:

$$\Delta r = \frac{2d}{\pi\sqrt{I_D/I_S}}. \tag{3.10}$$

Since the saturation intensity I_S of single molecules at cryogenic temperature is of the order of 1 W/cm^2, a laser intensity on the order of 1 kW/cm^2 is enough to achieve nanometric resolution.

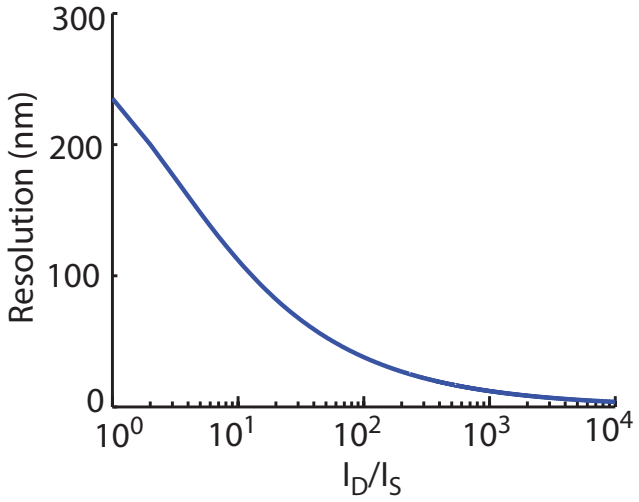

Figure 3.9: Resolution of direct-ESSat microscopy as a function of the doughnut beam intensity.

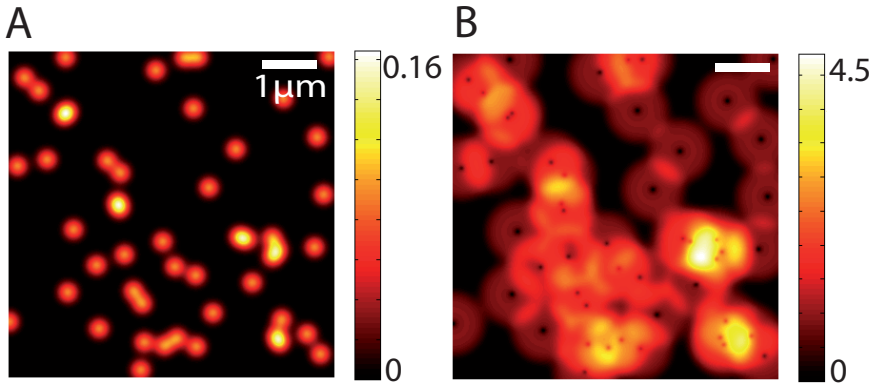

Figure 3.10: Simulated images of 50 identical single molecules. (A) Confocal image, $I_G/I_S = 0.1$; (B) direct-ESSat image, $I_D/I_S = 10$. The fluorescence signal is given in the unit of R_∞.

We then simulate the fluorescence intensity distribution in an image of 50 randomly located identical molecules. Figure 3.10A shows a conventional confocal image obtained with a Gaussian beam having the intensity distribution:

$$I_{Gaussian} = I_G \, exp(-\frac{2r^2}{w_0^2}) \tag{3.11}$$

where I_G and w_0 are respectively the maximal intensity and the waist of the Gaussian beam. Its FWHM is 380 nm. The brightest spots suggest the contribution of more than one molecule to their fluorescence intensity.

Figure 3.10B shows the direct-ESSat image obtained with a doughnut beam at $I_D/I_S = 10$. We can clearly resolve molecules which are not resolvable in Figure 3.10A. However, when more than two molecules are present in the focal spot, the fluorescence signal of each molecule adds a background signal to the other one, which degrades the contrast of the central dip.

3.3.2 Modulated-excited state saturation microscopy

In order to improve the image contrast, we introduce "modulated-ESSat microscopy". A temporally modulated Gaussian beam is added to the doughnut beam to excite the molecules.

Figure 3.11A shows the intensity profiles of the doughnut beam (blue) and the Gaussian beam (red). The doughnut beam has the maximal intensity much higher than I_S and saturates the molecule except in its center. The Gaussian beam has a maximal intensity equal to I_S. Figure 3.11B is an illustration of the principle of the modulated-ESSat microscopy. The blue and red curves are respectively the fluorescence profiles of the molecule, excited with only the doughnut beam and only the Gaussian beam (not modulated). In modulated-ESSat microscopy, both beams excite the molecule, so that the excitation intensity is $I_{total}(t) = I_{donut} + I_{Gaussian}(t)$. Since the Gaussian beam is

temporally modulated, it induces a fluorescence intensity modulation. The amplitude of this modulation strongly depends on the position of the molecule with respect to the doughnut beam. It is maximal when the molecule is submitted to the weakest doughnut beam intensity, i.e. in the doughnut center. The yellow curve in Figure 3.11B shows the amplitude of the fluorescence intensity modulation, plotted as a function of the position of the molecule. It constitutes the effective excitation PSF, which is much smaller than the diffraction limit.

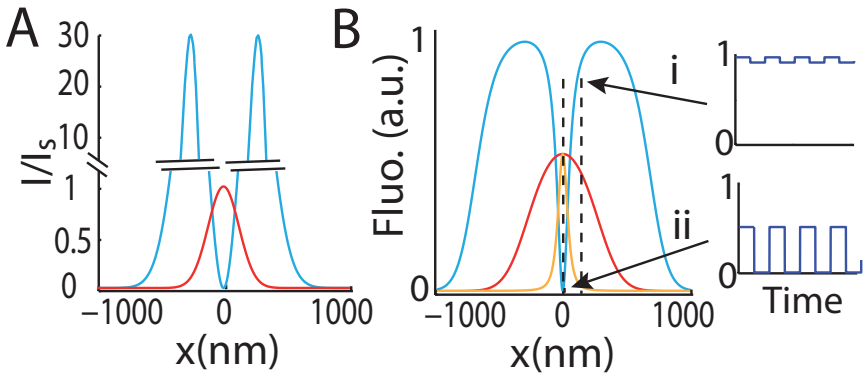

Figure 3.11: Principle of modulated-ESSat microscopy. (A) Intensity profiles of the doughnut beam (blue) and the Gaussian beam (red). $I_D \gg I_S$ and $I_G = I_S$; (B) fluorescence signal of a molecule submitted to the doughnut beam and to the Gaussian beam. The doughnut beam saturates the molecule except in the center. The Gaussian beam is temporally modulated, which induces a modulation of the fluorescence intensity. The insets "i" and "ii" indicate the fluorescence intensity modulations for two positions of the molecule. The yellow curve shows the amplitude of the fluorescence intensity modulation as a function of the position of the molecule (the effective excitation PSF).

A demodulation method is applied to extract the amplitude of the fluorescence intensity modulation. For simplicity, we consider a single cosine modulation of the Gaussian beam:

$$I_{Gaussian}(r,t) = I_G \frac{1 + cos(2\pi\nu t)}{2} exp(-\frac{2r^2}{w_0^2}) \tag{3.12}$$

where ν is the modulation frequency.

At moderate Gaussian beam intensity ($I_G \leq I_S$), the detected count rate of a single

molecule can be modelled as:

$$S = S_0 + \Delta S \frac{1 + cos(2\pi\nu t)}{2} \tag{3.13}$$

where S_0 is the fluorescence signal of the molecule due to the doughnut beam excitation. ΔS is the amplitude of the fluorescence intensity modulation, induced by the Gaussian beam intensity modulated at frequency ν. Fourier transform is then applied on Equation 3.13 to extract ΔS.

An image of ΔS is plotted in Figure 3.12C when scanning the molecule around the doughnut and Gaussian beam, with $I_G = 0.1I_S$, $I_D = 10I_S$. Compared to the direct-ESSat image, we can see that the modulated-ESSat technique turns the signal

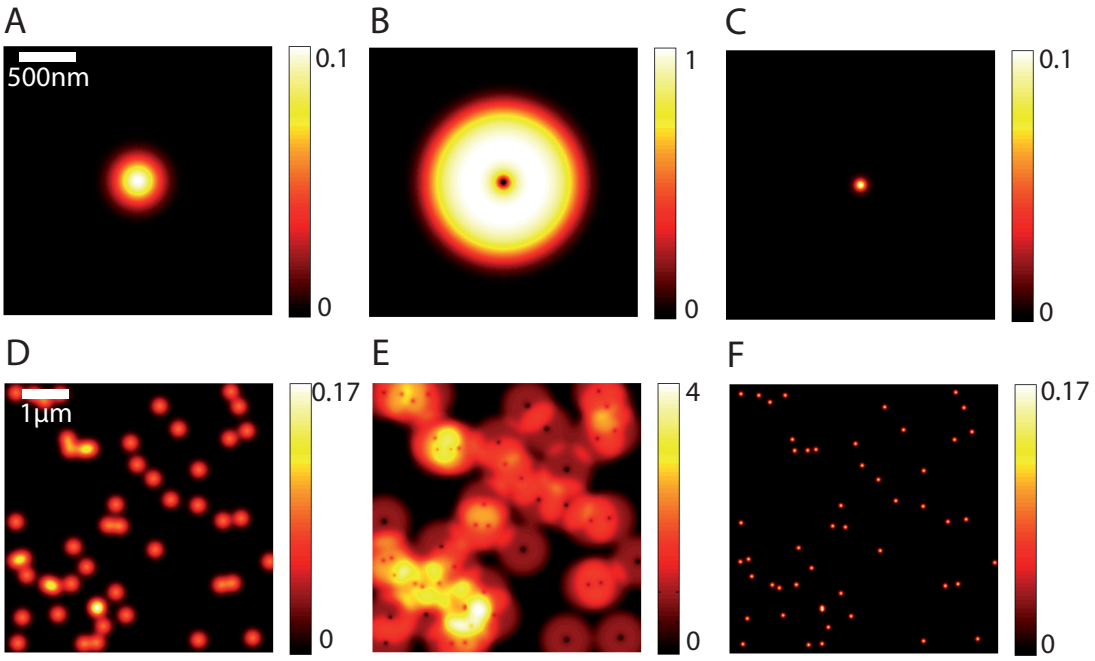

Figure 3.12: Simulations of modulated-ESSat imaging. (A) and (B) represent respectively images of a molecule excited with a Gaussian beam and a doughnut beam; (C) the modulated-ESSat image. (D - F) are images of 50 identical molecules taken with respectively a Gaussian beam, direct-ESSat microscopy and modulated-ESSat microscopy. $I_G = 0.1I_S$, $I_D = 10I_S$. The fluorescence signal is given in the unit of R_∞.

of a single molecule into a "positive" signal on a dark background. We then simulate images of 50 randomly located identical molecules, shown in Figure 3.12D-F. While both direct-ESSat and modulated-ESSat images offer super-resolution, the latter has a better contrast. Indeed, demodulated signals from single molecules do not overlap, as long as molecules are separated by a distance larger than the effective resolution.

We will now discuss the resolution of modulated-ESSat microscopy as a function of intensities of the doughnut and Gaussian beams.

Using Equation 3.5, the amplitude of the fluorescence intensity modulation can be expressed as:

$$\Delta R(r) = R[I_{donut}(r) + I_{Gaussian}(r)] - R[I_{donut}(r)] \tag{3.14}$$

In the following, we consider the case where $r \ll d$. Therefore $I_{Gaussian}(r) \approx I_{Gaussian}(0) = I_G$. In the center of the doughnut beam, the amplitude is maximal and equals to $R(I_G)$.

The resolution can be defined as the FWHM of $\Delta R(r)$ and is given by:

$$\Delta r = \frac{2d}{\pi}\sqrt{\frac{A(I_G)}{I_D/I_S}}, \tag{3.15}$$

with

$$A(I_G) = \sqrt{(1 + I_G/I_S) + (1 + I_G/2I_S)^2} - (1 + I_G/2I_S). \tag{3.16}$$

As in the case of direct-ESSat microscopy, the resolution mainly depends on the inverse of $\sqrt{I_D/I_S}$ and can be drastically reduced when $I_D \gg I_S$. In principle, it also depends on the intensity of the Gaussian beam and is proportional to $\sqrt{A(I_G)}$. The evolution of $\sqrt{A(I_G)}$ is shown in Figure 3.13. At $I_G \gg I_S$, $A(I_G) = 1$ and the resolution of modulated-ESSat microscopy is the same as that of direct-ESSat microscopy. Indeed, in this case, the amplitude of the modulated fluorescence signal is $\Delta R(r) \approx R_\infty - R[I_{donut}(r)]$, with R_∞ the maximal fluorescence signal. Obviously, $\Delta R(r)$ has the same

FWHM as that of $R[I_{donut}(r)]$ (the fluorescence distribution of direct-ESSat). For lower I_G, $\sqrt{A}$ is less than 1. However, the signal-to-noise ratio of modulated-ESSat images will also be lower. Therefore, in practice, I_G is at the order of tens of I_S or even higher and $\sqrt{A} \sim 1$.

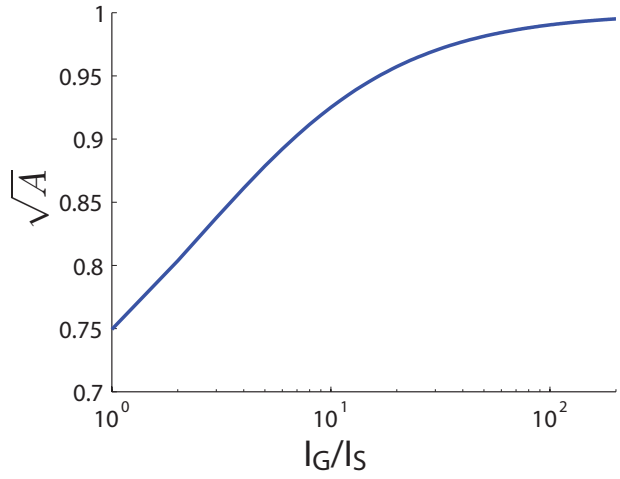

Figure 3.13: $\sqrt{A}$ as a function of I_G/I_S.

3.4 Experimental setup

Sample

The molecule-matrix system used for the present study is the highly fluorescent dibenzanthanthrene (DBATT) molecule (fluorescence yield close to unity) in an octadecane polycrystal. Their structures are shown in Figure 3.14. Single DBATT molecules in octadecane at liquid helium temperature exhibit stable and lifetime-limited zero-phonon lines (FWHM about 30 MHz) around 589nm.

A small drop of a DBATT-doped octadecane solution at temperature about 30 °C is deposited on a coverslip and spread to form a thin film with thickness less than 10 μm. The sample is mounted on a calibrated x-y piezoelectric scanner and x-y-z stepper-

positioners, and inserted together with a microscopic objective (numerical aperture 0.95) in a helium cryostat. The stepper-positioners allow translation of the sample over 4 mm in the lateral direction and over 6 mm in the axial direction. At liquid helium temperature, the scan area is 14 μm * 14 μm.

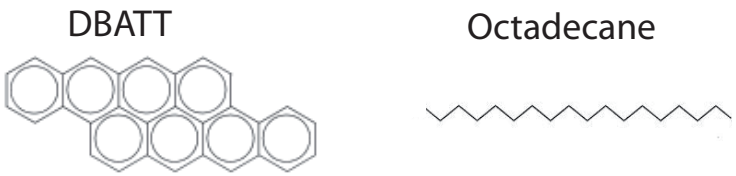

Figure 3.14: Chemical structures of the aromatic DBATT molecule and octadecane.

Optical setup

Figure 3.15A shows a diagram of the direct-ESSat setup. A tunable single-frequency dye laser (Matisse-DS, Sirah) is used to excite DBATT molecules at 589 nm. The spectral resolution of the laser is about 0.5 MHz. The laser output power is stabilized with an electro-optic modulator. A bandpass filter is used to reject the residual fluorescence of the dye. After coupling into a single-mode polarisation-maintaining optical fiber, the laser beam is sent to a spatial light modulator (SLM) (PLUTO-VIS, Holoeye). The SLM has 1920*1080 pixels, and operates in the visible range (400-700 nm). As explained in Chapter 2, the SLM imprints a vortex phase mask varying azimuthally from 0 to 2π and a blazed grating (see Figure 3.16) on the incident light to generate a doughnut beam.

A quarter-wave plate changes the polarisation of the light from linear to circular in order to equally excite the molecules with dipole moment spread in the focal plane. Red-shifted fluorescence from single molecules is filtered and focused on an avalanche photodiode. A pinhole is used to reject the contribution of out-of-focus fluorescence to the counting rate. A flipping mirror can be used to reflect the doughnut beam to a

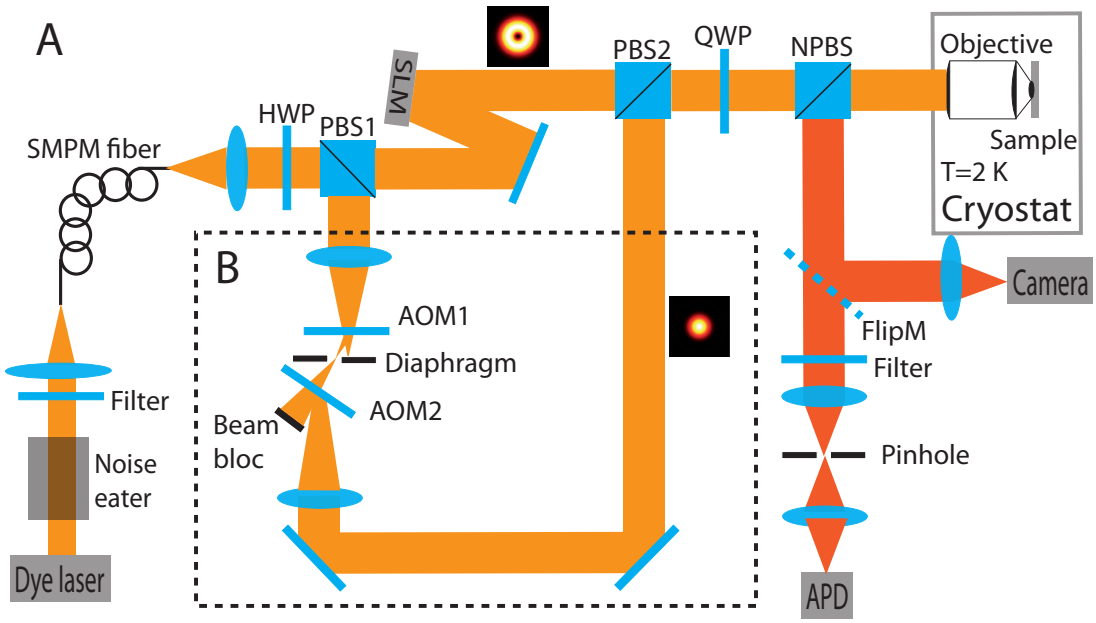

Figure 3.15: Experimental setup of ESSat microscope. (A) Direct-ESSat setup. A dye laser provides excitation light with tunable wavelength around 589 nm. The laser beam is sent to a spatial light modulator (SLM) to produce a doughnut beam at the focal plane of the objective. The fluorescence of single molecules is focused on an avalanche photodiode (APD). (B) Modulation part of the modulated-ESSat setup. The laser beam is split into two beams on a polarizing beamsplitter (PBS1). The transmitted beam is kept to produce the doughnut form. The reflected beam is temporally modulated by two acousto-optical modulators (AOM). Both beams are recombined on PBS2 and focused on the sample. Abbreviations: SMPM Fiber: Single-mode Polarisation-Maintaining Fiber; HWP: Half-Wave Plate; QWP: Quarter-Wave Plate; NPBS : non-polarising cube beamsplitter; FlipM: Flipping Mirror.

camera, in order to characterize its spatial intensity profile.

To perform modulated-ESSat microscopy, a temporally modulated Gaussian beam is superimposed on the doughnut beam, as shown in Figure 3.15B. A polarising beamsplitter (PBS1) splits the laser beam into two beams. The reflected beam is modulated at a frequency of 1 kHz by two AOMs at diffraction orders +1 and -1. The RF frequencies sent to the AOMs differ by 1 MHz, so that beating between the two beams vanishes over the integration time (few ms) of the detector. Moreover, such a small frequency difference between the two beams compared to the molecular linewidth ensures that both beams produce very similar degrees of excitation of the molecule.

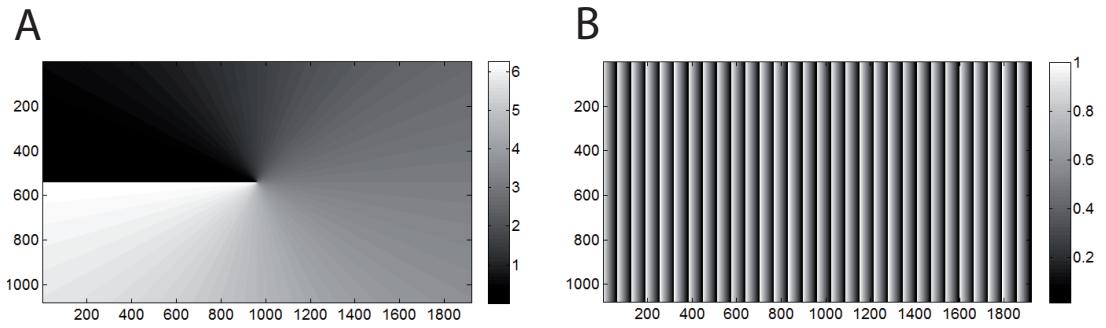

Figure 3.16: Phase masks. (A) Vortex mask with phase varying azimuthally from 0 to 2π; (B) blazed grating.

3.5 Experimental results

3.5.1 Characterization of the doughnut beam

There are different types of optical aberrations in imaging systems [203]. In a confocal microscope, careful alignment of the optical setup assures minimal aberrations and provides diffraction-limited images. However the objective used in this experiment is not designed for cryogenic temperature applications. The optical elements of the objective have different thermal expansion coefficients, which induces aberrations, in particular astigmatism, once cooled down to 2 K. Such aberrations can affect the quality of the

doughnut beam, leading to non-perfect "zero" in the doughnut center and anisotropic intensity distribution.

Optical aberrations can be expressed with Zernike polynomials [203], which are defined on a disk, thus well adapted to describe waves passing through a circular aperture. Figure 3.17 shows the first fifteen wavefront modes for the corresponding Zernike polynomials.

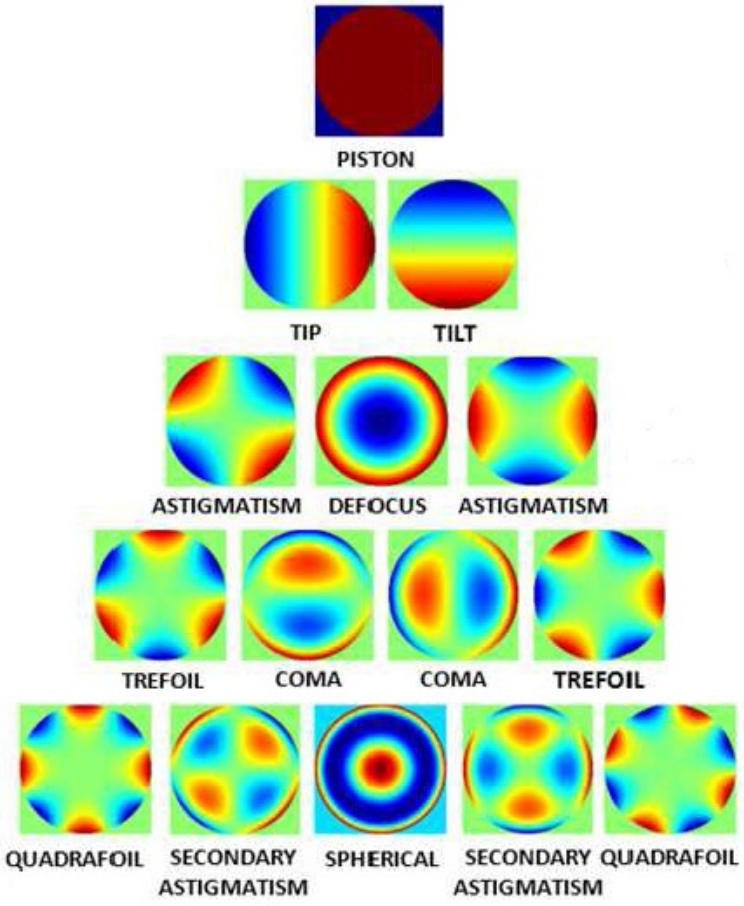

Figure 3.17: Wavefront modes for the first fifteen Zernike polynomials. Extracted from [204].

To correct the aberrations, we apply a compensation phase mask with the SLM, together with the vortex mask and the blazed grating (see Fig 3.16). The compensation

mask is a linear combination of the Zernike polynomials. The first eight Zernike polynomials are used, since they represent the most common aberrations in an imaging system (see Figure 3.17).

We developed an algorithm written in Labview which automatically determines this compensation mask. Figure 3.18 shows the interface of the program.

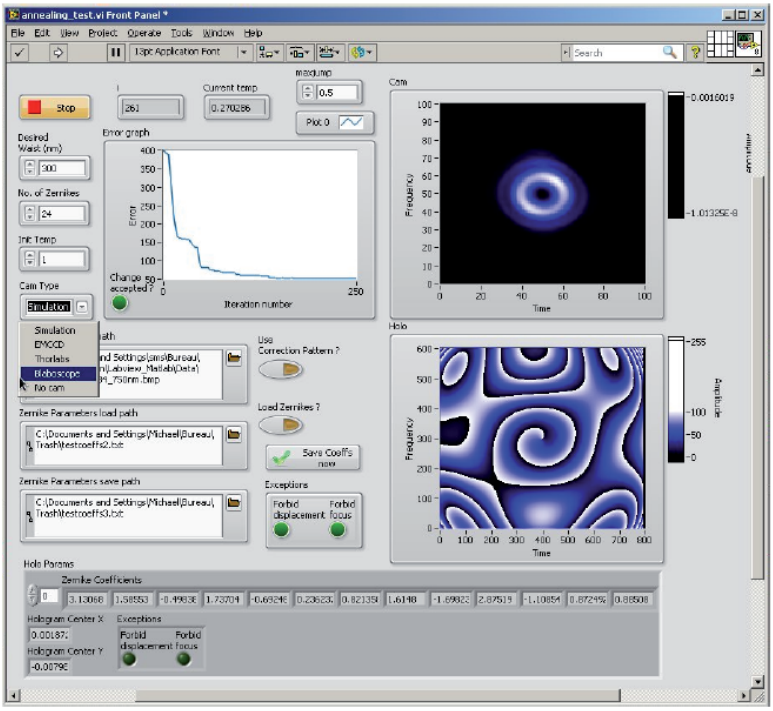

Figure 3.18: Interface of the Labview program for the optimisation of the doughnut beam profile.

An error function is defined as:

$$Err(a_1, a_2, \ldots, a_n) = \sum_{x,y} (I_{exp}(a_1, a_2, \ldots, a_n, x, y) - I_{cal}(x, y))^2 \qquad (3.17)$$

where I_{exp} is the experimental image of the doughnut beam, reflected on a gold mirror placed at the focal plane of the objective. I_{cal} is the corresponding desired diffraction-limited image of the doughnut beam, calculated on the basis of the experimental diameter

of the doughnut beam profile. x, y are the pixel numbers in the image, and a_i is the weight of the ith Zernike polynomial.

The algorithm is based on the simulated annealing method, which minimizes the error function by randomly changing the weight of one of the Zernike polynomials. It combines a direct research by successive tries and a random acceptance of certain "harmful" modifications. A Maxwell-Boltzmann factor is introduced to decide the acceptance of the random changes, allowing to find a better minimum than the closest local minimum. A parameter called *Temperature* appears in the term $exp(-\Delta Err/T)$, where $\Delta Err = Err_1 - Err_0$ is the difference between the error function before and after the change. The *Temperature* evolves with time to ensure a convergence with a reasonable number of iterations and a sufficient exploration of the error function space.

After the launch of the algorithm, the changes of the three Zernike polynomials which represent the x-tilt, y-tilt and focusing actions, decrease the value of the error function rapidly. It points to location and size mismatches between the two images. Thereafter, the changes of the weights for polynomials representing the astigmatisms mostly affect the error function, suggesting that the main existing aberrations in our system are astigmatisms.

Figure 3.19 shows the results of the aberration corrections. Figure 3.19A, B, C are respectively the reflected doughnut image at room temperature, at 2 K before and after aberration corrections. Aberrations that are clearly present at 2 K can be well corrected.

At low temperature, single molecules are both small ($\sim$ 1 nm) and photostable, they can therefore be used as local nanoscopic probe of the light intensity distribution in the focal plane of the objective. The fluorescence signal of a molecule is proportional to the excitation intensity at low saturation. By scanning a molecule across the doughnut beam while recording its fluorescence with an APD, we can reproduce the doughnut intensity profile. Figure 3.20A shows an experimentally obtained fluorescence image of the doughnut beam after the aberration correction, with $I_D = 0.4$ W/cm^2 ($I_S = 2$ W/cm^2),

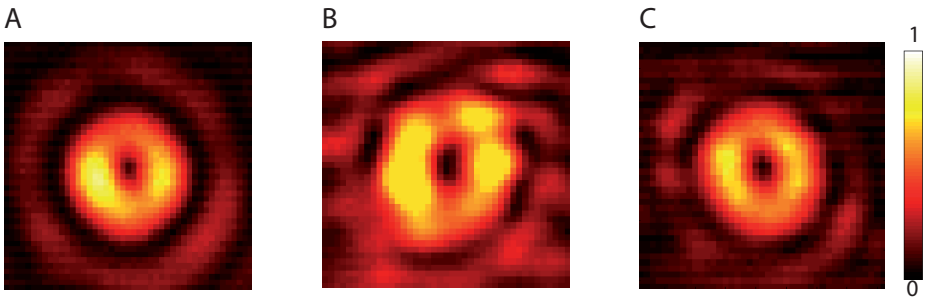

Figure 3.19: Optimizing the doughnut beam with a SLM. Camera images of the doughnut beam, reflected on a gold mirror at the focal plane of the objective, at room temperature (A), at 2 K without aberration correction (B) and at 2 K with aberration correction (C).

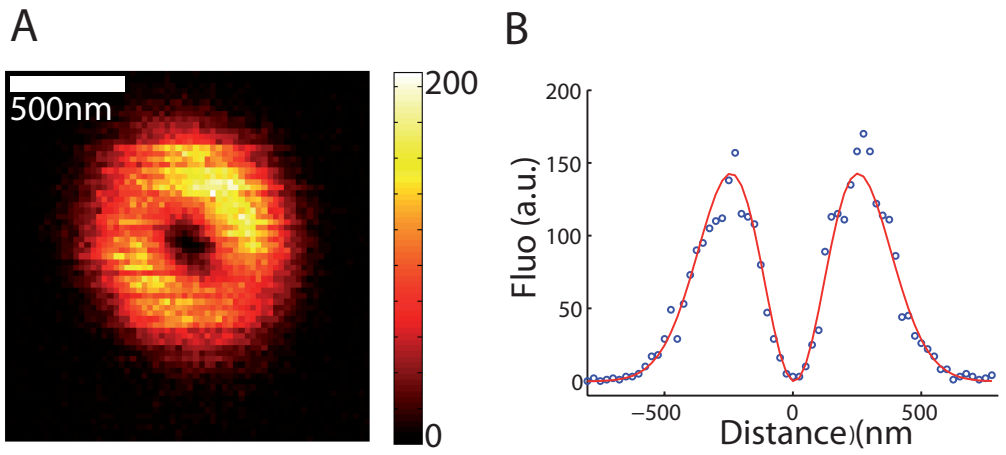

Figure 3.20: (A) Fluorescence image of a molecule excited with the doughnut beam. Pixel dwell time is 10 ms and $I_D = 0.4$ W/cm^2. (B) Cross-sectional profile.

$a_3 = 2\lambda$ and $a_5 = 1\lambda$ (both for astigmatism corrections). In this case, the aberrations shown in the doughnut image are induced once by the objective. The parameters of the Zernike polynomials are divided by two with respect to these determined with the reflection image, in which the aberrations are induced twice by the objective.

A very important issue regarding the doughnut intensity distribution is the intensity in its center, where residual intensity will degrade the resolution performance of ESSat microscopy. The cross-sectional profile in Figure 3.20B shows that the fluorescence intensity at the center of the doughnut profile, due to background signal, is less than 1% of the peak intensity.

3.5.2 Results of direct-excited state saturation microscopy

Confocal or direct-ESSat images of a single molecule are displayed in Figure 3.21A. The central dip of the direct-ESSat images of the molecule sharpens while increasing the excitation intensity. The FWHM of the central dips as a function of the laser intensity is shown Figure 3.21B. The black spots are the experimental data, fitted with Equation 3.9. The extracted saturation intensity I_S is 1.3 W/cm^2.

Figure 3.22 shows the image of another molecule and its profile for $I_D = 13$ kW/cm^2, which corresponds to about 10^4 I_S. The lowest value of the fluorescence intensity in the image is about 0.4 of the maximal value, due to the residual intensity in the doughnut center. The residual intensity can be therefore deduced with Equation 3.5 to be about $6{\cdot}10^{-5}$ of the maximal intensity. The achieved resolution is 4.4 nm, close to the value 3.9 nm predicted by Equation 3.10. This resolution is less than a hundredth of the laser wavelength (589 nm) and approaches the size of the molecule. In principle, applying higher laser intensities can further improve the resolution. However, we observed displacements of the minimal fluorescence signal between successive scanning lines in images acquired at higher laser intensities. This suggests that the resolution is currently limited by the mechanical stability of our microscope setup. Two factors have been identified.

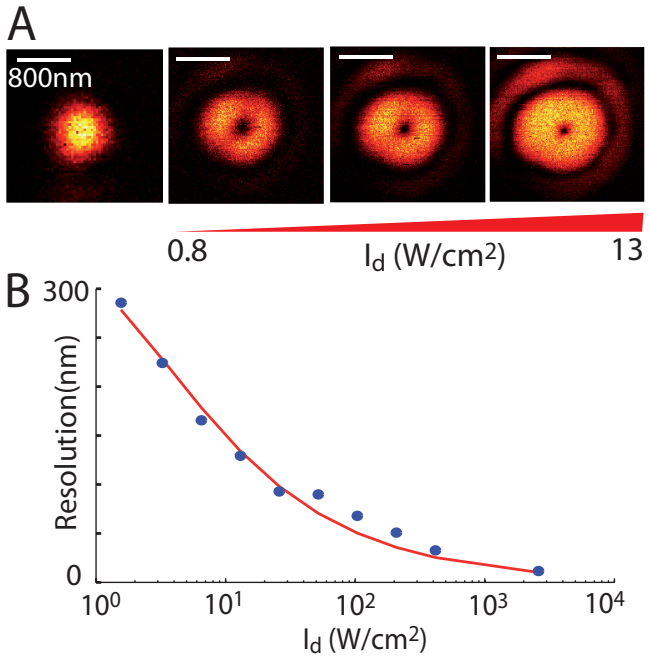

Figure 3.21: Experimental resolution obtained with direct-ESSat microscopy. (A) Images of a molecule obtained with a Gaussian beam or with a doughnut beam for different laser intensities. (B) Resolution of direct-ESSat microscopy as a function of the doughnut beam intensity. The rightmost spot corresponds to 11.5 nm resolution with $I_d = 1.3kW/cm^2$. Black spot: experimental data; red line: fit by Equation 3.9.

The first one is the mechanical vibration of the microscopy insert. The microscopy insert is about 60 cm long. It is inserted in the cryostat and fixed at the top. The fixation at the bottom is realized by three springs around the insert, which might not provide sufficient mechanical stability for nm-resolution imaging. We will try different fixation designs of the insert in order to improve its mechanical stability. The second one is the hysteresis of our open-loop piezoelectric scanner. Using a closed-loop piezo scanner or an external scanning mirror can further improve the mechanical stability of our ESSat microscope.

A direct-ESSat image of two molecules separated by about 300 nm (below the diffraction limit 380 nm) is shown in Figure 3.23. The fluorescence excitation spectrum confirms the presence of two molecules with optical resonances separated by about 150 MHz. The

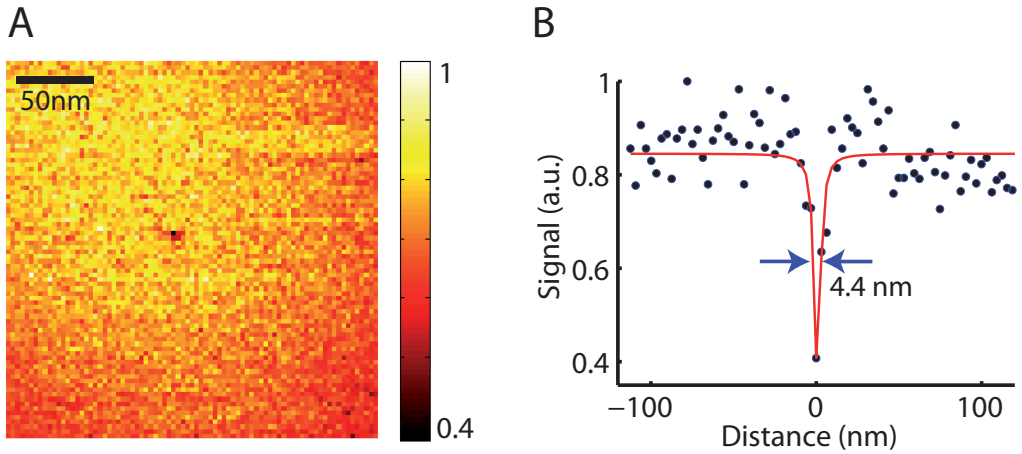

Figure 3.22: Direct-ESSat imaging of a single molecule. (A) Central region of the image of a molecule; (B) profile of the left image. $I_D = 13$ kW/cm^2.

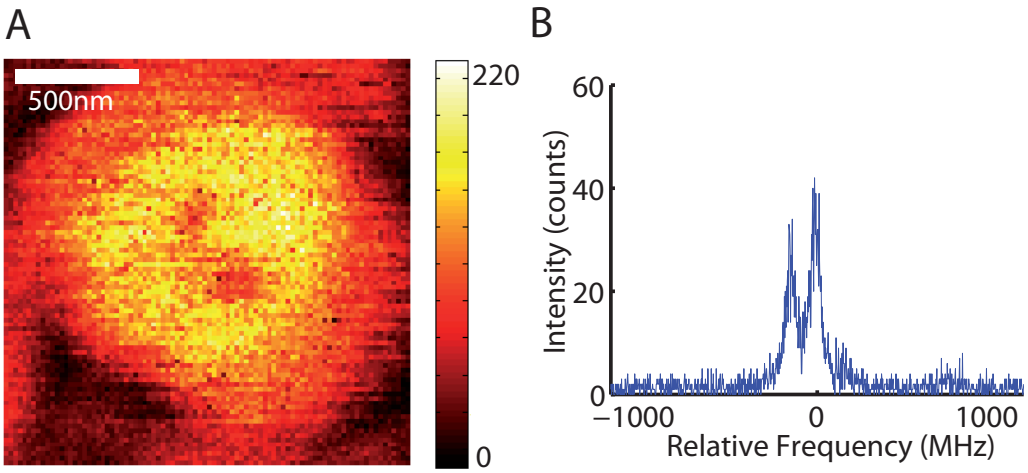

Figure 3.23: Direct-ESSat imaging of two molecules ($I_D = 130$ W/cm^2) and their fluorescence excitation spectrum ($I_D = 0.5$ W/cm^2). Pixel dwell time is 5 ms.

laser was tuned to a frequency for which the molecular lines have a maximal overlap. The two molecules can be clearly resolved, with well separated local fluorescence minima. However, the contrast of the image is poor since the saturated fluorescence signal of each molecule adds to the fluorescence minimum of the other one. In order to improve the image contrast, modulated-ESSat microscopy is performed and presented in the next section.

3.5.3 Results of modulated-excited state saturation microscopy

In all modulated-ESSat experiments, the Gaussian beam is modulated at the frequency of 1 kHz, 500 μs "on" and 500 μs "off". Figure 3.24 displays a diffraction-limited Gaussian image, a direct-ESSat image and a modulated-ESSat image of the same molecule. The modulated-ESSat method yields a super-resolved image of the molecule with a "positive" signal over a dark background. Yet a residual noise is still present in Figure 3.24C. It is due to fluorescence shot noise in the doughnut-shaped saturated fluorescence intensity, which leads to noise in the demodulated signal. In order to improve the signal-to-noise ratio of the modulated-ESSat image, a longer acquisition time is required.

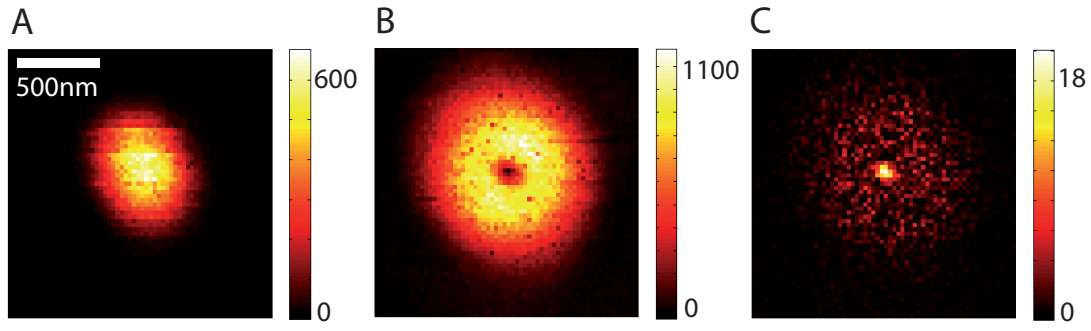

Figure 3.24: Modulated-ESSat imaging. (A) and (B) represent respectively images of a molecule obtained with the Gaussian beam (I_G = 0.7 W/cm^2) and with the doughnut beam (I_D = 26 W/cm^2); (C) the modulated-ESSat image. I_G = 5 W/cm^2, I_D = 26 W/cm^2, pixel dwell time 10 ms, modulation frequency 1 kHZ.

The resolution of modulated-ESSat is investigated as a function of the doughnut

beam intensities, shown in Figure 3.25. As in direct-ESSat microscopy, the resolution is improved with increasing doughnut beam intensities.

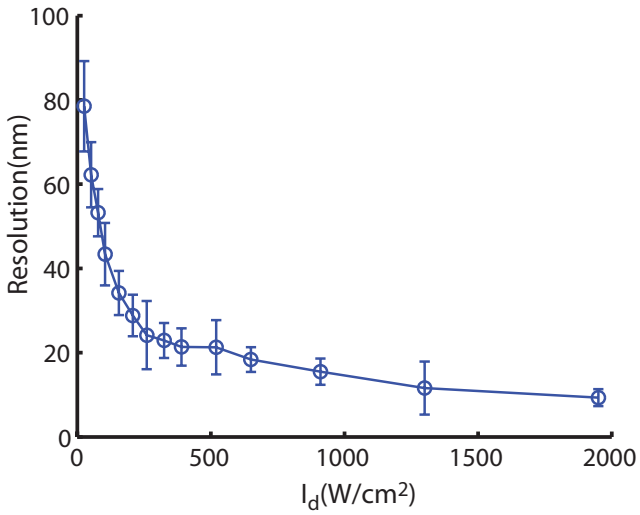

Figure 3.25: Evolution of the resolution as a function of I_D. I_G is fixed at 15 W/cm^2. I_S = 1.4 W/cm^2. Each displayed data is an average of three measurements, and the error bar shows the standard deviation.

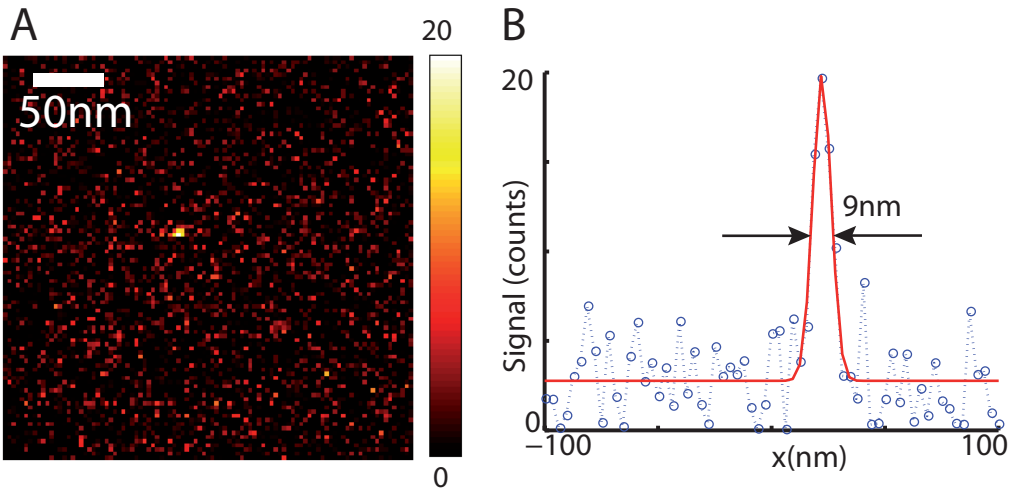

Figure 3.26: Modulated-ESSat imaging of a molecule. (A) Modulated-ESSat image; (B) the intensity profile of the molecule and the Gaussian fit used to determine the FWHM. Pixel size 3nm, pixel dwell time 25ms. I_D = 2.2 kW/cm^2 and I_G = 170 W/cm^2.

At $I_D = 2.2$ kW/cm^2 and $I_G = 170$ W/cm^2, we achieve a resolution of 9 nm, as shown in Figure 3.26. The acquisition time of modulated-ESSat is longer than that of direct-ESSat, which makes modulated-ESSat images more prone to mechanical vibrations. Therefore we could not achieve the same resolution as that obtained with direct-ESSat.

Figure 3.27A shows the fluorescence excitation spectrum of two molecules. We tune the laser frequency to the frequency of maximal overlap of the two molecular lines and acquire a conventional confocal image of the two molecules, shown in Figure 3.27B. The images of the two molecules overlap and they are not resolved. Modulated-ESSat clearly resolves the fluorescence spots from the two molecules, and unravels a spatial separation of 200 nm between them, as shown in Figure 3.27C.

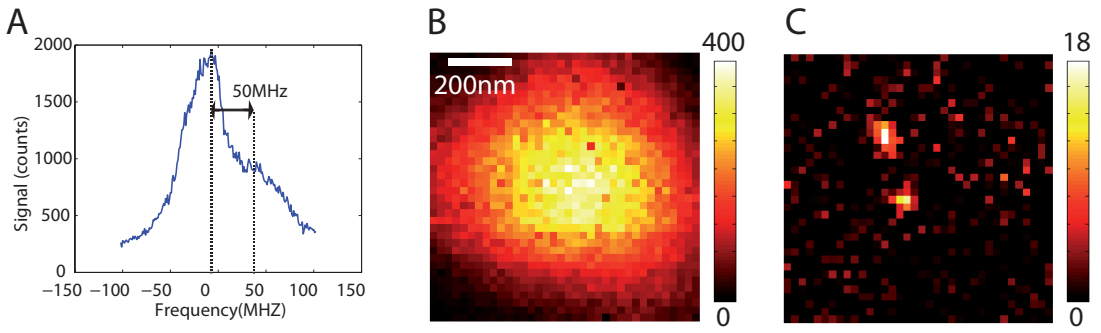

Figure 3.27: Superresolution imaging of two molecules with modulated-ESSat microscopy. (A) Fluorescence excitation spectrum of the two molecules at T = 2 K, I_G = 1.5 W/cm^2; (B) confocal image, $I_G = 5$ W/cm^2, pixel dwell time 4 ms; (C) modulated-ESSat image, $I_G = 100$ W/cm^2, $I_D = 260$ W/cm^2, pixel dwell time 25 ms. Pixel size 25 nm. Pixel value in the unit of APD counts.

3.6 Conclusion

In this chapter, we presented a new super-resolution imaging method of single molecules at cryogenic temperature, based on excited state saturation with a doughnut beam. A resolution of 4.4 nm was achieved with this method, approaching the size of the molecule. Due to extremely low saturation intensity of single molecules at liquid helium

temperature, this resolution is obtained with a laser intensity of only a few tens of kW/cm^2. Application of a modulated Gaussian beam together with a demodulation technique offers a better contrast in images of highly concentrated samples. A resolution of 9 nm was obtained with this method, due to longer integration times over which mechanical vibrations of the cryostat are integrated. The resolution of ESSat microscopy is limited by the residual intensity in the center of the doughnut beam, the mechanical stabilities of the cryostat and of the piezo scanner, which could be improved with future developments. ESSat microscopy is capable of sub-diffraction imaging of molecules with close optical resonance, which offers the possibilities to pursue different quantum optics applications, such as the entanglements and interactions between molecules by coherent dipole-dipole coupling [193].

Summary and outlook

During the course of this Doctorate work, we developed two super-resolution microscopies: Lattice-STED microscopy and cryogenic ESS microscopy.

Lattice-STED for the first time massively parallelized STED microscopy. Optical lattices generated by multi-beam interferences are used as depletion patterns together with a camera for detection. In order to obtain a super-resolution image, the sample only needs to be scanned over a unit cell of the optical lattice instead of the whole field of view. A 100-fold parallelization was achieved with moderate laser powers. Super-resolution images of 70 nm resolution and a field view of 2.9 μm * 2.9 μm can be acquired at a rate of 12.5 images per second. This imaging speed is only limited by the readout time of the camera and can be therefore improved by using faster cameras.

The resolution performances of Lattice-STED is related to the rotational mobility of the molecules. For slowly-rotating or fixed molecules, the polarization of the field of the optical lattice matters. For three-beam Lattice-STED , the effective fluorescence PSF does not depend on the relative phases of the three beams, therefore the super-resolution images can be deconvolved with this PSF. For four-beam Lattice-STED, one can use circularly polarized beams combined with light-sheet microscopy [205, 206], so as to deplete equally molecules with dipole moment spread in the focal plane of the objective.

The imaging speed of Lattice-STED is currently limited by the readout time of the camera. With the development of new camera techniques, for example the APD-array camera, the imaging speed of Lattice-STED could be further improved, to $\sim$ 1000 frames

per second.

Increasing the field of view of Lattice-STED is another interesting challenge. Lasers with lower repetition rate can deplete molecules more efficiently [207]; nanoparticle-assisted STED [208] uses metal nanoparticles to enhance both the excitation light and the fluorescence of the emitters. They all allow STED imaging with lower light level, thus can be implemented with Lattice-STED to achieve bigger fields of view.

Another possibility is to use reversible photoswitchable fluorescent proteins, which require low light level to be switched. Chmyrov et al. parallelized RESOLFT microscopy based on photoswitchable proteins and achieved a field of view of about 100 μm * 100 μm with an imaging speed of several second per super-resolution images [209]. However, protein switching is a relatively slow on-off process ($\sim$ 10 ms), which sets a limit to the imaging acquisition rate. Therefore, Lattice-STED and parallelized-RESOLFT can be regarded as complementary techniques: the first one offers higher imaging speed and the second one provides larger fields of view. We will combine the two techniques to pursue biological applications such as the study of fast cell shaping and migration.

ESSat microscopy is based on the optical saturation of the sharp zero-phonon line of single molecules inserted in solid hosts at 2K. By imaging molecules with a doughnut-shaped beam, we demonstrated a resolution of 4.4 nm. Due to the extremely low saturation intensities of the zero-phonon line, this resolution is obtained with a laser intensity of only 13 kW/cm^2. Application of a modulated Gaussian beam together with a demodulation technique offers a better contrast in images of highly concentrated samples. A resolution of 9 nm was obtained with this method, due to longer integration times over which mechanical vibrations of the cryostat are integrated.

Besides ESSat microscopy, one can also consider the implementation of STED microscopy at cryogenic temperature. STED microscopy at room temperature has demonstrated a resolution of 8 nm with single N-V centers in diamond with an oil-immersion objective [93], then a 4.2 nm resolution with a solid immersion objective [94]. However, it

requires high laser intensity (up to several GW/cm^2), which is about 10^5-10^6 times higher than the intensity applied in ESSat microscopy. Applying STED microscopy to single molecules at liquid helium temperature could reduce the required depletion intensity by three orders of magnitude. Since STED microscopy does not require the modulation of the Gaussian beam as in modulated-ESSat microscopy, pixel dwell times as short as several tens of μs are possible [47]. Such short integration times are interesting to reduce the effects of mechanical vibrations during imaging.

Further improvement of the super-resolution microscopy at cryogenic temperature could be three-dimensional resolution enhancement. 3D super-resolution is crucial to determine the distance between single emitters in a thick sample. Studying spectrally and spatially close molecules offers the possibilities to pursue different quantum optics applications, such as the entanglements and interactions between molecules by coherent dipole-dipole coupling [193].

Bibliography

[1] M. E. Verdet, *Leçons d'optique physique* (Masson, 1869).

[2] E. Abbe, "Beiträge zur theorie des mikroskops und der mikroskopischen wahrnehmung", *Archiv für mikroskopische Anatomie* **9**, 413 (1873).

[3] Rayleigh, "On the theory of optical images, with special reference to the microscope", *Philosophical Magazine Series 5* **42**, 167 (1896).

[4] J. I. Goldstein, D. E. Newbury, P. Echlin, D. C. Joy, C. Fiori, and E. Lifshin, "Scanning electron microscopy and X-ray microanalysis. A text for biologists, materials scientists, and geologists", 673 pp. (1981).

[5] W. Chao, B. D. Harteneck, J. A. Liddle, E. H. Anderson, and D. T. Attwood, "Soft X-ray microscopy at a spatial resolution better than 15 nm", *Nature* **435**, 1210 (2005).

[6] J. Vila-Comamala, K. Jefimovs, J. Raabe, T. Pilvi, R. H. Fink, M. Senoner, A. Maassdorf, M. Ritala, and C. David, "Advanced thin film technology for ultrahigh resolution X-ray microscopy", *Ultramicroscopy* **109**, 1360 (2009).

[7] W. Chao, P. Fischer, T. Tyliszczak, S. Rekawa, E. Anderson, and P. Naulleau, "Real space soft x-ray imaging at 10 nm spatial resolution", *Optics Express* **20**, 9777 (2012).

[8] R. Erni, M. D. Rossell, C. Kisielowski, and U. Dahmen, "Atomic-resolution imaging with a sub-50-pm electron probe", *Physical Review Letters* **102**, 096101 (2009).

[9] D. B. Williams and C. B. Carter, *Transmission Electron Microscopy* (Springer US, 1996), pp. 3–17.

[10] M. L. Watson, "Staining of tissue sections for electron microscopy with heavy metals", *The Journal of Biophysical and Biochemical Cytology* **4**, 475 (1958).

[11] G. E. Palade, "A study of fixation for electron microscopy", *The Journal of Experimental Medicine* **95**, 285 (1952).

[12] B. Hecht, B. Sick, U. P. Wild, V. Deckert, R. Zenobi, O. J. F. Martin, and D. W. Pohl, "Scanning near-field optical microscopy with aperture probes: Fundamentals and applications", *The Journal of Chemical Physics* **112**, 7761 (2000).

[13] E. Betzig and R. J. Chichester, "Single molecules observed by near-field scanning optical microscopy", *Science* **262**, 1422 (1993).

[14] G. Binnig, C. F. Quate, and C. Gerber, "Atomic force microscope", *Physical Review Letters* **56**, 930 (1986).

[15] Q. Zhong, D. Inniss, K. Kjoller, and V. B. Elings, "Fractured polymer/silica fiber surface studied by tapping mode atomic force microscopy", *Surface Science Letters* **290**, L688 (1993).

[16] G. Meyer and N. M. Amer, "Novel optical approach to atomic force microscopy", *Applied Physics Letters* **53**, 1045 (1988).

[17] F. J. Giessibl, "Advances in atomic force microscopy", *Reviews of Modern Physics* **75**, 949 (2003).

[18] P. K. Hansma and J. Tersoff, "Scanning tunneling microscopy", *Journal of Applied Physics* **61**, R1 (1987).

[19] J. Tersoff and D. R. Hamann, "Theory of the scanning tunneling microscope", *Physical Review B* **31**, 805 (1985).

[20] D. M. Eigler and E. K. Schweizer, "Positioning single atoms with a scanning tunnelling microscope", *Nature* **344**, 524 (1990).

[21] F. Ohnesorge and G. Binnig, "True atomic resolution by atomic force microscopy through repulsive and attractive forces", *Science* **260**, 1451 (1993).

[22] F. J. Giessibl, "Atomic resolution of the silicon (111)-(7x7) surface by atomic force microscopy", *Science* **267**, 68 (1995).

[23] J. W. Lichtman and J.-A. Conchello, "Fluorescence microscopy", *Nature Methods* **2**, 910 (2005).

[24] M. Orrit and J. Bernard, "Single pentacene molecules detected by fluorescence excitation in a p-terphenyl crystal", *Physical Review Letters* **65**, 2716 (1990).

[25] W. P. Ambrose, T. Basché, and W. E. Moerner, "Detection and spectroscopy of single pentacene molecules in a p-terphenyl crystal by means of fluorescence excitation", *The Journal of Chemical Physics* **95**, 7150 (1991).

[26] J. Mertz, *Introduction to optical microscopy* (Roberts, 2010).

[27] A. G. Godin, B. Lounis, and L. Cognet, "Super-resolution microscopy approaches for live cell imaging", *Biophysical Journal* **107**, 1777 (2014).

[28] E. Betzig, G. H. Patterson, R. Sougrat, O. W. Lindwasser, S. Olenych, J. S. Bonifacino, M. W. Davidson, J. Lippincott-Schwartz, and H. F. Hess, "Imaging intracellular fluorescent proteins at nanometer resolution", *Science* **313**, 1642 (2006).

[29] S. T. Hess, T. P. Girirajan, and M. D. Mason, "Ultra-high resolution imaging by fluorescence photoactivation localization microscopy", *Biophysical Journal* **91**, 4258 (2006).

[30] M. J. Rust, M. Bates, and X. Zhuang, "Sub-diffraction-limit imaging by stochastic optical reconstruction microscopy STORM", *Nature Methods* **3**, 793 (2006).

[31] M. Heilemann, S. vandeLinde, M. Schüttpelz, R. Kasper, B. Seefeldt, A. Mukherjee, P. Tinnefeld, and M. Sauer, "Subdiffraction-resolution fluorescence imaging with conventional fluorescent probes", *Angewandte Chemie International Edition* **47**, 6172 (2008).

[32] A. Sharonov and R. M. Hochstrasser, "Wide-field subdiffraction imaging by accumulated binding of diffusing probes", *Proceedings of the National Academy of Sciences* **103**, 18911 (2006).

[33] G. Giannone, E. Hosy, F. Levet, A. Constals, K. Schulze, A. I. Sobolevsky, M. P. Rosconi, E. Gouaux, R. Tampé, D. Choquet, and L. Cognet, "Dynamic superresolution imaging of endogenous proteins on living cells at ultra-high density", *Biophysical Journal* **99**, 1303 (2010).

[34] S. W. Hell and J. Wichmann, "Breaking the diffraction resolution limit by stimulated emission: stimulated-emission-depletion fluorescence microscopy", *Optics Letters* **19**, 780 (1994).

[35] S. W. Hell and M. Kroug, "Ground-state-depletion fluorscence microscopy: A concept for breaking the diffraction resolution limit", *Applied Physics B* **60**, 495 (1995).

[36] M. G. L. Gustafsson, "Surpassing the lateral resolution limit by a factor of two using structured illumination microscopy", *Journal of Microscopy, Journal of Microscopy* **198, 198**, 82, 82 (2000).

[37] R. Heintzmann, T. M. Jovin, and C. Cremer, "Saturated patterned excitation microscopy—a concept for optical resolution improvement", *Journal of the Optical Society of America A* **19**, 1599 (2002).

[38] M. G. L. Gustafsson, "Nonlinear structured-illumination microscopy: wide-field fluorescence imaging with theoretically unlimited resolution", *Proceedings of the National Academy of Sciences of the United States of America* **102**, 13081 (2005).

[39] The Nobel Prize in Chemistry 2014 - press release, `http://www.nobelprize.org/nobel_prizes/chemistry/laureates/2014/press.html`, accessed: 2015-01-20.

[40] L. Zhu, W. Zhang, D. Elnatan, and B. Huang, "Faster STORM using compressed sensing", *Nature Methods* **9**, 721 (2012).

[41] T. Grotjohann, I. Testa, M. Reuss, T. Brakemann, C. Eggeling, S. W. Hell, and S. Jakobs, "rsEGFP2 enables fast RESOLFT nanoscopy of living cells", *eLife* **1**, (2012).

[42] F. Huang, T. M. P. Hartwich, F. E. Rivera-Molina, Y. Lin, W. C. Duim, J. J. Long, P. D. Uchil, J. R. Myers, M. A. Baird, W. Mothes, M. W. Davidson, D. Toomre, and J. Bewersdorf, "Video-rate nanoscopy using sCMOS camera-specific single-molecule localization algorithms", *Nature Methods* **10**, 653 (2013).

[43] H.-l. D. Lee, S. J. Sahl, M. D. Lew, and W. E. Moerner, "The double-helix microscope super-resolves extended biological structures by localizing single blinking molecules in three dimensions with nanoscale precision", *Applied Physics Letters* **100**, 153701 (2012).

[44] S. A. Jones, S.-H. Shim, J. He, and X. Zhuang, "Fast, three-dimensional super-resolution imaging of live cells", *Nature Methods* **8**, 499 (2011).

[45] T. J. Gould, D. Burke, J. Bewersdorf, and M. J. Booth, "Adaptive optics enables 3D STED microscopy in aberrating specimens", *Optics Express* **20**, 20998 (2012).

[46] N. T. Urban, K. I. Willig, S. W. Hell, and U. V. Nagerl, "STED nanoscopy of actin dynamics in synapses deep inside living brain slices", *Biophysical Journal* **101**, 1277 (2011).

[47] V. Westphal, S. O. Rizzoli, M. A. Lauterbach, D. Kamin, R. Jahn, and S. W. Hell, "Video-rate far-field optical nanoscopy dissects synaptic vesicle movement", *Science* **320**, 246 (2008).

[48] U. V. Nagerl, K. I. Willig, B. Hein, S. W. Hell, and T. Bonhoeffer, "Live-cell imaging of dendritic spines by STED microscopy", *Proceedings of the National Academy of Sciences of the United States of America* **105**, 18982 (2008).

[49] J.-B. Trebbia, P. Tamarat, and B. Lounis, "Indistinguishable near-infrared single photons from an individual organic molecule", *Physical Review A* **82**, 063803 (2010).

[50] R. Lettow, Y. L. A. Rezus, A. Renn, G. Zumofen, E. Ikonen, S. Götzinger, and V. Sandoghdar, "Quantum interference of tunably indistinguishable photons from remote organic molecules", *Physical Review Letters* **104**, 123605 (2010).

[51] G. V. Varada and G. S. Agarwal, "Two-photon resonance induced by the dipole-dipole interaction", *Physical Review A* **45**, 6721 (1992).

[52] M. C. Raff, "Two distinct populations of peripheral lymphocytes in mice distinguishable by immunofluorescence", *Immunology* **19**, 637 (1970).

[53] W. W. Franke, E. Schmid, M. Osborn, and K. Weber, "Different intermediate-sized filaments distinguished by immunofluorescence microscopy", *Proceedings of the National Academy of Sciences* **75**, 5034 (1978).

[54] B. A. Griffin, S. R. Adams, and R. Y. Tsien, "Specific covalent labeling of recombinant protein molecules inside live cells", *Science* **281**, 269 (1998).

[55] A. Keppler, S. Gendreizig, T. Gronemeyer, H. Pick, H. Vogel, and K. Johnsson, "A general method for the covalent labeling of fusion proteins with small molecules in vivo", *Nature Biotechnology* **21**, 86 (2003).

[56] G. V. Los, L. P. Encell, M. G. McDougall, D. D. Hartzell, N. Karassina, C. Zimprich, M. G. Wood, R. Learish, R. F. Ohana, M. Urh, D. Simpson, J. Mendez, K. Zimmerman, P. Otto, G. Vidugiris, J. Zhu, A. Darzins, D. H. Klaubert, R. F. Bulleit, and K. V. Wood, "HaloTag: a novel protein labeling technology for cell imaging and protein analysis", *ACS Chemical Biology* **3**, 373 (2008).

[57] J. Lippincott-Schwartz and G. H. Patterson, "Development and use of fluorescent protein markers in living cells", *Science* **300**, 87 (2003).

[58] V. V. Verkhusha and K. A. Lukyanov, "The molecular properties and applications of Anthozoa fluorescent proteins and chromoproteins", *Nature Biotechnology* **22**, 289 (2004).

[59] R. Y. Tsien, "The green fluorescent protein", *Annual Review of Biochemistry* **67**, 509 (1998).

[60] M. Chalfie, Y. Tu, G. Euskirchen, W. W. Ward, and D. C. Prasher, "Green fluorescent protein as a marker for gene expression", *Science* **263**, 802 (1994).

[61] M. Minsky, "Memoir on inventing the confocal scanning microscope", *Scanning* **10**, 128 (1988).

[62] J.-A. Conchello and J. W. Lichtman, "Optical sectioning microscopy", *Nature Methods* **2**, 920 (2005).

[63] T. H. Maiman, "Stimulated optical radiation in ruby", *Nature* **187**, 493 (1960).

[64] L. Dudás, J. Sinkó, M. Erdélyi, and G. Szabó, "Confocal line-scanning microscope with modified illumination", *Optics Letters* **37**, 4293 (2012).

[65] B. Zhang, J. Zerubia, and J.-C. Olivo-Marin, "Gaussian approximations of fluorescence microscope point-spread function models", *Applied Optics* **46**, 1819 (2007).

[66] W. Denk, J. Strickler, and W. Webb, "Two-photon laser scanning fluorescence microscopy", *Science* **248**, 73 (1990).

[67] F. Helmchen and W. Denk, "Deep tissue two-photon microscopy", *Nature Methods* **2**, 932 (2005).

[68] K. Svoboda, W. Denk, D. Kleinfeld, and D. W. Tank, "In vivo dendritic calcium dynamics in neocortical pyramidal neurons", *Nature* **385**, 161 (1997).

[69] D. Kleinfeld, P. P. Mitra, F. Helmchen, and W. Denk, "Fluctuations and stimulus-induced changes in blood flow observed in individual capillaries in layers 2 through 4 of rat neocortex", *Proceedings of the National Academy of Sciences* **95**, 15741 (1998).

[70] F. Helmchen, K. Svoboda, W. Denk, and D. W. Tank, "In vivo dendritic calcium dynamics in deep-layer cortical pyramidal neurons", *Nature Neuroscience* **2**, 989 (1999).

[71] P. Theer and W. Denk, "On the fundamental imaging-depth limit in two-photon microscopy", *Journal of the Optical Society of America A* **23**, 3139 (2006).

[72] W. L. Peticolas, J. P. Goldsborough, and K. E. Rieckhoff, "Double photon excitation in organic crystals", *Physical Review Letters* **10**, 43 (1963).

[73] O. Svelto, *Principles of lasers* (Springer Science & Business Media, 2010).

[74] E. J. Ambrose, "A surface contact microscope for the study of cell movements", *Nature* **178**, 1194 (1956).

[75] D. Axelrod, "Cell-substrate contacts illuminated by total internal reflection fluorescence.", *The Journal of Cell Biology* **89**, 141 (1981).

[76] E. J. Ezratty, M. A. Partridge, and G. G. Gundersen, "Microtubule-induced focal adhesion disassembly is mediated by dynamin and focal adhesion kinase", *Nature Cell Biology* **7**, 581 (2005).

[77] M. C. Leake, J. H. Chandler, G. H. Wadhams, F. Bai, R. M. Berry, and J. P. Armitage, "Stoichiometry and turnover in single, functioning membrane protein complexes", *Nature* **443**, 355 (2006).

[78] S. Hell and E. H. K. Stelzer, "Properties of a 4Pi confocal fluorescence microscope", *Journal of the Optical Society of America A* **9**, 2159 (1992).

[79] S. Hell and E. H. K. Stelzer, "Fundamental improvement of resolution with a 4Pi-confocal fluorescence microscope using two-photon excitation", *Optics Communications* **93**, 277 (1992).

[80] M. G. L. Gustafsson, D. A. Agard, and J. W. Sedat, in *Sevenfold improvement of axial resolution in 3D wide-field microscopy using two objective lenses* (PUBLISHER, 1995), Vol. 2412, pp. 147–156.

[81] M. G. Gustafsson, D. A. Agard, and J. W. Sedat, "I5M: 3D widefield light microscopy with better than 100 nm axial resolution", *Journal of microscopy* **195**, 10 (1999).

[82] S. W. Hell, "Toward fluorescence nanoscopy", *Nature Biotechnology* **21**, 1347 (2003).

[83] S. W. Hell, "Far-field optical nanoscopy", *Science* **316**, 1153 (2007).

[84] B. Huang, M. Bates, and X. Zhuang, "Super resolution fluorescence microscopy", *Annual review of biochemistry* **78**, 993 (2009).

[85] N. A. Jensen, J. G. Danzl, K. I. Willig, F. Lavoie-Cardinal, T. Brakemann, S. W. Hell, and S. Jakobs, "Coordinate-targeted and coordinate-stochastic super-resolution microscopy with the reversibly switchable fluorescent rrotein dreiklang", *ChemPhysChem* n/a (2014).

[86] T. A. Klar and S. W. Hell, "Subdiffraction resolution in far-field fluorescence microscopy", *Optics Letters* **24**, 954 (1999).

[87] D. H. Burns, J. B. Callis, G. D. Christian, and E. R. Davidson, "Strategies for attaining superresolution using spectroscopic data as constraints", *Applied Optics* **24**, 154 (1985).

[88] A. M. van Oijen, J. Köhler, J. Schmidt, M. Müller, and G. J. Brakenhoff, "3-Dimensional super-resolution by spectrally selective imaging", *Chemical Physics Letters* **292**, 183 (1998).

[89] M. P. Clausen, S. Galiani, D. L. Serna, J. Bernardino, M. Fritzsche, J. Chojnacki, K. Gehmlich, B. C. Lagerholm, and C. Eggeling, "Pathways to optical STED microscopy", *NanoBioImaging* **1**, 1 (2013).

[90] B. Harke, J. Keller, C. K. Ullal, V. Westphal, A. Schönle, and S. W. Hell, "Resolution scaling in STED microscopy", *Optics Express* **16**, 4154 (2008).

[91] F. Pampaloni and J. Enderlein, "Gaussian, Hermite-Gaussian, and Laguerre-Gaussian beams: a primer", *arXiv:physics/0410021* (2004).

[92] V. Westphal and S. W. Hell, "Nanoscale resolution in the focal plane of an optical microscope", *Physical Review Letters* **94**, 143903 (2005).

[93] E. Rittweger, K. Y. Han, S. E. Irvine, C. Eggeling, and S. W. Hell, "STED microscopy reveals crystal colour centres with nanometric resolution", *Nat Photon* **3**, 144 (2009).

[94] D. Wildanger, B. R. Patton, H. Schill, L. Marseglia, J. P. Hadden, S. Knauer, A. Schönle, J. G. Rarity, J. L. O'Brien, S. W. Hell, and J. M. Smith, "Solid immersion facilitates fluorescence microscopy with nanometer resolution and sub-Ångström emitter localization", *Advanced Materials* **24**, OP309 (2012).

[95] G. Donnert, J. Keller, R. Medda, M. A. Andrei, S. O. Rizzoli, R. Lührmann, R. Jahn, C. Eggeling, and S. W. Hell, "Macromolecular-scale resolution in biological fluorescence microscopy", *Proceedings of the National Academy of Sciences* **103**, 11440 (2006).

[96] K. Willig, B. Harke, R. Medda, and S. Hell, "STED microscopy with continuous wave beams", *NATURE METHODS* **4**, 915 (2007).

[97] J. R. Moffitt, C. Osseforth, and J. Michaelis, "Time-gating improves the spatial resolution of STED microscopy", *Optics Express* **19**, 4242 (2011).

[98] G. Vicidomini, G. Moneron, K. Han, V. Westphal, H. Ta, M. Reuss, J. Engelhardt, C. Eggeling, and S. Hell, "Sharper low-power sted nanoscopy by time gating", *nature methods* **8**, 571 (2011).

[99] G. Vicidomini, A. Schönle, H. Ta, K. Y. Han, G. Moneron, C. Eggeling, and S. W. Hell, "STED nanoscopy with time-gated detection: theoretical and experimental aspects", *PLoS ONE* **8**, e54421 (2013).

[100] D. Wildanger, J. Bückers, V. Westphal, S. W. Hell, and L. Kastrup, "STED microscope aligned by design", *Optics Express* **17**, 16100 (2009).

[101] G. Donnert, J. Keller, C. A. Wurm, S. O. Rizzoli, V. Westphal, A. Schonle, R. Jahn, S. Jakobs, C. Eggeling, and S. W. Hell, "Two-color far-field fluorescence nanoscopy", *Biophysical Journal* **92**, L67 (2007).

[102] L. Meyer, D. Wildanger, R. Medda, A. Punge, S. O. Rizzoli, G. Donnert, and S. W. Hell, "Dual-color STED microscopy at 30-nm focal-plane resolution", *Small* **4**, 1095 (2008).

[103] J. Tønnesen, F. Nadrigny, K. I. Willig, R. Wedlich-Söldner, and U. V. Nägerl, "Two-color STED microscopy of living synapses using a single laser-beam pair", *Biophysical Journal* **101**, 2545 (2011).

[104] R. Schmidt, C. A. Wurm, S. Jakobs, J. Engelhardt, A. Egner, and S. W. Hell, "Spherical nanosized focal spot unravels the interior of cells", *Nature Methods* **5**, 539 (2008).

[105] P. A. Pellett, X. Sun, T. J. Gould, J. E. Rothman, M.-Q. Xu, I. R. Corrêa, and J. Bewersdorf, "Two-color STED microscopy in living cells", *Biomedical Optics Express* **2**, 2364 (2011).

[106] J. B. Ding, K. T. Takasaki, and B. L. Sabatini, "Supraresolution imaging in brain slices using stimulated-emission depletion two-photon laser scanning microscopy", *Neuron* **63**, 429 (2009).

[107] G. Moneron and S. W. Hell, "Two-photon excitation STED microscopy", *Optics Express* **17**, 14567 (2009).

[108] P. Bethge, R. Chéreau, E. Avignone, G. Marsicano, and U. V. Nägerl, "Two-photon excitation STED microscopy in two colors in acute brain slices", *Biophysical Journal* **104**, 778 (2013).

[109] B. Harke, C. K. Ullal, J. Keller, and S. W. Hell, "Three-dimensional nanoscopy of colloidal crystals", *Nano Letters* **8**, 1309 (2008).

[110] S. W. Hell, R. Schmidt, and A. Egner, "Diffraction-unlimited three-dimensional optical nanoscopy with opposing lenses", *Nature Photonics* **3**, 381 (2009).

[111] D. WILDANGER, R. MEDDA, L. KASTRUP, and S. HELL, "A compact STED microscope providing 3D nanoscale resolution", *Journal of Microscopy* **236**, 35 (2009).

[112] M. Dyba and S. W. Hell, "Focal spots of size $\lambda/23$ open up far-field florescence microscopy at 33 nm axial resolution", *Physical Review Letters* **88**, 163901 (2002).

[113] M. Friedrich, Q. Gan, V. Ermolayev, and G. S. Harms, "STED-SPIM: stimulated emission depletion improves sheet illumination microscopy resolution", *Biophysical Journal* **100**, L43 (2011).

[114] M. Dyba, S. Jakobs, and S. W. Hell, "Immunofluorescence stimulated emission depletion microscopy", *Nature Biotechnology* **21**, 1303 (2003).

[115] V. Westphal, J. Seeger, T. Salditt, and S. W. Hell, "Stimulated emission depletion microscopy on lithographic nanostructures", *Journal of Physics B: Atomic, Molecular and Optical Physics* **38**, S695 (2005).

[116] R. Wollhofen, J. Katzmann, C. Hrelescu, J. Jacak, and T. A. Klar, "120 nm resolution and 55 nm structure size in STED-lithography", *Optics Express* **21**, 10831 (2013).

[117] D. Wildanger, J. R. Maze, and S. W. Hell, "Diffraction unlimited all-optical recording of electron spin resonances", *Physical Review Letters* **107**, 017601 (2011).

[118] L. Kastrup, H. Blom, C. Eggeling, and S. W. Hell, "Fluorescence fluctuation spectroscopy in subdiffraction focal volumes", *Physical Review Letters* **94**, 178104 (2005).

[119] H. Blom, L. Kastrup, and C. Eggeling, "Fluorescence fluctuation spectroscopy in reduced detection volumes", *Current Pharmaceutical Biotechnology* **7**, 51 (2006).

[120] E. Rittweger, D. Wildanger, and S. W. Hell, "Far-field fluorescence nanoscopy of diamond color centers by ground state depletion", *EPL (Europhysics Letters)* **86**, 14001 (2009).

[121] K. Y. Han, S. K. Kim, C. Eggeling, and S. W. Hell, "Metastable dark states enable ground state depletion microscopy of nitrogen vacancy centers in diamond with diffraction-unlimited resolution", *Nano Lett.* **10**, 3199 (2010).

[122] M. Hofmann, C. Eggeling, S. Jakobs, and S. W. Hell, "Breaking the diffraction barrier in fluorescence microscopy at low light intensities by using re-

versibly photoswitchable proteins", *Proceedings of the National Academy of Sciences of the United States of America* **102**, 17565 (2005).

[123] M. A. Schwentker, H. Bock, M. Hofmann, S. Jakobs, J. Bewersdorf, C. Eggeling, and S. W. Hell, "Wide-field subdiffraction RESOLFT microscopy using fluorescent protein photoswitching", *Microscopy Research and Technique* **70**, 269 (2007).

[124] L. Schermelleh, P. M. Carlton, S. Haase, L. Shao, L. Winoto, P. Kner, B. Burke, M. C. Cardoso, D. A. Agard, M. G. L. Gustafsson, H. Leonhardt, and J. W. Sedat, "Subdiffraction multicolor imaging of the nuclear periphery with 3D structured illumination microscopy", *Science* **320**, 1332 (2008).

[125] P. Kner, B. B. Chhun, E. R. Griffis, L. Winoto, and M. G. L. Gustafsson, "Super-resolution video microscopy of live cells by structured illumination", *Nature Methods* **6**, 339 (2009).

[126] E. Mudry, K. Belkebir, J. Girard, J. Savatier, E. L. Moal, C. Nicoletti, M. Allain, and A. Sentenac, "Structured illumination microscopy using unknown speckle patterns", *Nature Photonics* **6**, 312 (2012).

[127] F. Wei and Z. Liu, "Plasmonic structured illumination microscopy", *Nano Letters* **10**, 2531 (2010).

[128] E. H. Rego, L. Shao, J. J. Macklin, L. Winoto, G. A. Johansson, N. Kamps-Hughes, M. W. Davidson, and M. G. L. Gustafsson, "Nonlinear structured-illumination microscopy with a photoswitchable protein reveals cellular structures at 50-nm resolution", *Proceedings of the National Academy of Sciences* **109**, E135 (2012).

[129] A. Yildiz, J. N. Forkey, S. A. McKinney, T. Ha, Y. E. Goldman, and P. R. Selvin, "Myosin V walks hand-over-hand: single fluorophore imaging with 1.5-nm localization", *Science* **300**, 2061 (2003).

[130] X. Qu, D. Wu, L. Mets, and N. F. Scherer, "Nanometer-localized multiple single-molecule fluorescence microscopy", *Proceedings of the National Academy of Sciences of the United States of America* **101**, 11298 (2004).

[131] S. Manley, J. M. Gillette, G. H. Patterson, H. Shroff, H. F. Hess, E. Betzig, and J. Lippincott-Schwartz, "High-density mapping of single-molecule trajectories with photoactivated localization microscopy", *Nature Methods* **5**, 155 (2008).

[132] O. Rossier, V. Octeau, J.-B. Sibarita, C. Leduc, B. Tessier, D. Nair, V. Gatterdam, O. Destaing, C. Albigès-Rizo, R. Tampé, L. Cognet, D. Choquet, B. Lounis, and G. Giannone, "Integrins β1 and β3 exhibit distinct dynamic nanoscale organizations inside focal adhesions", *Nature Cell Biology* **14**, 1057 (2012).

[133] M. V. Gudheti, N. M. Curthoys, T. J. Gould, D. Kim, M. S. Gunewardene, K. A. Gabor, J. A. Gosse, C. H. Kim, J. Zimmerberg, and S. T. Hess, "Actin mediates the nanoscale membrane organization of the clustered membrane protein influenza hemagglutinin", *Biophysical Journal* **104**, 2182 (2013).

[134] G. Fu, T. Huang, J. Buss, C. Coltharp, Z. Hensel, and J. Xiao, "In vivo structure of the E. coli FtsZ-ring revealed by photoactivated localization microscopy (PALM)", *PLoS ONE* **5**, e12680 (2010).

[135] B. Huang, W. Wang, M. Bates, and X. Zhuang, "Three-dimensional super-resolution imaging by stochastic optical reconstruction microscopy", *Science* **319**, 810 (2008).

[136] A. Dani, B. Huang, J. Bergan, C. Dulac, and X. Zhuang, "Superresolution imaging of chemical synapses in the brain", *Neuron* **68**, 843 (2010).

[137] A. Löschberger, S. v. d. Linde, M.-C. Dabauvalle, B. Rieger, M. Heilemann, G. Krohne, and M. Sauer, "Super-resolution imaging visualizes the eightfold symmetry of gp210 proteins around the nuclear pore complex and resolves the central channel with nanometer resolution", *Journal of Cell Science* **125**, 570 (2012).

[138] J. Fölling, M. Bossi, H. Bock, R. Medda, C. A. Wurm, B. Hein, S. Jakobs, C. Eggeling, and S. W. Hell, "Fluorescence nanoscopy by ground-state depletion and single-molecule return", *Nature Methods* **5**, 943 (2008).

[139] B. Lalkens, I. Testa, K. I. Willig, and S. W. Hell, "MRT letter: Nanoscopy of protein colocalization in living cells by STED and GSDIM", *Microscopy Research and Technique* **75**, 1 (2012).

[140] G. Lukinavičius, K. Umezawa, N. Olivier, A. Honigmann, G. Yang, T. Plass, V. Mueller, L. Reymond, I. R. Corrêa Jr, Z.-G. Luo, C. Schultz, E. A. Lemke, P. Heppenstall, C. Eggeling, S. Manley, and K. Johnsson, "A near-infrared fluorophore for live-cell super-resolution microscopy of cellular proteins", *Nature Chemistry* **5**, 132 (2013).

[141] P. Winckler, L. Lartigue, G. Giannone, F. De Giorgi, F. Ichas, J.-B. Sibarita, B. Lounis, and L. Cognet, "Identification and super-resolution imaging of ligand-activated receptor dimers in live cells", *Scientific Reports* **3**, (2013).

[142] M. F. Juette, T. J. Gould, M. D. Lessard, M. J. Mlodzianoski, B. S. Nagpure, B. T. Bennett, S. T. Hess, and J. Bewersdorf, "Three-

dimensional sub–100 nm resolution fluorescence microscopy of thick samples", *Nature Methods* **5**, 527 (2008).

[143] S. R. P. Pavani, M. A. Thompson, J. S. Biteen, S. J. Lord, N. Liu, R. J. Twieg, R. Piestun, and W. E. Moerner, "Three-dimensional, single-molecule fluorescence imaging beyond the diffraction limit by using a double-helix point spread function", *Proceedings of the National Academy of Sciences* **106**, 2995 (2009).

[144] M. Bates, B. Huang, G. T. Dempsey, and X. Zhuang, "Multicolor super-resolution imaging with photo-switchable fluorescent probes", *Science* **317**, 1749 (2007).

[145] B. Huang, S. A. Jones, B. Brandenburg, and X. Zhuang, "Whole-cell 3D STORM reveals interactions between cellular structures with nanometer-scale resolution", *Nature Methods* **5**, 1047 (2008).

[146] M. Andresen, A. C. Stiel, J. Fölling, D. Wenzel, A. Schönle, A. Egner, C. Eggeling, S. W. Hell, and S. Jakobs, "Photoswitchable fluorescent proteins enable monochromatic multilabel imaging and dual color fluorescence nanoscopy", *Nature Biotechnology* **26**, 1035 (2008).

[147] M. Bossi, J. Fölling, V. N. Belov, V. P. Boyarskiy, R. Medda, A. Egner, C. Eggeling, A. Schönle, and S. W. Hell, "Multicolor far-field fluorescence nanoscopy through isolated detection of distinct molecular species", *Nano Letters* **8**, 2463 (2008).

[148] F. V. Subach, G. H. Patterson, S. Manley, J. M. Gillette, J. Lippincott-Schwartz, and V. V. Verkhusha, "Photoactivatable mCherry for high-resolution two-color fluorescence microscopy", *Nature Methods* **6**, 153 (2009).

[149] M. P. Backlund, M. D. Lew, A. S. Backer, S. J. Sahl, and W. E. Moerner, "The role of molecular dipole orientation in single-molecule fluorescence microscopy and implications for super-resolution imaging", *ChemPhysChem* **15**, 587 (2014).

[150] J. Engelhardt, J. Keller, P. Hoyer, M. Reuss, T. Staudt, and S. W. Hell, "Molecular orientation affects localization accuracy in superresolution far-field fluorescence microscopy", *Nano Lett.* **11**, 209 (2010).

[151] A. S. Backer, M. P. Backlund, M. D. Lew, and W. E. Moerner, "Single-molecule orientation measurements with a quadrated pupil", *Optics Letters* **38**, 1521 (2013).

[152] A. S. Backer, M. P. Backlund, A. R. v. Diezmann, S. J. Sahl, and W. E. Moerner, "A bisected pupil for studying single-molecule orientational dynamics and its application to three-dimensional super-resolution microscopy", *Applied Physics Letters* **104**, 193701 (2014).

[153] K. Fujita, M. Kobayashi, S. Kawano, M. Yamanaka, and S. Kawata, "High-resolution confocal microscopy by saturated excitation of fluorescence", *Physical Review Letters* **99**, 228105 (2007).

[154] Y. Yonemaru, M. Yamanaka, N. I. Smith, S. Kawata, and K. Fujita, "Saturated excitation microscopy with optimized excitation modulation", *ChemPhysChem* **15**, 743 (2014).

[155] S.-W. Chu, H.-Y. Wu, Y.-T. Huang, T.-Y. Su, H. Lee, Y. Yonemaru, M. Yamanaka, R. Oketani, S. Kawata, S. Shoji, and K. Fujita, "Saturation and reverse saturation of scattering in a single plasmonic nanoparticle", *ACS Photonics* **1**, 32 (2014).

[156] S.-W. Chu, T.-Y. Su, R. Oketani, Y.-T. Huang, H.-Y. Wu, Y. Yonemaru, M. Yamanaka, H. Lee, G.-Y. Zhuo, M.-Y. Lee, S. Kawata, and K. Fujita, "Measurement of a saturated emission of optical radiation from gold nanoparticles: application to an ultrahigh resolution microscope", *Physical Review Letters* **112**, 017402 (2014).

[157] T. Dertinger, R. Colyer, G. Iyer, S. Weiss, and J. Enderlein, "Fast, background-free, 3D super-resolution optical fluctuation imaging (SOFI)", *Proceedings of the National Academy of Sciences* **106**, 22287 (2009).

[158] T. Dertinger, M. Heilemann, R. Vogel, M. Sauer, and S. Weiss, "Superresolution optical fluctuation imaging with organic dyes", *Angewandte Chemie* **122**, 9631 (2010).

[159] S. Geissbuehler, C. Dellagiacoma, and T. Lasser, "Comparison between SOFI and STORM", *Biomedical Optics Express* **2**, 408 (2011).

[160] N. Hafi, M. Grunwald, L. S. van den Heuvel, T. Aspelmeier, J.-H. Chen, M. Zagrebelsky, O. M. Schütte, C. Steinem, M. Korte, A. Munk, and P. J. Walla, "Fluorescence nanoscopy by polarization modulation and polarization angle narrowing", *Nature Methods* **11**, 579 (2014).

[161] S. W. Hell, "Microscopy and its focal switch", *Nature Methods* **6**, 24 (2009).

[162] C. Shannon, "Communication in the presence of noise", *Proceedings of the IRE* **37**, 10 (1949).

[163] S. J. Holden, S. Uphoff, and A. N. Kapanidis, "DAOSTORM: an algorithm for high-density super-resolution microscopy", *Nature Methods* **8**, 279 (2011).

[164] F. Huang, S. L. Schwartz, J. M. Byars, and K. A. Lidke, "Simultaneous multiple-emitter fitting for single molecule super-resolution imaging", *Biomedical Optics Express* **2**, 1377 (2011).

[165] P. Bingen, M. Reuss, J. Engelhardt, and S. W. Hell, "Parallelized STED fluorescence nanoscopy", *Optics Express* **19**, 23716 (2011).

[166] G. Grynberg, B. Lounis, P. Verkerk, J.-Y. Courtois, and C. Salomon, "Quantized motion of cold cesium atoms in two- and three-dimensional optical potentials", *Physical Review Letters* **70**, 2249 (1993).

[167] A. Hemmerich and T. W. Hänsch, "Two-dimensional atomic crystal bound by light", *Physical Review Letters* **70**, 410 (1993).

[168] M. Campbell, D. N. Sharp, M. T. Harrison, R. G. Denning, and A. J. Turberfield, "Fabrication of photonic crystals for the visible spectrum by holographic lithography", *Nature* **404**, 53 (2000).

[169] M. P. MacDonald, G. C. Spalding, and K. Dholakia, "Microfluidic sorting in an optical lattice", *Nature* **426**, 421 (2003).

[170] L. Novotny, R. D. Grober, and K. Karrai, "reflected image of a strongly focused spot", *Optics Letters* **26**, 789 (2001).

[171] K. Lindfors, T. Kalkbrenner, P. Stoller, and V. Sandoghdar, "Detection and spectroscopy of gold nanoparticles using supercontinuum white light confocal microscopy", *Physical Review Letters* **93**, 037401 (2004).

[172] M. Dyba and S. Hell, "Photostability of a fluorescent marker under pulsed excited-state depletion through stimulated emission", *APPLIED OPTICS* **42**, (2003).

[173] C. Eggeling, A. Volkmer, and C. A. M. Seidel, "Molecular photobleaching kinetics of Rhodamine 6G by one- and two-photon induced confocal fluorescence microscopy", *ChemPhysChem* **6**, 791 (2005).

[174] L. P. Chew, "Constrained delaunay triangulations", *Algorithmica* **4**, 97 (1989).

[175] G. Moneron, R. Medda, B. Hein, A. Giske, V. Westphal, and S. W. Hell, "Fast STED microscopy with continuous wave fiber lasers", *Optics Express* **18**, 1302 (2010).

[176] G. Donnert, C. Eggeling, and S. Hell, "Major signal increase in fluorescence microscopy through dark-state relaxation", *NATURE METHODS* **4**, 81 (2007).

[177] J. Vogelsang, R. Kasper, C. Steinhauer, B. Person, M. Heilemann, M. Sauer, and P. Tinnefeld, "A reducing and oxidizing system minimizes photobleaching and blinking of fluorescent dyes", *Angewandte Chemie International Edition* **47**, 5465 (2008).

[178] J. O. Carnali and M. S. Naser, "The use of dilute solution viscometry to characterize the network properties of carbopol microgels", *Colloid and Polymer Science* **270**, 183 (1992).

[179] P. Tamarat, A. Maali, B. Lounis, and M. Orrit, "Ten years of single-molecule spectroscopy", *J. Phys. Chem. A* **104**, 1 (1999).

[180] R. Kaufmann, C. Hagen, and K. Grünewald, "Fluorescence cryo-microscopy: current challenges and prospects", *Current Opinion in Chemical Biology* **20**, 86 (2014).

[181] C. Bleck, A. Merz, M. Gutierrez, P. Walther, J. Dubochet, B. Zuber, and G. Griffiths, "Comparison of different methods for thin section EM analysis of Mycobacterium smegmatis", *Journal of Microscopy* **237**, 23 (2010).

[182] G. Schneider, P. Guttmann, S. Rehbein, S. Werner, and R. Follath, "Cryo X-ray microscope with flat sample geometry for correlative fluorescence and nanoscale tomographic imaging", *Journal of Structural Biology* **177**, 212 (2012).

[183] I. Hurbain and M. Sachse, "The future is cold: cryo-preparation methods for transmission electron microscopy of cells", *Biology of the Cell* **103**, 405 (2011).

[184] J.-B. Trebbia, H. Ruf, P. Tamarat, and B. Lounis, "Efficient generation of near infra-red single photons from the zero-phonon line of a single molecule", *Optics Express* **17**, 23986 (2009).

[185] J.-B. Trebbia, P. Tamarat, and B. Lounis, "Indistinguishable near-infrared single photons from an individual organic molecule", *Physical Review A* **82**, 063803 (2010).

[186] Y.-W. Chang, S. Chen, E. I. Tocheva, A. Treuner-Lange, S. Löbach, L. Søgaard-Andersen, and G. J. Jensen, "Correlated cryogenic photoactivated localization microscopy and cryo-electron tomography", *Nature Methods* **11**, 737 (2014).

[187] R. Kaufmann, P. Schellenberger, E. Seiradake, I. M. Dobbie, E. Y. Jones, I. Davis, C. Hagen, and K. Grünewald, "Super-resolution microscopy using standard fluorescent proteins in intact cells under cryo-conditions", *Nano Letters* **14**, 4171 (2014).

[188] S. Weisenburger, B. Jing, D. Hänni, L. Reymond, B. Schuler, A. Renn, and V. Sandoghdar, "Cryogenic colocalization microscopy for nanometer-distance measurements", *ChemPhysChem* **15**, 763 (2014).

[189] B. Lounis and M. Orrit, "Single-photon sources", *Reports on Progress in Physics* **68**, 1129 (2005).

[190] B. Lounis and W. Moerner, "Single photons on demand from a single molecule at room temperature", *Nature* **407**, 491 (2000).

[191] B. Lounis, H. A. Bechtel, D. Gerion, P. Alivisatos, and W. E. Moerner, "Photon antibunching in single CdSe/ZnS quantum dot fluorescence", *Chemical Physics Letters* **329**, 399 (2000).

[192] T. Gaebel, M. Domhan, I. Popa, C. Wittmann, P. Neumann, F. Jelezko, J. R. Rabeau, N. Stavrias, A. D. Greentree, S. Prawer, J. Meijer, J. Twamley, P. R. Hemmer, and J. Wrachtrup, "Room-temperature coherent coupling of single spins in diamond", *Nature Physics* **2**, 408 (2006).

[193] C. Hettich, C. Schmitt, J. Zitzmann, S. Kühn, I. Gerhardt, and V. Sandoghdar, "Nanometer resolution and coherent optical dipole coupling of two individual molecules", *Science* **298**, 385 (2002).

[194] M. Celebrano, R. Lettow, P. Kukura, M. Agio, A. Renn, S. Götzinger, and V. Sandoghdar, "Efficient coupling of single photons to single plasmons", *Optics Express* **18**, 13829 (2010).

[195] D. E. Chang, A. S. Sørensen, E. A. Demler, and M. D. Lukin, "A single-photon transistor using nanoscale surface plasmons", *Nature Physics* **3**, 807 (2007).

[196] G. V. Varada and G. S. Agarwal, "Two-photon resonance induced by the dipole-dipole interaction", *Physical Review A* **45**, 6721 (1992).

[197] W. Moerner and L. Kador, "Optical detection and spectroscopy of single molecules in a solid", *Physical Review Letters* **62**, 2535 (1989).

[198] W. E. Moerner and M. Orrit, "Illuminating Single Molecules in Condensed Matter", *Science* **283**, 1670 (1999).

[199] J. Wiedmann and A. Penzkofer, "Excited-state absorption cross-sections in rhodamine dyes determined after molecular reorientation", *Il Nuovo Cimento B Series 11* **63**, 459 (1981).

[200] E. Rittweger, B. Rankin, V. Westphal, and S. Hell, "Fluorescence depletion mechanisms in super-resolving STED microscopy", *Chemical Physics Letters* **442**, 483 (2007).

[201] W. E. Moerner, *Single-Molecule Optical Detection, Imaging and Spectroscopy* (VCH Verlagsgesellschaft mbH, 1996), pp. 1–30.

[202] T. Plakhotnik, W. E. Moerner, V. Palm, and U. P. Wild, "Single molecule spectroscopy: maximum emission rate and saturation intensity", *Optics Communications* **114**, 83 (1995).

[203] M. Born and E. Wolf, *Principles of optics: electromagnetic theory of propagation, interference and diffraction of light* (CUP Archive, 1999).

[204] A. Fuensanta and D. Nathan, *Topics in Adaptive Optics* (InTech, 2012).

[205] P. A. Santi, "Light sheet fluorescence microscopy a review", *Journal of Histochemistry & Cytochemistry* **59**, 129 (2011).

[206] P. J. Keller and H.-U. Dodt, "Light sheet microscopy of living or cleared specimens", *Current Opinion in Neurobiology* **22**, 138 (2012).

[207] D. Wildanger, E. Rittweger, L. Kastrup, and S. W. Hell, "STED microscopy with a supercontinuum laser source", *Optics Express* **16**, 9614 (2008).

[208] Y. Sivan, Y. Sonnefraud, S. Kena-Cohen, J. B. Pendry, and S. A. Maier, "Nanoparticle-assisted stimulated-emission-depletion nanoscopy", *ACS Nano* (2012).

[209] A. Chmyrov, J. Keller, T. Grotjohann, M. Ratz, E. d'Este, S. Jakobs, C. Eggeling, and S. W. Hell, "Nanoscopy with more than 100,000 'doughnuts"', *Nature Methods* **10**, 737 (2013).

APPENDIX A

Three-beam interference optical lattice

A.1 Rotations of the polarisation and of the wave vector

In this section, we will discuss the rotations of the polarization and of the wave vector of a laser beam which enters the objective and gets deviated. The incident wave with the wave vector $\vec{k_i}$ propagates parallel to the optical axis of the objective $\vec{e_z}$. It has linear polarization $\vec{e_i}$, parallel to the x-axis $\vec{e_x}$ (see Figure A.1).

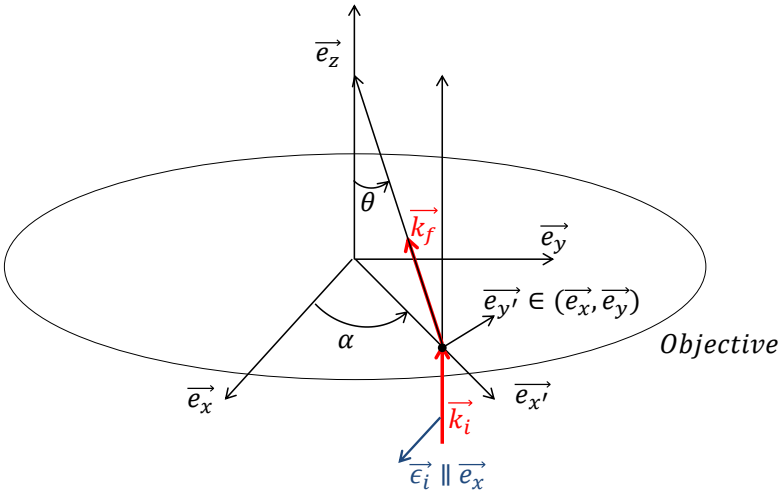

Figure A.1: Geometrical configuration of the incident wave $\vec{k_i}$ and the transmitted wave $\vec{k_f}$. Red lines show the wave vectors and the blue arrow indicates the polarization.

We set two Cartesian bases as $B_1 = (\vec{e_x}, \vec{e_y}, \vec{e_z})$ and $B_2 = (\vec{e_{x'}}, \vec{e_{y'}}, \vec{e_z})$. The matrix for changing the basis from B_1 to B_2 is:

$$M_{1\to 2} = \begin{pmatrix} cos\alpha & sin\alpha & 0 \\ -sin\alpha & cos\alpha & 0 \\ 0 & 0 & 1 \end{pmatrix} \tag{A.1}$$

The polarization of the incident beam is $(1, 0, 0)$ in the basis B_1. In the basis B_2, it will be:

$$(\vec{e_i})_{B_2} = M_{1\to 2}\,(\vec{e_i})_{B_1} = \begin{pmatrix} cos\alpha & sin\alpha & 0 \\ -sin\alpha & cos\alpha & 0 \\ 0 & 0 & 1 \end{pmatrix} \begin{pmatrix} 1 \\ 0 \\ 0 \end{pmatrix} = \begin{pmatrix} cos\alpha \\ -sin\alpha \\ 0 \end{pmatrix} \tag{A.2}$$

The transmitted wave's polarization $\vec{e_f}$ is the rotation of the incident wave's polarization of an angle θ around the axis $\vec{e_{y'}}$. The rotation matrix is:

$$N = \begin{pmatrix} cos\theta & 0 & -sin\theta \\ 0 & 1 & 0 \\ sin\theta & 0 & cos\theta \end{pmatrix} \tag{A.3}$$

Therefore the transmitted wave's polarization in the basis B_2 is given by:

$$(\vec{e_f})_{B_2} = N\,(\vec{e_i})_{B_2} \tag{A.4}$$

We can then rewrite the transmitted wave's polarization in the basis B_1 as:

$$(\vec{e_f})_{B_1} = M_{1\to 2}^{-1}\,N\,M_{1\to 2}\,(\vec{e_i})_{B_1} = \begin{pmatrix} cos^2\alpha\, cos\theta + sin^2\alpha \\ cos\alpha\, sin\alpha\,(cos\theta - 1) \\ cos\alpha\, sin\theta \end{pmatrix} \tag{A.5}$$

We now consider the wave vector. The incident wave vector can be written as $\vec{k_i} = (0\ 0\ k)$, which only has the component along the z-axis $\vec{e_z}$. Therefore we have

$$(\vec{k_i})_{B_2} = (\vec{k_i})_{B_1} \tag{A.6}$$

The transmitted wave vector follows a rotation along the axis $\vec{e_{y'}}$ and can be expressed in the basis B_1 as:

$$(\vec{k_f})_{B_1} = M_{1\to 2}^{-1}\ N\ \vec{k_i} = \begin{pmatrix} -cos\alpha\ sin\theta \\ -sin\alpha\ sin\theta \\ cos\theta \end{pmatrix} k \tag{A.7}$$

A.2 Period of the three-beam interference pattern

In this section, we discuss the period of the three-beam interference pattern at $\alpha = 30°$. Following Equation 2.9 and Equation 2.10, the periodicity of the optical lattices is linked to phase terms $\Phi_{p,q}$., which writes as:

$$\begin{aligned} \Phi_{p,q} &= \left(\vec{k_p'} - \vec{k_q'}\right) \cdot \vec{r} \\ &= \left(\vec{k_p'} - \vec{k_q'}\right) \cdot (r\,cos\varphi\,\vec{e}_x + r\,sin\varphi\,\vec{e}_y) \\ &= \frac{2n\pi r}{\lambda} sin\theta\,[(cos\alpha_q - cos\alpha_p)cos\varphi + (sin\alpha_q - sin\alpha_p)sin\varphi] \end{aligned} \tag{A.8}$$

r and φ are the polar coordinates at the interference plane, see Fig. A.2. $\alpha = 30°$, therefore we have $\alpha_1 = 30°$, $\alpha_2 = 150°$, $\alpha_3 = 270°$. The phase terms can be thus expressed as:

$$\begin{cases} \Phi_{1,2} = -\frac{2n\pi r}{\lambda}\ sin\theta\ \sqrt{3}cos\varphi \\ \Phi_{2,3} = \frac{2n\pi r}{\lambda}\ sin\theta\ \left(\frac{\sqrt{3}}{2}cos\varphi - \frac{3}{2}sin\varphi\right) \\ \Phi_{3,1} = \frac{2n\pi r}{\lambda}\ sin\theta\ \left(\frac{\sqrt{3}}{2}cos\varphi + \frac{3}{2}sin\varphi\right) \end{cases} \tag{A.9}$$

Note that $\Phi_{1,2}+\Phi_{2,3}+\Phi_{3,1}=0$, we can treat simple cases by setting one of the phase

terms equal to 0. For example, by setting $\Phi_{1,2}$=0 ($\varphi = 90°$), we have $\Phi_{2,3}$=-$\Phi_{3,1}$. The interference pattern has the expression:

$$I(r) = A + B\ cos(\frac{3\pi nr}{\lambda} sin\theta) \tag{A.10}$$

A and B are constants. The period along $\varphi = 90°$ is then:

$$p = \frac{2\lambda}{3n\ sin\theta} \tag{A.11}$$

Setting $\Phi_{2,3}$=0 and $\Phi_{3,1}$=0 leads us to the same expression of the period along $\varphi = 30°$ and 150°, confirmed by the simulated intensity distribution of the optical lattice shown in Fig. A.2. Equation A.11 gives therefore the period of the optical lattices generated with the three-beam interference for α=30°.

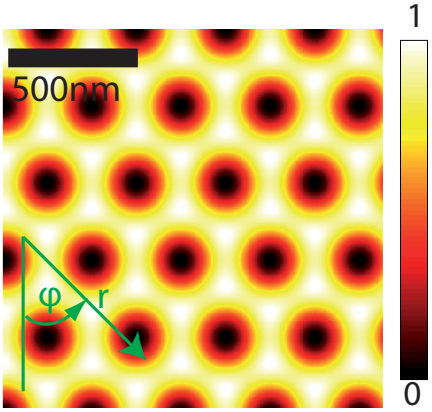

Figure A.2: Intensity distribution of the three-beam interference pattern for $\alpha = 30°$ and $\theta = 70°$. Lower left corner shows the polar coordinates.

APPENDIX B

Cross-talk between neighbour "detectors" in Lattice-STED

In Lattice-STED, the binary mask and the camera acts together as an array of "point detectors", with each "point detector" corresponding to one of the intensity minimum of the optical lattice. While a fluophore is at one intensity minima, it can emit fluorescence, which will be detected by the corresponding "point detector", named "detector" 1. Due to the short distance between the "detectors" (290 nm) compared to the emission PSF, "detectors" neighbouring to "detector" 1 can also detect a small amount of fluorescence emitted by the fluorophore (see Figure B.1). This causes cross-talk between "detectors" and leads to artefacts in the super-resolution images. The artefact is called "ghost", meaning that a fluophore has a brighter image at the right coordinates and darker images appearing in adjacent sub-images. Therefore a linear unmixing is applied to the "detectors" to eliminate the cross-talk, as explained below.

We define the cross-talk as the ratio between the fluorescence signals detected by "detector" 1 and 2. a and b are respectively the cross-talks between horizontal (or vertical) and diagonal neighbour "detectors", which are given by:

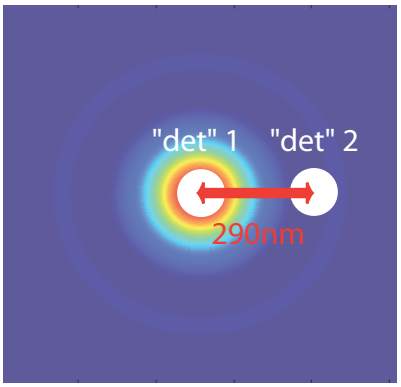

Figure B.1: "Cross-talk" between two "detectors", separated with a distance of 290 nm (period of the optical lattice). The background shows the emission PSF of a fluorophore centred at "detector" 1.

$$
\begin{aligned}
a &= \frac{\int_{-R}^{R}\int_{p-\sqrt{R^2-y^2}}^{p+\sqrt{R^2-y^2}} PSF(x,y)dxdy}{\int_{-R}^{R}\int_{\sqrt{R^2-y^2}}^{\sqrt{R^2-y^2}} PSF(x,y)dxdy} \\
b &= \frac{\int_{p-R}^{p+R}\int_{p-\sqrt{R^2-(y-p)^2}}^{p+\sqrt{R^2-(y-p)^2}} PSF(x,y)dxdy}{\int_{-R}^{R}\int_{\sqrt{R^2-y^2}}^{\sqrt{R^2-y^2}} PSF(x,y)dxdy}
\end{aligned}
\tag{B.1}
$$

where p is the period of the optical lattice and R is the radius of the "detectors". $PSF(x,y)$ is the emission PSF of a fluorophore and is given by:

$$
PSF = \left[\frac{2J_1(k\,NA\,r)}{k\,NA\,r}\right]^2 \tag{B.2}
$$

where J_1 is the Bessel function of the first kind of order one, $k = 2\pi/\lambda$ is the wavenumber, NA is the numerical aperture and r is the radial distance from the optical axis.

Suppose that there is an array of P * Q "detectors", and cross-talk only exists between

neighbour "detectors", the fluorescence signal $F_{p,q}$ of the detector (p,q) would be:

$$\begin{aligned} F_{p,q} = F'_{p,q} &+ a(F'_{p-1,q} + F'_{p+1,q} + F'_{p,q-1} + F'_{p,q+1}) \\ &+ b(F'_{p-1,q-1} + F'_{p-1,q+1} + F'_{p+1,q-1} + F'_{p+1,q+1}) \end{aligned} \tag{B.3}$$

with $1 < p < P$ and $1 < q < Q$. $F_{p,q}$ consists of the fluorescence originating from emitters in the region of the detector (p,q) ($F'_{p,q}$) and cross-talks of fluorescences from emitters in its neighbour "detectors". A similar formula can be written for p=1,P or q=1,Q.

Set $F_l = F_{p,q}$ with $l = (p-1) * P + q$, Equations B.3 writes:

$$\begin{aligned} F_l = F'_l &+ a(F'_{l-P} + F'_{l+P} + F'_{l+1} + F'_{l-1}) \\ &+ b(F'_{l-P-1} + F'_{l-P+1} + F'_{l+P-1} + F'_{l+P+1}) \end{aligned} \tag{B.4}$$

with $l = 1, 2, ..., P * Q$. Equations.B.4 consist of $P * Q$ equations and can be written as:

$$M * F' = F \tag{B.5}$$

M is the cross-talk matrix depending on a and b, F' and F are respectively the fluorescence values of "detectors" without and with the cross-talk.

The fluorescence values of "detectors" corrected from cross-talk are therefore:

$$F' = M^{-1}F \tag{B.6}$$

Abstract: This thesis presents the development of two new super-resolution microscopy techniques.

The first technique aims at improving the imaging speed of super-resolution microscopy at room temperature for biological applications. As a scanning technique, STED (Stimulated Emission Depletion) microscopy needs parallelization for fast wide-field imaging. Using well-designed optical lattices for depletion together with wide-field excitation and a fast camera for detection, we achieve large parallelization of STED microscopy. Wide field of view super-resolved images are acquired by scanning over a single unit cell of the optical lattice, which can be as small as 290 nm * 290 nm. Lattice-STED imaging is demonstrated with a resolution down to 70 nm at 12.5 frames per second.

The second one extends super-resolution microscopy to liquid helium temperature for applications in quantum technologies. Optical resolution of solid-state single quantum emitters at the nanometer scale is a challenging step towards the control of delocalized states formed by strongly and coherently interacting emitters. ESSat (Excited State Saturation) microscopy operating at cryogenic temperatures is based on optical saturation of the excited state of single fluorescent molecules with a doughnut-shaped beam. Sub-10 nm resolution is achieved with extremely low excitation intensities, more than million times lower than those used in room temperature STED microscopy. Compared to super-localisation approaches, our technique offers a unique opportunity to super-resolve single molecules having overlapping optical resonance frequencies, paving the way to the study of coherent interactions between single emitters and to the manipulation of their degree of entanglement.

Keywords: super-resolution, microscopy, STED, single molecule

Résumé: Cette thèse présente le développement de deux méthodes de microscopie super-résolue.

La première méthode vise à améliorer la vitesse d'imagerie de la microscopie super-résolue à température ambiante pour des applications biologiques. En tant qu'une technique de scan, la microscopie STED a besoins d'être parallélisé pour faire de l'imagerie rapide en champ large. Nous avons obtenu une parallélisation massive de la microscopie STED en utilisant les réseaux d'optique avec une excitation en en champ large et une caméra rapide pour détection. Les images super-résolues d'un champ de 3 µm par 3 µm sont acquises en scannant une maille élémentaire du réseau optique, qui peut être aussi petite que 290 nm * 290 nm. La microscopie Lattice-STED est démontrée avec une résolution allant jusqu'à 70 nm à une cadence de 12,5 images par seconde.

La deuxième méthode étend la microscopie super-résolue à la température de l'hélium liquide pour des applications aux technologies quantiques. Des résolutions optiques à l'échelle nanométrique des émetteurs quantique est une étape cruciale vers le contrôle des états délocalisés formés par les interactions fortes et cohérentes entre des émetteurs. Dans ce contexte, nous avons développé une technique de microscopie à des températures cryogéniques, dénommée la microscopie Essat. Cette technique est basée sur la saturation optique de l'état excité des molécules fluorescentes uniques par l'excitation d'un faisceau en forme d'anneau. Une résolution moins de 10 nm est obtenue avec de basses intensités d'excitation, plus de millions de fois plus faibles que celles utilisées dans la microscopie STED à la température ambiante. Par rapport aux approches basées sur la super-localisation, notre technique offre une occasion unique de résoudre sous la limite de diffraction les molécules uniques ayant des fréquences de résonance optiques qui se chevauchent. Ceci ouvre la voie à l'étude des interactions cohérentes entre émetteurs uniques et à la manipulation de leur degré d'intrication.

Mot-clés: super-résolution, microscopie, STED, molécule unique